Plasmon Enhanced Titanium Dioxide Nanotubes for Nanophotonics, Non-linear Optics, and Photocatalysis

by

Sheng Zeng

A thesis submitted in partial fulfillment of the requirement for the degree of

Doctor of Philosophy

in

Solid State Electronics

Department of Electrical Computer Engineering

University of Alberta

Abstract:

Photocatalysis was originally inspired by photosynthetic models from nature, and now opens the window to a wider range of applications including but not limited to solar-to-chemical energy storage, water/air purification. Both photocatalytic hydrogen generation and CO_2 to hydrocarbon processes are aiming to kill two birds with one stone by treating wastes and producing clean energy. Hydrogen has been considered as an ultimate clean energy source and is heavily relied upon for fuel cells. With that being said, so far, hydrogen has been still mainly produced from fossil fuels by steam reforming instead of photocatalytic water splitting which is a greener method. CO_2 photoreduction is able to store solar energy and reduce CO_2 concentration in the atmosphere simultaneously. Nature creates a balance of carbon resources in ecosystems, however anthropogenic interference destroys that balance. Photocatalytic CO_2 capture is an ideal approach to close the anthropogenically opened carbon loop. This way, it rebalances the carbon emissions as in the case of photosynthesis in green plants. Largely, all my motivation comes from the urgency with global problems such as global warming and environmental pollution, which accelerate the need for greater research into photocatalysis. Thus, my efforts have been put into how to design and fabricate highly efficient photocatalysts and enhance the performance of challenging photocatalytic reactions.

I started my first PhD project with a review paper on photocatalytic CO_2 reduction using perovskite oxide nanomaterials. As the material focus of this review article, I selected perovskite oxides because they are mostly earth-abundant, nontoxic to nature, chemically stable, and tunable in many aspects such as crystal structures, bandgaps and surface energies. This review paper offers me key

insights for developing advanced photocatalysts in order to improve the yields of CO_2 reduction products.

Having accomplished this review paper, I found that nanophotonics and plasmons are good angles to tackle the problem of photocatalyst with less efficiency. The idea and efforts turned into the next scientific article, entitled "optical control of selectivity of high rate CO_2 photoreduction via interband-or hot electron Z-scheme reaction pathways in Au-TiO_2 plasmonic photonic crystal photocatalyst". The periodically modulated TiO_2 nanotube arrays were decorated with gold nanoparticles to form plasmonic photonic crystal photocatalysts from which dramatically improved performance and remarkable selectivity are obtained.

Admittedly, plasmonic photocatalysis promises using light as the energy source to drive a variety of thermal energy-intensive chemical reactions, however, the incorporation of plasmonic noble metals has become a double-edged sword. To overcome the drawback of relying on noble metals became the motivation of the next two manuscripts in my PhD program. The group IV transition metal nitrides have shown the possibilities as better alternatives courtesy of their unique characteristics such as exhibiting both metallic and semiconducting properties, possessing ceramic hardness, high thermal tolerance and chemical resistance. All these advantages have shown the possibility for substitution of plasmonic noble metals. These two manuscripts included in the thesis are "Femtosecond and Picosecond single pulsed laser ablation of Nonlinear Optical TiN, as alternative for gold" and "Core-Shell TiO_2@HfN Nanotube Arrays: Hot Carrier Photoanode for Sunlight-Driven Water-Splitting". They investigated the optical and material properties of TiN and proved the promising performance of HfN as photocatalyst for water-splitting.

Preface:

All works presented in this thesis were completed at the Department of Electrical and Computer Engineering, University of Alberta.

Chapter 2 has been adapted from a published review article, Zeng, Sheng, Piyush Kar, Ujwal Kumar Thakur, and Karthik Shankar. "A review on photocatalytic CO_2 reduction using perovskite oxide nanomaterials." Nanotechnology 29, no. 5 (2018): 052001. I was responsible for the literature review, design and writing of the manuscript with the assistance from Piyush Kar. Ujwal Kumar Thakur contributed to manuscript writing and review. Karthik Shankar was supervisory author.

Chapter 4 has been published as a research article, Zeng, Sheng, Ehsan Vahidzadeh, Collin G. VanEssen, Piyush Kar, Ryan Kisslinger, Ankur Goswami, Yun Zhang et al. "Optical control of selectivity of high rate CO_2 photoreduction via interband-or hot electron Z-scheme reaction pathways in Au-TiO_2 plasmonic photonic crystal photocatalyst." Applied Catalysis B: Environmental 267 (2020): 118644. In this work, I designed and performed the experiments, analysis of the results and composed the manuscript. Ehsan Vahidzadeh, Collin G. VanEssen helped with sample fabrication and data collection. Piyush Kar, Ryan Kisslinger, Ankur Goswami, Yun Zhang, Najia Mahdi, and Saralyn Riddell contributed to data collection and provide theoretical insight for data analysis. Pawan Kumar guided for experiments design and contributed to manuscript edits and review. Alexander E. Kobryn and Sergey Gusarov performed DFT modeling and manuscript edits, Karthik Shankar was supervisory author.

Results presented in Chapter 5 are from a well-established manuscript that will be a published scientific article soon. The manuscript title is “Femtosecond and Picosecond single pulsed laser ablation of Nonlinear Optical TiN, as alternative for gold”. And following is the authors’ contributions in this manuscript: I was responsible for experimental design, data collection and analysis, and manuscript composition. Ruoheng Zhang was the person conducted laser ablation tests, Najia Mahdia and Saralyn Riddella helped in sample fabrication, Ehsan Vahidzadeh and Yun Zhang assisted in characterization of samples. Robert Fedosejevs, Ying Tsui, and Karthik Shankar were the supervisory authors.

Chapter 6 of this thesis was adapted from a submitted research manuscript that has not yet published as of the time I am writing this thesis. The manuscript is titled “Core-Shell TiO_2@HfN Nanotube Arrays: Hot Carrier Photoanode for Sunlight-Driven Water-Splitting”. I planned and conducted all experiments, data analysis and manuscript composition. Triratna Muneshwar conducted atomic layer deposition. Saralyn Riddell assisted in sample fabrication. Ajay P Manuel conducted Lumerical FDTD simulation. Ehsan Vahidzadeh and Ryan Kisslinger contributed to data collection. Pawan Kumar provide scientific insights for data interpretation. Kazi M. Alam performed DFT modeling, Ken Cadien and Karthik Shankar were supervisory authors.

Acknowledgements:

First of all, I would like to express my sincerest thank to my supervisor Professor Karthik Shankar for all the brilliant guidance, excellent suggestions, and constant encouragement to me all along the Ph.D. program. I consider myself very fortunate for taking his offer in Dec 2016 and being supervised by him throughout my Ph.D. research studies. He is always tirelessly providing in-depth and enlighten discussion, sharing of his exceptional scientific knowledge, and spurring me on to a higher standard and a greater effort. I wouldn't be qualified enough to start next chapter of my life without all of these from him.

I am grateful to Prof. Ken Cadien and Prof. Ying Tsui, members of my supervisory committee, for giving me all kinds of support whenever I required and encouraged me to accomplish my research projects. I extremely thank to Prof. Xihua Wang for his mentorship who helped me in many aspects as an instructor of a wonderful course, a referrer for my scholarship and an extension of committee member for my research projects. I would also like to thank Prof. Manisha Gupta for her support and patience during my candidacy exam. I especially want to show my gratitude to Dr. Alexander E. Kobryn from National Institution of Nanotechnology, the first person who taught me DFT modeling and was always being helpful to me.

I profusely thank to all my lab mates who made my research enjoyable and experimented alongside me. They are Aarat Kalra, Ajay Peter Manuel, Ehsan Vahidzadeh, Ryan Kisslinger, Saralyn Riddell, and Ujwal Kumar Thakur. They all gave me all sorts of help as much as they can during my graduate study. I wish all alumni in our lab best in their future endeavors, and thank for the cheerful memories to Ben Wiltshire, Weidi Hua, Najia Mahdi, Yun Zhang, Lintong Bu, Arezoo Hosseini, Lian Shoute, Sahil Patel, and Collin VanEssen. Postdoctoral fellows, Kazi Alam and

Piyush Kar were always willing to help me and guide me without reservation. A special thank from the bottom of my heart to Dr. Pawan Kumar for being a friend and a teacher to me. He inspired me with his extraordinary knowledge and made this thesis possible.

Finally, I would like to express my gratitude and love to my family. I thank them for sharing the warmth and joy of family with me, and apologize for being absent and not fulfilling family obligations due to studying abroad. My dad is the person always standing behind me with love beyond words and my mon always give me her greatest love and kindness without beginning and ending. I am greatly indebted to my girlfriend for her unfailing love, thoughtfulness, support and understanding.

There is an old Chinese poem saying: the sharp edge of a sword comes out from grinding, and plum blossom's fragrance comes from the bitter cold. I finally understand that all the efforts and hardships eventually turn into the fertile soil for the bloom of future.

Table of Contents

List of Figures:

List of Tables:

1. Introduction

1.1. Solar Energy Harvesting

Modern industrial civilization is heavily reliant on energy, which is predominantly supplied by fossil fuels at the moment. While fracking-related new oil production and the COVID-19 pandemic-related loss of energy demand caused crude oil prices to crater, underneath the apparent volatile and promptly rebounded crude oil prices, it is the hidden battle that energy remains the must-competing interest for countries[1]. Energy demand remains a top issue on humanity's problem list for the next half century[2]. The shortage of energy will deteriorate other issues, because each of them is closely corelated together. For instance, population expansion increases energy consumption[3]; to overcome the energy deficit, it will give rise to environmental problems including but not limited to pollution, disease; however, if the energy shortage cannot be addressed properly, even more notorious problems will emerge such as famine, poverty, and wars[1]. While the global energy demand is 162494 TWh (13972 million tonnes of oil equivalent) in 2017[4], the projection according to International Energy Agency (IEA) indicates that the total energy demand increases to 224784 TWh (19328 million tonnes of oil equivalent) by 2040[5]. To solve those tightly connected problems, solar energy is a clean, inexpensive, sustainable approach for anywhere on the earth illuminated by the sun. Considering sun as a blackbody with a temperature of 5800 K, the radiant power density of the sun is 5.961×10^7 W/m^2 according to Planck radiation low[6], which means 1.36 kW/m^2 solar irradiance incident on the earth's surface. Further calculation will tell us that the annual solar radiation on earth's surface is 6,000 times greater than the entire global energy demand.

After decades of efforts from scientists, the technology and economics of conversion of solar energy into electricity have achieved conspicuous progress[7, 8]. Today, the energy payback time of a photovoltaic system is approximately 1-4 years depending on the geographical location and the type of solar cells. For example, the energy payback time for a polycrystalline silicon solar cell in Arizona could be roughly 2-4 years while a thin-film solar cell can recover the pollution from its production and generate pure clean electricity after the first year. Moreover, the capital costs per kilowatt-hour of solar PV is approaching fossil fuel costs closely. Some places in Spain and Germany even have a surplus of power generated from solar energy during off-peak hours of the daytime.

However, the pros and cons of solar PV are on the table[9]. Obviously, solar PV cannot provide electricity during the night or on a cloudy day. An alternative solution is a solar thermal system that can store solar energy as thermal energy and use it during the night. Many countries are developing solar photovoltaic and solar thermal technologies simultaneously[10]. However, a solar thermal system also has its own limitations[11]. For instance - the installation is costly, it cannot be used to generate power, and thermal energy cannot be stored for long[12].

Due to such limitations of solar PV and solar thermal energy, scientists are eager to explore new methods. Photosynthesis and photocatalysis are inspired by the omnipotent nature[13]. The Hydrogen economy is an actively discussed solution, considering hydrogen is energy intense, clean and easy to store and transport. In this application, hydrogen and oxygen are generated from the splitting of water driven by sunlight. Another novel application, CO_2 photoreduction, is one of the most attractive artificial solar driven reactions[14]. Both photocatalytic hydrogen generation and CO_2 to hydrocarbon process are inspired by countless photosynthetic models from nature as

shown in Figure 1. For example, sugarcane can convert CO_2 to cane sugar reaching storage efficiency around 8%. CO_2 photoreduction can capture rapidly increasing CO_2 and store solar energy in higher energy compounds such as short chain hydrocarbons and alcohols, which kills two birds with one stone. This means the ultimate goal is to close the carbon loop such that any CO_2 released from solar carbon fuels is originally produced by CO_2 as a fuel feedstock. The advantages of photocatalytic CO_2 reduction are obvious: 1) It captures and recycles greenhouse gas in the atmosphere, 2) Solar energy can be stored for a long time and generate power during night, 3) Products are energy intense and easily transportable, 4) It synthesizes high value chemicals for industries. In conclusion, photocatalysis opens the window to a wider range of applications including solar-to-chemical energy storage, water purification etc. The urgency of global problems including global warming and environmental pollution fuels accelerates the need for greater research into photocatalysis.

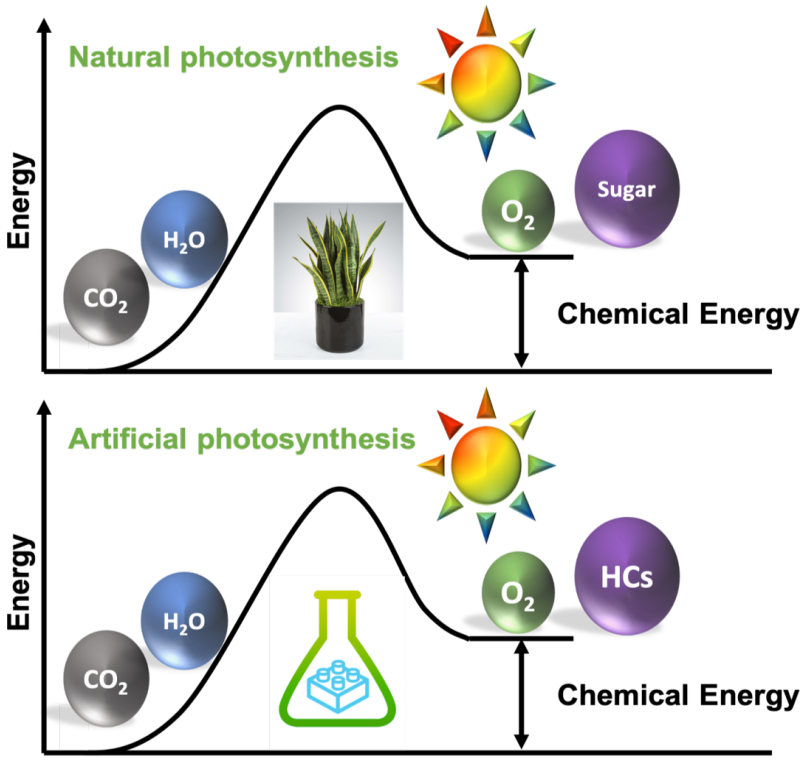

Figure 1: Schematics of natural photosynthesis by green plants and artificial photocatalytic water splitting.

The next question will be how to connect solar radiation to the concept of energy use on a daily basis. Figure 2 demonstrates the solar spectrum in irradiance vs. wavelength. From wave-particle duality of light, light can be both described as an electromagnetic wave and a quantum-mechanical particle also known as photon. The wavelength of light is inversely proportional to the energy of a photon.

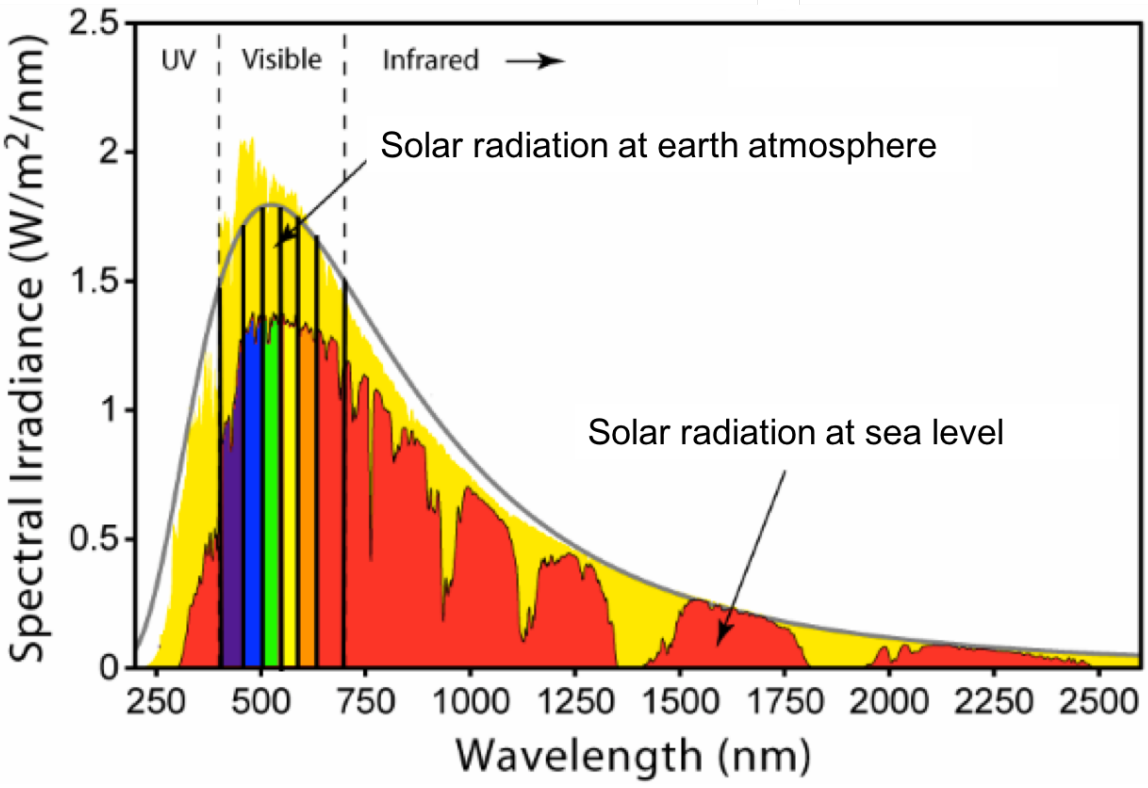

Figure 2：Solar spectrum at earth atmosphere vs. at sea level.（Data from American Society for Testing and Materials (ASTM) G-173-03 reference spectra）

Once the energy of a single incident photon is obtained, the power density of irradiance can be calculated by multiplying the energy of a single photon by the number of photons per unit area per second called photon flux. When a photon striking on a semiconductor has an energy larger than the band gap, it will be absorbed by this material and produce an excess electron-hole pair. The

photo-generated electrons can be utilized either for generating electricity by photovoltaic devices or for providing energy for photocatalytic reactions.

1.2. Photocatalytic CO_2 Reduction

In general, scientists have been investigating four approaches to capture wildly increasing CO_2 concentrations in the atmosphere: 1) Carbon capture using amines; 2) High temperature reduction; 3) Electrochemical reduction; 4) Photocatalytic reduction. Among all these methods, CO_2 photoreduction stands out due to its ability to store solar energy and reduce CO_2 concentration in the atmosphere simultaneously. Nature creates a balance of carbon resources in ecosystems, however, this balance has been destroyed by anthropogenic interference. Although the UNFCCC treaty has prevented reckless GHG increases[15], 2017 global CO_2 emissions were still 37 $GtCO_2$[16] and the atmosphere CO_2 concentration was 405 PPM[17]. This environmental disruption will last for over a thousand years[18]. Photocatalytic CO_2 capture is an ideal approach to close the anthropogenically opened carbon loop and rebalance the carbon emissions like what nature did through photosynthesis. In general, photocatalytic reduction of CO_2 needs a semiconducting material as a photocatalyst and involves H_2O or H_2 as reagents to transform CO_2 into hydrocarbon products. This process, in which multiple electrons/holes are needed, consists of three steps and is similar to the photovoltaic process: 1) Creation of photogenerated charge carriers in semiconducting photocatalysts by illumination; 2) Migration of charge carriers to the surface of photocatalysts; 3) Utilization of charge carriers on adsorbed CO_2/H_2O for forming hydrocarbon products. The most common products are CO, HCOOH, HCHO, CH_4, CH_3OH, multi-carbon compounds, etc. However, carbon dioxide is one of the most inert and stable molecules. To breaking down the C=O bonds and bending its linear geometry, the process requires large amount

of energy and existing of catalysts. For example, the formation of methane from CO_2 needs additional 818.3 kJ/mol in Gibbs free energy, much higher than the 237.2 kJ/mol required to split H_2O to H_2 and O_2.

Furthermore, let's consider whether a semiconductor is thermodynamically favored to be a potential photocatalyst for CO_2 reduction. As shown in Figure 3[19], to be able to complete a reaction, electrons in the conduction band of this semiconductor should be more negative than the reduction potential of a particular reaction. Meanwhile, holes in the valence band of this material should be oxidative enough to split H_2O molecules. Most notably, turning stable CO_2 into a $CO_2^{\bullet-}$ intermediate, as a most recognized first step of CO_2 reduction, requires -1.9 V vs. NHE, which is more negative than most conduction band of typical semiconductors. Therefore, scientists

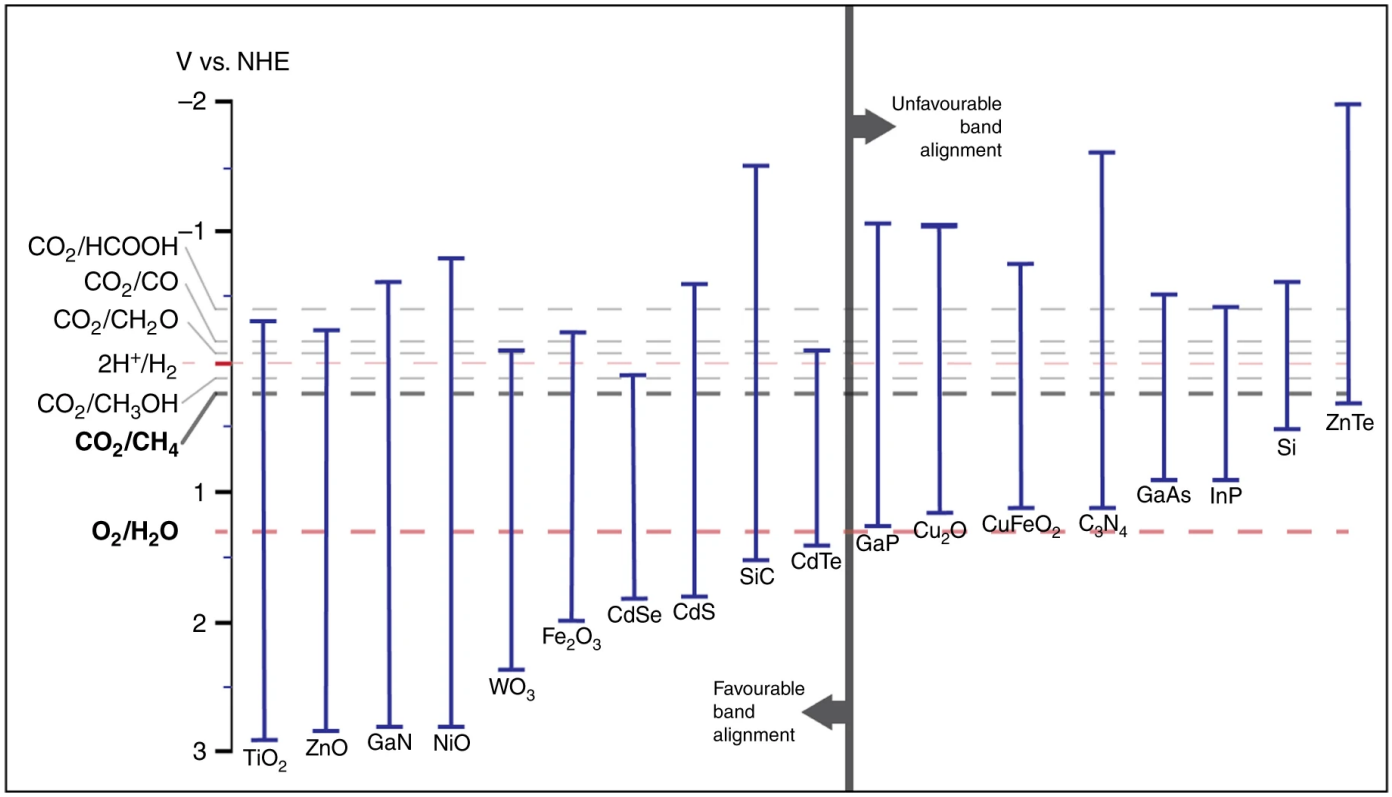

Figure 3: Energy band diagram of typical catalytic semiconductors and the energy levels of redox reactions in CO_2 to hydrocarbon fuels process. Reprinted with permission from [19]; ***copyright*** *Springer Nature 2019.*

proposed widespread process, proton-assisted transfer of multiple electrons, to bypass the high transition state of forming $CO_2^{\bullet-}$ intermediate. The possible reactions for photoreduction of CO_2 and their standard potential required with respect to the normal hydrogen electrode are listed in Table 1. However, this is only a thermodynamic premise. While in real world, there are countless factors that limit the transformation of CO_2.

Table 1: Common redox reactions related to photoreduction of CO_2 and their required potential with respect to NHE at pH7.

Reactions	Reduction potential vs NHE (pH=7)
$2H^+ + 2e^- \rightarrow H_2$	-0.41
$H_2O + 2h^- \rightarrow {}^1/_2\, O_2 + 2H^+$	0.82
$CO_2 + 2H^+ + 2e^- \rightarrow CO + H_2O$	-0.53
$CO_2 + 2H^+ + 2e^- \rightarrow HCOOH$	-0.61
$CO_2 + 4H^+ + 4e^- \rightarrow HCHO + H_2O$	-0.48
$CO_2 + 6H^+ + 6e^- \rightarrow CH_3OH + H_2O$	-0.38
$CO_2 + 8H^+ + 8e^- \rightarrow CH_4 + 2H_2O$	-0.24

Among many hypothetical pathways for CO_2 photoreduction, the two which are most accepted by scientists, are the formaldehyde path and the carbene path[14, 20]. Most detailed studies indicated that, depending on how CO_2 is adsorbed on the surface of catalysts, a preferred pathway will be employed. Initially, CO_2 activation is the very first step for any pathway, which forms the surface-bonded $CO_2^{\cdot-}$ radical anion via a one electron accepting process. For example, in the formaldehyde pathway, it is oxygen atoms in CO_2 which bind to the surface of the catalyst through oxygen coordination. Since the carbon atom in this case is exposed, this process sequentially forms formic acid, dihydroxymethyl radical by adding hydrogen atoms to CO_2 instead of cleaving the C-O bond.

Then after adding one more hydrogen atom, formaldehyde is formed by dehydration. Further reducing reactions produce methanol and methane via inserting hydrogen radical and dehydration sequentially. On the other hand, when the carbon atom of CO_2 is anchored on the surface of the catalyst in the process named carbon coordination, the carbene pathway is preferred because in this case oxygen atoms are exposed and likely bond with $H^{\cdot}$. This pathway has a straightforward process that involves attaching $H^{\cdot}$ to oxygen atom and cleavage of the C-O bond. The most common products in this pathway are carbon monoxide and methane, yet methanol is also possible.

Last but never the least important step is to define the efficiency of photocatalytic CO_2 reduction. The most commonly used measurement of photocatalytic activity is the rate of formation of products. Typically, it is the amount of product in each type formed in the unit of time divided by the total amount of catalyst used. The unit for amount of product is normally in mmol or ppm, while the amount of catalyst can be quantified by either mass or area, for example, mmol cm^{-2} $hour^{-1}$ or ppm $gram^{-1}minute^{-1}$. Another popular used measurement is turnover number, the amount of product to the number of active catalytic sites. However, the number of active sites is difficult to be quantified accurately. Thus, the active surface area measured by Brunauer-Emmett-Teller is an alternative to present the number of active sites. However, it is also not accurate due to not all active surface can be exposed to reagents and illuminated by light. Despite the mentioned problems, the turnover number is used to determine whether the products are from catalytic reaction or stoichiometric chemical reaction. Moreover, some measurements which are used in other light interacting processes are also adopted for photocatalytic CO_2 reduction, for example, external quantum efficiency (EQE), and absorbed photon to electron conversion efficiency (APCE),

In conclusion, although photocatalytic CO_2 reduction is challenging, it is still a promising approach to close the carbon loop, considering the following advantages: 1) Components involved in process are earth abundant CO_2, H_2O and inexhaustible solar energy; 2) Alleviation of GHC-caused global warming crisis; 3) Balancing CO_2 emission by recycling and producing hydrocarbon fuels to substitute conventional fossil fuels; 4) Storing solar energy for easy transportation and later usage.

1.3. TiO_2 nanotube arrays

TiO_2 nanotube arrays (TNT) are self-organized, highly-ordered, vertically tubular nanostructure made by electrochemical anodization (shown in Figure 4 [21]). Later in thesis, the detail of growing TiO_2 nanotubes will be discussed either on native (Ti foil) or non-native (conductive glass) substrates. Compare to anodic alumina nanoporous structure, it indicates much higher refractive index, more flexibility in geometry and great electronic properties. It has been well utilized in solar cells as electron transport layer, because of its excellent anisotropic property, which is the long vertical light absorption path and short horizontal charge transport path. An explosion of

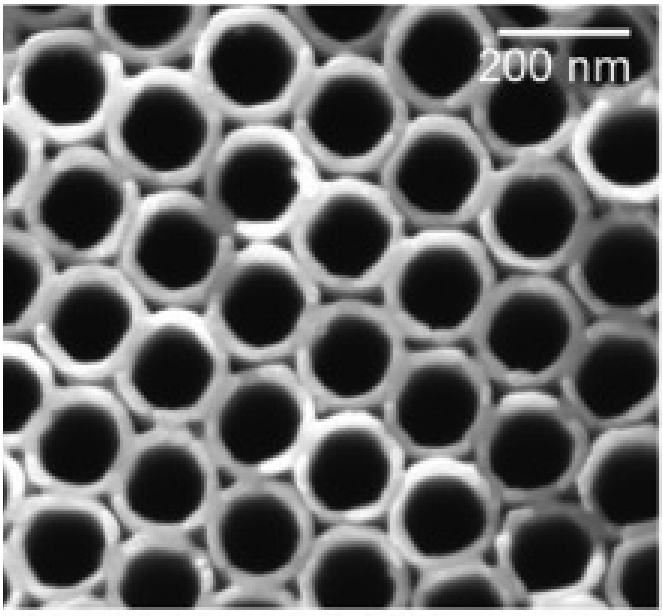

Figure 4: A top view of SEM image of the TiO_2 nanotube arrays. Reprinted with permission from Ref [21]; copyright 2012 Wiley .

research has been achieved on this architecture and leads to narrower band gap, stronger light absorption, longer carrier life time, more functional dexterity and much more. Due to these benefits, the application of TNT has been expanded to photocatalysts, biosensor, supercapacitors, coating material and nanophotonics etc.

1.4. Fabrication techniques

There are countless methods developed by scientists for fabrication nanostructures ranging from atomic layer thin film to 3D architectures. Considering the limited space of this thesis, I focus the discussion within three main methods used in my research for fabrication, namely anodization, sputtering and atomic layer deposition.

1.4.1. Anodization

Anodization is an electrochemical oxidation and etching process for surface treatment, which is well-known simple and cost-effective. The first anodization utilization was developed in early 20th century for aluminum protective film[22]. At the beginning, anodization method was merely utilized on aluminum for corrosion protection until the technique became matured. Today, it has been widely used for a large variety of materials (Al, Ti, Ge, Fe, Hf, Ta, Ni, and so on) to create vertical, highly-ordered, self-organized, nanoporous structures.

Taking titanium dioxide nanotube as an example, the anodization process consists of four chemical reactions simultaneously happening in the electrolytic cell, listed as following:

Field assisted oxidation:

$$\mathrm{Ti} + 2\mathrm{H_2O} \rightarrow \mathrm{TiO_2} + 4H^+ + 4e^- \qquad (1.)$$

Field assisted migration:

$$\mathrm{Ti}^{4+} + 6F^{-} \rightarrow [\mathrm{TiF}_6]^{2-} \quad (2.)$$

Field assisted dissolution:

$$\mathrm{TiO}_2 + 6F^{-} + 4H^{+} \rightarrow [\mathrm{TiF}_6]^{2-} + 2\mathrm{H}_2\mathrm{O} \quad (3.)$$

Chemical dissolution:

$$\mathrm{TiO}_2 + 6\mathrm{HF} \rightarrow [\mathrm{TiF}_6]^{2-} + 2\mathrm{H}_2\mathrm{O} + 2H^{+} \quad (4.)$$

The above-mentioned reactions are driven by an anodic voltage within an electrolytic cell which has an anodic sample electrode and a counter electrode (shown in Figure 5). The process has three sequential stages. It starts from oxide formation followed by a fluoride pitting of the newly formed oxide layer. Finally, an equilibrium is settled between the oxide formation and oxide etching. As a result, the nanotube titanium dioxide layer can be established by the continuous "digging" at the interface of metal and oxide. Many variables are related to adjustment of anodization process such as electrolyte compositions, voltage, current, pH value, temperature etc. Typically, the anodization can be categorized into two modes, i.e., potentiostatic mode and galvanostatic mode. In

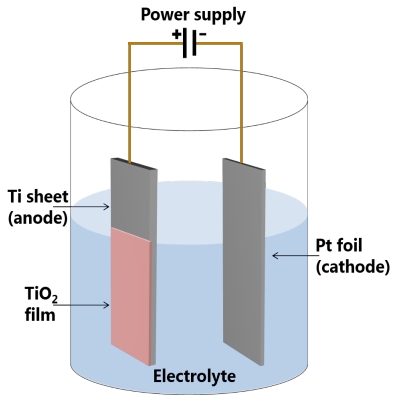

Figure 5: A schematic of anodization in an electrolytic cell for growing TiO_2 nanotubes.

potentiostatic mode, a constant anodic voltage is applied throughout the anodization process, while in galvanostatic mode, it keeps the anodizing current constant by varying anodic voltage.

1.4.2. Sputtering deposition

Sputter has been utilized for decades and recognized as a reliable, dexterous and effective method. Generally, it can be categorized as dc discharge sputtering, RF sputtering, magnetron sputtering, and reactive sputtering. In our fabrication process, we mainly use magnetron sputtering technique which has been widely employed since 1960s. A sputtering tool can be used for either deposition or erosion of material. Throughout this thesis, we only discuss material depositing due to our research scope. Technically, a cathode target which is the source of material is under the bombardment of an ionized gas molecule. Then sputtered off material flies across the chamber to adsorb on an arbitrary substrate. In our research related to this thesis, we mainly use sputtering to form metal nanoparticles for localize surface plasmon resonance or to deposit a Ti thin film for subsequent anodization. A large number of parameters are involved to vary the morphology and quality of the deposited material, such as pressure, substrate temperature, target current and voltage, distance between target and substrate, carrier gas. For instance, to obtained highly-ordered TiO_2 nanotubes on conductive glass by anodization, it requires a denser and uniform Ti film which need lower sputtering pressure and high substrate temperature. On the other hand, the metal nanoparticles that we obtained from sputtering require moderately high sputtering pressure and avoid substrate heating.

1.4.3. Atomic layer deposition

Atomic layer deposition (ALD) has become an inevitable technique for fabrication of microelectronics, optoelectronics, batteries, and memory devices. Additionally, it has been widely employed as a routine tool in the research field of nanomaterials, such as surface passivation, tunnelling layer, surface doping. The pool of ALD materials expands rapidly ranging from metal (Ni, Au, Ag, Cu, Ge, Li, Mg, Fe, Co, Zn and more) to oxides and nitrides (including and not limited to TiO_2, ZnO, SiO_2, Al_2O_3, WO_3, ZrO_2, HfO_2, In_2O_3, V_2O_5, Ta_2O_5, AlN, ZrN, HfN). The expanding of material library in ALD appreciates the developing of suitable chemical precursors, which need to fulfill many requirements such as sufficient vapor pressure, thermal stability, appropriate volatility, suitable functional group and self-limiting behavior. In our research, plasma enhanced atomic layer deposition is the only type of ALD employed and can be consider as a variation of plasma enhanced chemical vapor deposition. During a deposition cycle, the first precursor is introduced to the reaction chamber and adsorb on the surface of substrate to form a monolayer. After remove excess of the first precursor, the second pulse carriers the co-reactant into the chamber also in a self-limiting manner. Then the plasma is ignited with the existing of both reactants. The final stage is a post-plasma purge and ready for the next deposition cycle. Later sections will discuss the experimental details of ALD and illustrate its utilization and advantages.

2. A Review on Photocatalytic CO_2 Reduction using Perovskite Oxide Nanomaterials

Perovskite now has been recognized as one of the most important class of material. But it is not as popular as it was discovered by the German scientist Gustav Rose and named in honor of the Russian mineralogist Lev Perovski. Perovskite oxides share the same formula of ABX_3 in which X is oxygen. Because the large variety of chemical composition within the class of perovskite oxides, there are many advantages are well-known, including but not limited to ferroelectricity, magnetism, superconductivity, catalytic activity. Considering perovskite oxides have become significantly important and popular in the field of catalysis, the major question in this project is "what are the beneficial effects of perovskite oxides that make them become good catalysts especially in CO_2 photoreduction?"

2.1. Introduction

Excessive CO_2 emission by human activities has the potential to dramatically change our environment. Anthropogenic CO_2 emissions are implicated in phenomena such as global warming, acid rain, and a rising sea level. Figure 6 shows that there is a strong correlation between CO_2 concentration and global temperature for the past few decades[23]. The International Panel on Climate Change predicted that the global temperature will rise 1.9 ℃ in mean value if CO_2 rises to 590 ppm by 2100, which will have serious climatic impact [24]. This makes it imperative to find methods to mitigate CO_2 emissions and also to replace an increasing portion of fossil fuels by renewable sources to meet global energy demand. Several methodologies have been demonstrated for CO_2 conversion to light hydrocarbons, and these include photocatalytic reduction [25-34], electrochemical reduction [35, 36], photoelectrochemical reduction and thermochemical reduction

[37-40]. Among the common methods, photocatalysis, is preferred since it only requires solar radiation as an energy source and has been proven effective in various applications[41-44], including water splitting[45-48], H_2O_2 production [49, 50], pollutant degradation [51, 52], and N_2 fixation[53-58]. Various types of photocatalyst materials being used for CO_2 reduction at present include oxide and non-oxide semiconductors[59, 60], non-titanium metal oxides and sulfides[61-63], and metal-free materials[64, 65], molecular catalysts [66, 67], and other/diverse catalysts[68-77]. However, matching photocatalytic conversion rates of CO_2 with the rates of CO_2 production using existing technology remains a daunting challenge, which is driving researchers to pursue new materials and designs for the technology. Perovskites are new materials that are constituted of earth-abundant elements and are technologically important from the standpoint of photovoltaics[78-80] and CO_2 photoreduction[81-83]. A good example high performance of perovskite based CO_2 photoreduction is reported by Xu and co-workers[83].

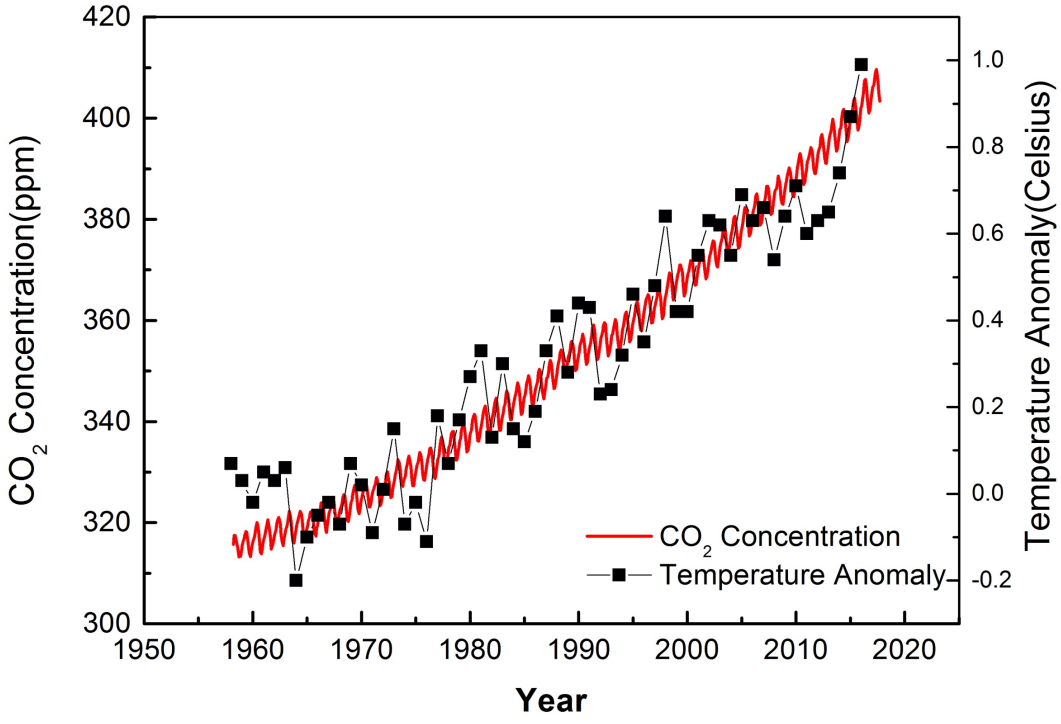

Figure 6: Correlation of global temperature with CO_2 concentration from 1958 to 2017. Data is sourced from U.S. Department of Commerce's National Oceanic and Atmospheric Administration, NASA's Goddard Institute for Space Studies [23] .

In this review, we focus on the latest advances in the development of perovskite oxide nanomaterials and their use in photocatalytic CO_2 reduction. Technologically important considerations for researchers' focus on perovskite oxides [84-89] include their scientific potential due to their unique properties like superconductivity [90-94], magnetic properties [95-99], ferroelectric abilities [100], multiferroicity[101] and catalytic capability [102, 103]. Compared to other heterogeneous photocatalysts, perovskite oxides have more suitably positioned energy bands for CO_2 reduction, and are adaptable to easy engineering of the bandgaps. One clear metric in which perovskite oxides have advantage over a number of other state-of-the-art nanomaterials, such as ZrO_2 (5.0 eV), Nb_2O_5 (3.8 eV), Ta_2O_5 (4.0 eV), Ga_2O_3 (4.6 eV) and GeO_2 (5.5 eV) is their lower bandgap [104, 105] which enables them to harvest a greater fraction of photons in terrestrial sunlight. Considering all these above factors, band engineered perovskite oxides are being actively studied for photocatalytic CO_2 reduction.

Perovskite oxides have the general formula ABO_3 and possess a crystal structure wherein A cations occupy cuboctahedral interstitial sites in BO_6 octahedra; the BO_6 octahedra share corners and are typically arranged in a cubic array. Perovskite oxides can have various band structures and photophysical properties [106] based on the composition of elements used in the A and B sites. Compared to wide band gaps in binary oxides, perovskite oxides provide a variety of band gap selections, which allows visible light absorption [107]. Moreover, perovskite oxides usually show better charge carrier separation due to the higher lattice distortion as compared to traditional binary oxides [106]. However, morphology and the catalyst/reactant interface are also important factors for photocatalyst candidates.

Several review papers on perovskite oxides have been published in the last decade, particularly in the recent years[108-110]. Wang *et al* recently summarized progress of perovskite materials in photocatalysis and photovoltaics including water-splitting, degradation of organic dyes, and solar cells [111]. Grabowska *et al* reviewed the preparation, characterization and applications of select perovskite oxides. Besides basic information, Grabowska's review paper also discussed doping effects and the influence of morphologies and surface properties [106]. Li *et al* published a review paper on latest progress and key factors for high efficiency CO_2 photoconversion [112]. However, none of these aforementioned review articles carefully examine CO_2 reduction using perovskite oxides. The present review paper attempts a comprehensive understanding of photocatalytic CO_2 reduction using perovskite oxide materials. The layout of this paper is as follows: material relevant information including preparation, structure, morphology and bandgap engineering, followed by a summary of CO_2 photoreduction mechanism and performance, and finally an exploration of the future of perovskite oxides in this area.

2.2. Mechanism of CO_2 reduction

2.2.1. Charge separation band energetics of perovskite oxides

For feasibility of use as photocatalysts, perovskite oxide nanomaterials must have suitable band energetics, and must be stable against photocorrosion, inert (biologically and chemically), inexpensive and nontoxic. When light is incident on a peroxide oxide semiconductor, with a photon energy that is higher than or equal to its bandgap (E_g), absorption of the photon occurs, resulting in the transition of an electron from the valence band to the conduction band and the creation of a hole in the valence band (Figure 7). The reduction potential of a photoexcited electron is the energy level at the bottom of conduction band, and the oxidizing power of the hole is

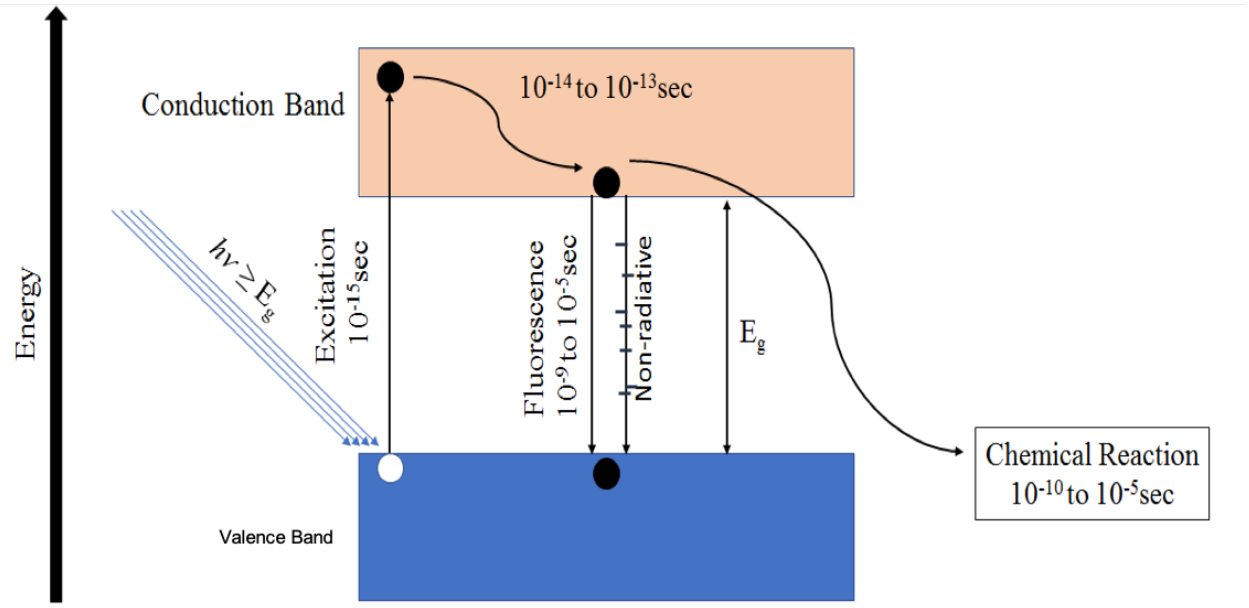

Figure 7: Schematic illustration of Excitation and deexcitation process in semiconductor after illumination with photons having energy higher than the bandgap of semiconductor.

determined by the top energy level of the valence band. In a typical photochemical reaction, photogenerated electrons and holes are separated and they migrate to the surface of photocatalyst, where electron transfer reactions between near-surface species and charge carriers occur [78, 112]. For CO_2 reduction in the presence of water, the valence band position of the perovskite oxide nanomaterials should be below the redox potential of water, and the position of conduction band of the same should be above of the redox potential of the CO_2 [110, 113, 114]. Therefore, perovskite oxide nanomaterials with suitable band alignment for oxidation of water at the valence band and reduction of CO_2 at conduction band can facilitate redox reaction before excited charge carriers undergo recombination.

Excited electrons in perovskite oxides typically undergo de-excitation and follow a pathway that minimizes the lifetime of excited states. Among common causes of minimization of lifetime of separated charges in perovskite oxide nanomaterials are: radiative/nonradiative recombination [42, 109, 110] whereby separated charges get trapped in metastable surface states, and reactions of

electron acceptors and donors that are present on the surfaces of perovskite oxides. Absorption of the incident photon and excited state creation occur in the femtosecond time range, while de-excitation typically occurs at picosecond/nanosecond timescales. Owing to the thermodynamics of CO_2 reduction as discussed above, there is wide variability in the performance of perovskite oxide nanomaterials, as presented in Table 3.

2.2.2. Reductants and products

There are reports of H_2 based CO_2 reduction reaction and the same with water vapor. Of practical interest, however, is to perform the CO_2 photoreduction reaction in presence of water vapor [113-116] because H_2 is high reactive and difficult to handle. In both H_2 and water vapor atmosphere, the CO_2 reduction initiates by oxidation of H_2 or water to release protons. The protons react with CO_2 to form different reduction products.

CO_2 is a very stable molecule and that necessitates its activation prior to its reduction reactions. CO_2 is activated by adsorption into electron rich oxygen vacancy defect sites on semiconductor surfaces, where the straight CO_2 molecule gets converted to its bent variant, i.e. $CO_2^{\delta-}$ [117]. This is likely the mechanism for activation of CO_2 in perovskite oxides. The other possible mechanism for CO_2 activation is by gain of electrons by CO_2 from photo-excited electron-hole centers in semiconductors. Both of the above mechanisms can co-exist and therefore occur simultaneously. A schematic of the CO_2 photoreduction process, using perovskite oxides is given in Figure 8, where the energetics of reduction of CO_2 and reduction products formed thereof, are given [62]. Considering the more reactive nature of $CO_2^{\delta-}$, it can participate in the reactions shown in Figure 8. $CO_2^{\delta-}$can enable the formation of hydrocarbons through carbene and formaldehyde pathways [117]. In the carbene pathway, $CO_2^{\delta-}$ gets converted into CO by one step electron reduction which

is further reduced to ·C, i.e. the carbon radical. The ·C radical gains electrons from perovskites and reacts with protons formed by water oxidation to form ·CH, $\cdot CH_2$ and $\cdot CH_3$ as intermediates, and CH_4 as the final product. The formaldehyde pathway does not involve formation of CO and the carbon radical (·C); instead, $CO_2^{\delta-}$ gets directly converted to CH_2O, HCOOH, CH_3OH and CH_4. The carbene pathway is more likely to occur on electron rich perovskite oxide surfaces, while the formaldehyde pathway is more like to occur on electron deficient perovskite oxide surfaces.

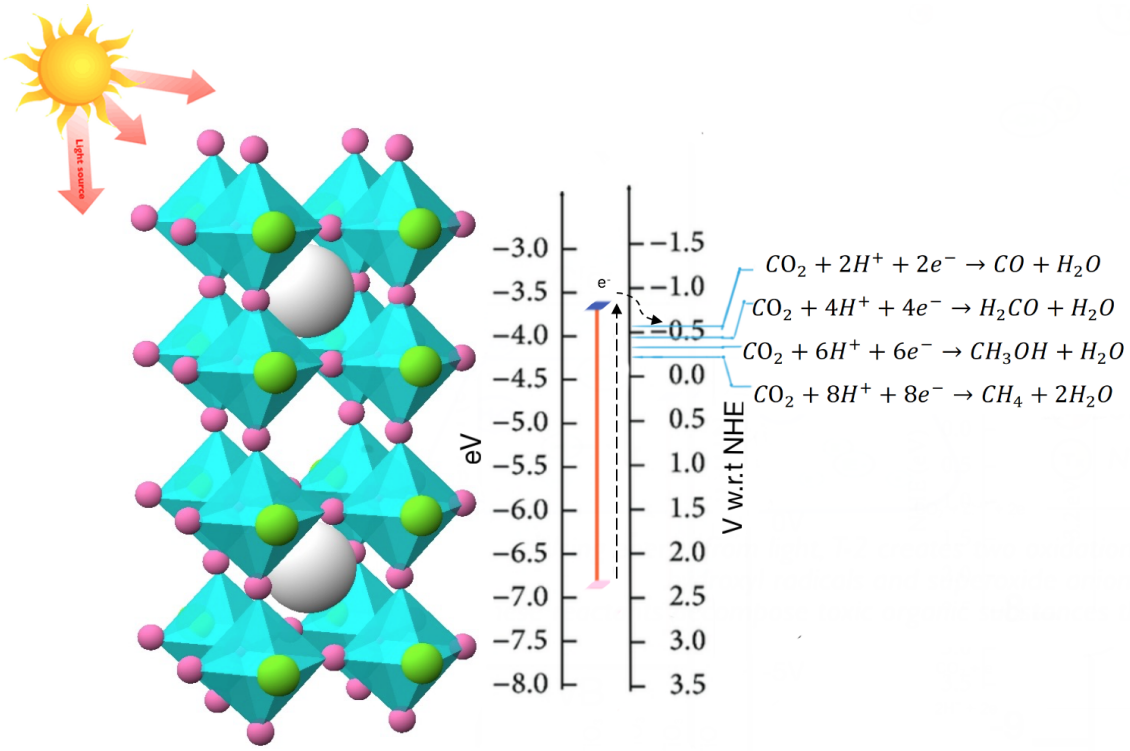

Figure 8: Reaction energetics for the transformation of CO_2 into hydrocarbons and intermediate products. The figure shows a cartoon of perovskite oxide nanomaterials under illumination.

Besides the formation of methane as we discussed above, many other products are commonly formed via CO_2 reduction. These products are mainly CO, and light hydrocarbons such as ethane, acetylene, ethylene, methanol, formaldehyde and formic acid [118, 119]. Carbon monoxide is one of most major gaseous products. The reaction pathway of CO_2 to CO was proposed by Hori et al at 1994 [120], which entails one electron reduction of CO_2 to form CO_2^- radical and reaction of

the same with proton to release CO. The source of proton being water vapour in the reactor, which gets oxidized at the valence band of perovskite oxides.

2.2.3. Isotopic labeling experiments to rule out effect of carbon contamination

Organic chemical precursors are not avoidable in synthesis of photocatalysts, including perovskites. However, those organic residues on photocatalysts are a major concern, because they are a potential cause carbon contamination. The contaminated carbon can react in conditions that are applied in CO_2 photoreduction experiments forming light hydrocarbons and other products that formed by CO_2 photoreduction. To rule out the carbon contamination as the cause of formation of hydrocarbons and other products of CO_2 reduction products, researchers have reported isotopic labelling experiments to track the source of carbon. Isotopic labelling experiments are performed by many researchers using $^{13}CO_2$ instead of regular CO_2. Methods, such gas chromatography mass spectrometry (GC-MS) [81, 121, 122] and nuclear magnetic resonance (NMR) [123] are used detect and differentiate between obtained using isotopic and regular CO_2.

2.3. Perovskite oxides for CO_2 photoreduction

2.3.1. Synthesis methods

Typical methods to prepare perovskite oxide nanomaterial photocatalysts are listed in Table 2, along with their various pros and cons. The methodology used during preparation impacts the morphology of the material and in turn the photocatalytic process. This is because the preparation method directly affects morphology- and structure-dependent material properties such as defect distribution, electronic properties and surface energy.

Table 2: Conventional methods for preparation of perovskite oxides.

Various methods of synthesis have been studied for identifying suitable morphologies for perovskite oxides nanomaterials [132]. The following section in this article contains examples of synthesis methods for important perovskite oxide nanomaterials, and the corresponding morphologies obtained from them. Kwak *et al* [133] reported a hydrothermal method for synthesizing $Ca_xTi_yO_3$ perovskite oxides (Figure 9). The process flow for the synthesis in shown in Figure 9. In their process, both calcium chloride dihydrate and titanium isopropoxide served as precursors. Based on the stoichiometric proportion, different amounts of calcium chloride dihydrate and titanium isopropoxide were added in solution phase while stirring. Additional sodium hydroxide was added to increase pH. Subsequently, the solution was treated at 453 °K for

Preparation Methods	**Description**	**Ref.**
Hydrothermal methods	Using aqueous solutions to conduct preparation in a high-pressure vessel at moderate-to-high temperatures.	[124]
Solvothermal method	Using non-aqueous solvents instead aqueous solutions in hydrothermal method, typically at a higher temperature.	[125]
Sol-Gel method	Converting monomers into a colloidal solution acting as a precursor to form a perovskite oxide.	[126]
Polymerized Complex method	Using various metal ions in desired stoichiometric ratio to form a polymer complex precursor.	[127]
Solid-state reaction method	Using very high temperatures to facilitate the direct reaction of a mixture of solid materials.	[128]
Molten salt treatment	Using molten salt as the medium to prepare desired perovskite oxide.	[129]
Sonochemical method	Including ultrasound during the synthesis process.	[130]
Microwave method	Using high frequency electromagnetic wave to synthesize a dielectric material.	[131]

8 hours in an autoclave. The precipitate samples were rinsed with distilled water and ethanol, then dried at 343 °K for 24 hours [133].

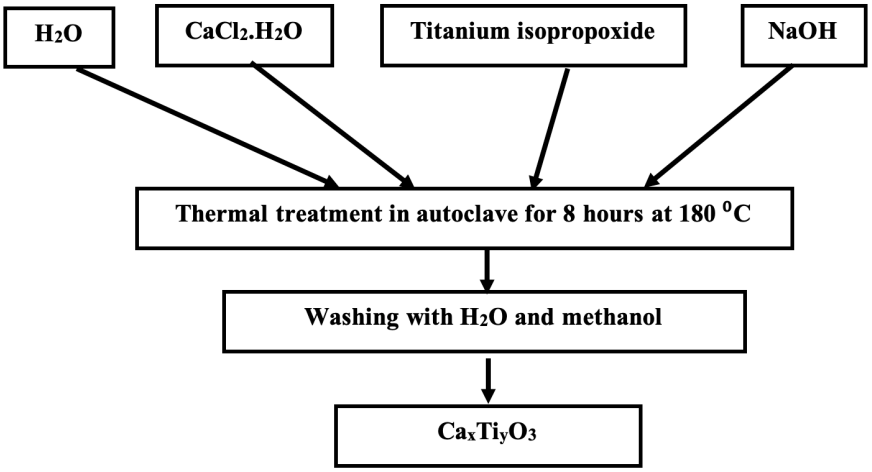

Figure 9:Process flow diagram of preparing $Ca_xTi_yO_3$ using hydrothermal synthesis. Reprinted from [133], Copyright 2015, with permission from Elsevier.

Zheng *et al* and Dong *et al* reported hydrothermal methods (shown in Figure 10) for synthesizing $SrTiO_3$ perovskite oxides of different nanostructured morphologies [134, 135]. Sol-gel synthesis is also a popular method for the preparation of perovskite oxides.

Figure 10: (a) Hydrothermal method for formation of $SrTiO_3$ hollow microspheres, reprinted with permission from Ref 134]; copyright Elsevier (2011) and (b) Growth of porous and solid $SrTiO_3$ using the same method at different operating temperatures. Reprinted with permission from Ref [135]; copyright Elsevier (2012).

Sol-gel formation of $CoTiO_3$ nanoparticles (process flow is shown in Figure 11) using polymeric fugitive agents has the advantage of reducing the nanoparticle size as compared to other methods. Additionally, the process involves introduction of trimeric acid as a polymerization and cation chelation agent [136]. Sonochemical synthesis method starts with a chemical reaction that is triggered by ultra-sonication of the precursors, and it is another effective synthesis method due to its simple and low-cost equipment, and simple process (Figure 12). Moghtada *et al* reported use of sonochemical methods for synthesis of titanate-based perovskite oxide nanocrystals [137].

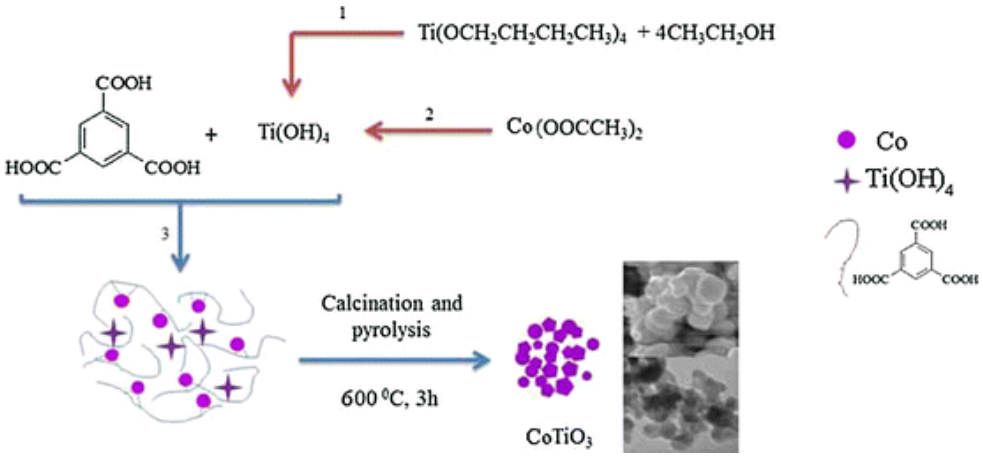

Figure 11:Process flow for synthesis of $CoTiO_3$ perovskite oxide nanoparticles. Adapted with permission from Springer (2015).

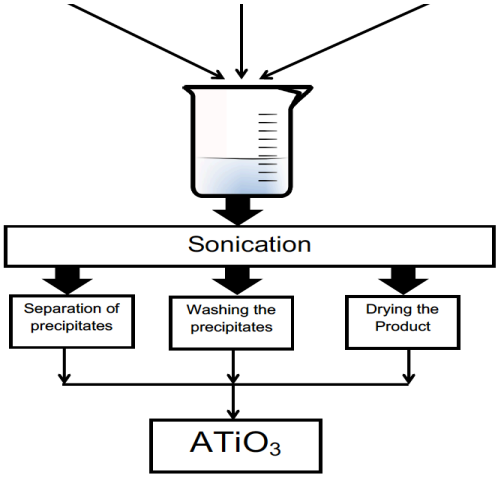

Figure 12: Process schematic for synthesis of $ATiO_3$ type perovskite oxide by sonochemical method .

2.3.2. Crystal structure, morphology and properties of perovskite oxides

Crystal structure

Perovskite materials are generally represented by the chemical formula ABX_3, where A and B are cations and X is an anion coordinating with B. Cations at site A are generally larger than the cation at site B. B-site cations are coordinated by the X site anion to form a BX_6 octahedron. A-site cation is located at the cavity of the 3-D frame made by the corner-shared octahedron [138]. Perovskite oxides (ABO_3) are a subclass of ABX_3 perovskites, where the A site cation is generally an alkaline earth or rare-earth ion, while site B contains a transition metal. In a typical ABO_3 structure, the A-site cation is 12-fold coordinated while the B-site cation is 6-fold coordinated with the oxygen anions. It must be noted that the ilmenite structure has the same composition as perovskite oxide. i.e., ABO_3. However, in an ilmenite structure the A-site and B-site cations are of almost identical size, unlike in perovskite oxides [96, 102, 139, 140]. The ideal perovskite structure is cubic as shown in Figure 13[141], however many compounds have a slightly distorted variants with lower symmetry [142].

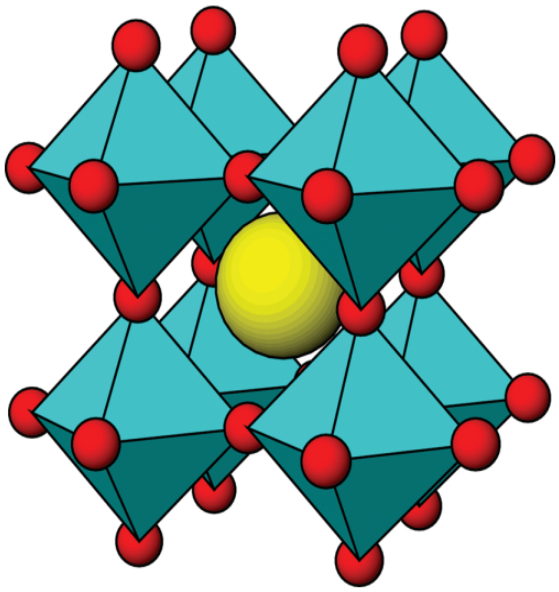

Figure 13: Crystal structures of an ideal cubic perovskite oxide. Here, the green sphere is the position of cation A. Cation B (not shown) is located inside the dark green octahedron with the 8 oxygen atoms (red spheres) in the 8 corners. permission from [141]; copyright American Chemical Society 2011.

Further studies indicated that oxygen or cation vacancies cause structure distortions producing variance in properties. Distortion in the ABO_3 structure can be mathematically represented by Equation (1), by comparison to an ideal cubic lattice:

$$\mathrm{D} = \frac{\mathrm{r}_A + \mathrm{r}_O}{\sqrt{2}}(r_B + r_O) \qquad (5.)$$

Normally, in perovskite oxide structures, the value of distortion, i.e. D in Equation (1), ranges from 0.80 to 1.10. A tilted octahedron creates other crystal phases namely, orthorhombic, rhombohedral, tetragonal, monoclinic, and triclinic, as shown in Figure 14[Grabowska, 2016 #105].

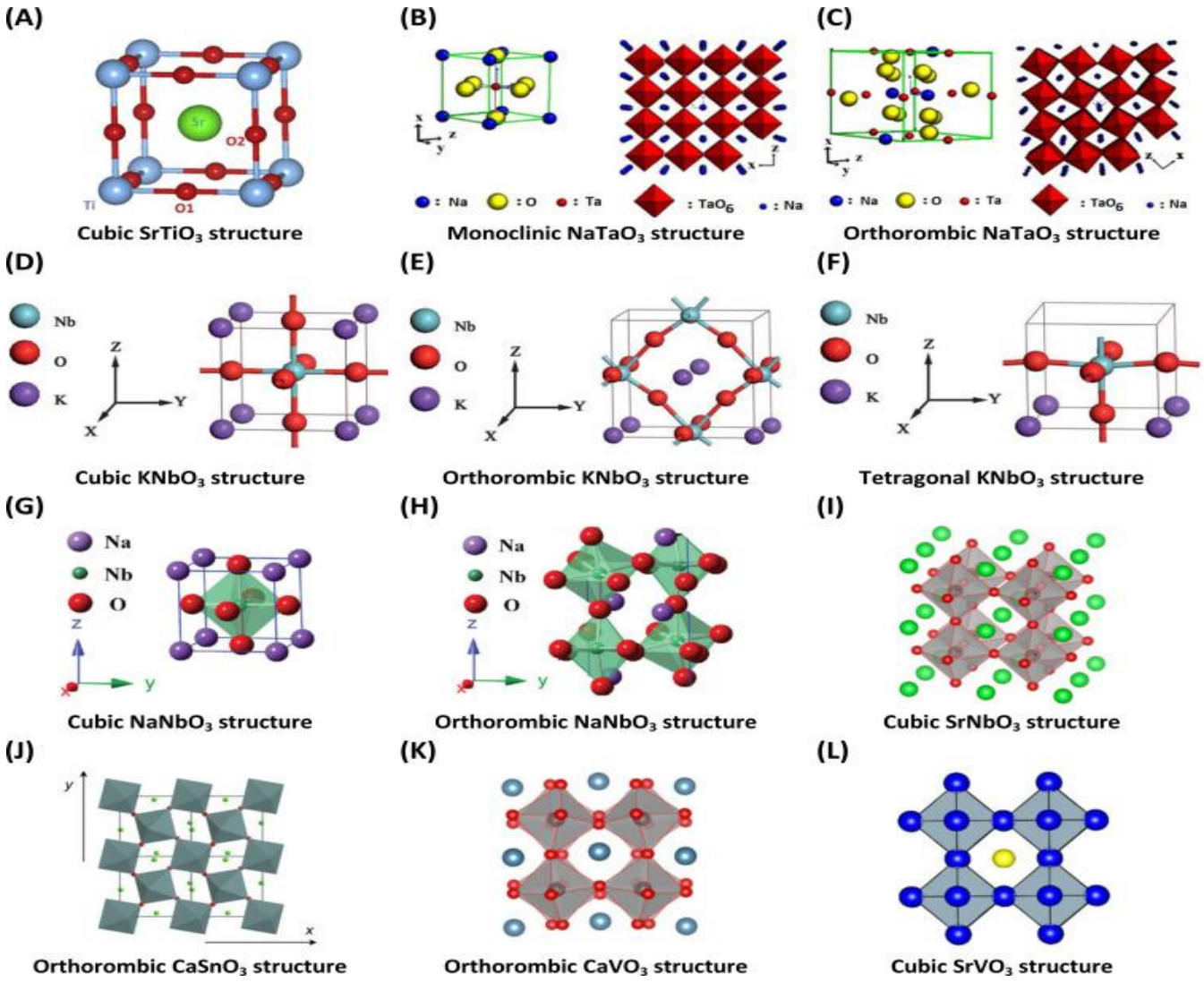

Figure 14: Distorted structures of selected perovskite oxides. Reprinted with permission from [106]; copyright American Chemical Society (2011).

Nanoscale morphology

Photogenerated charge carriers tend to go through radiative/nonradiative recombination before the initiation of a redox reaction. To reduce recombination and enhance photocatalytic efficiency it is important to choose a proper morphology of perovskite oxide nanomaterials. Nanoscale morphology of perovskite oxides is an important parameter that influences the efficiency of photocatalytic reactions. Perovskite oxide nanomaterials bearing nanoscale morphologies also tend to have fewer defects and therefore exhibit more resistance against charge carrier recombination. Nanoscale morphology in perovskite oxide nanomaterials also provides high surface area, which contributes to greater photocatalytic performance [143-148]. One of the widely researched nanoscale morphology of perovskite oxides is the nanoporous structure (Figure 15). Nanoporous $LaMnO_3$ exhibited enhanced performance in photocatalytic organic dye degradation, when compared to other photocatalysts [149]. However, the authors stated that better crystallinity along with higher surface area of their catalyst could further improve the photocatalytic performance of their catalyst. In yet another nanoporous scheme, Fu *et al* [150]

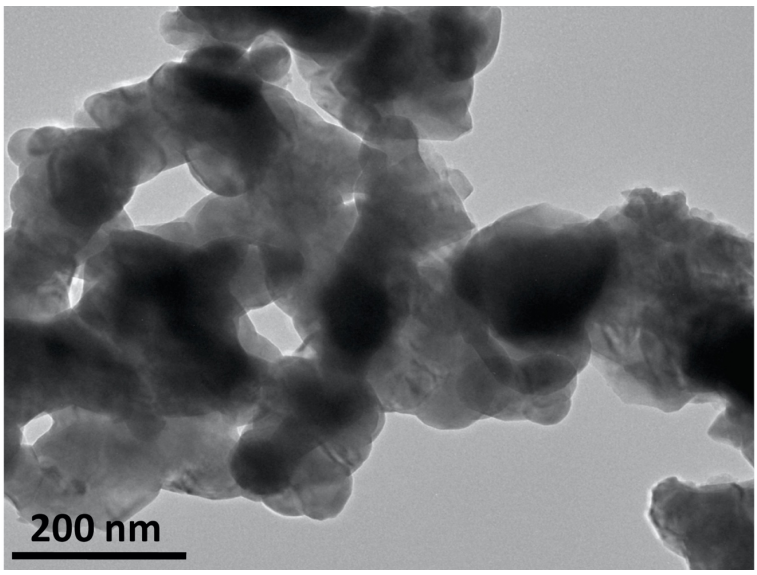

Figure 15: Bright field TEM image, showing the porous structure with 200 nm particle size of $LaMnO_3$, Reprinted with permission from [149]; copyright Elsevier (2017).

illustrated that hollow sphere $LaCoO_3$ achieved high photocatalytic activities attributed to large surface areas and more active sites. Microtubes/nanotubes constitute another common nanoscale morphology in perovskite oxides. Figure 16 shows a TEM image of individual $PbZrO_3$ nanotubes.

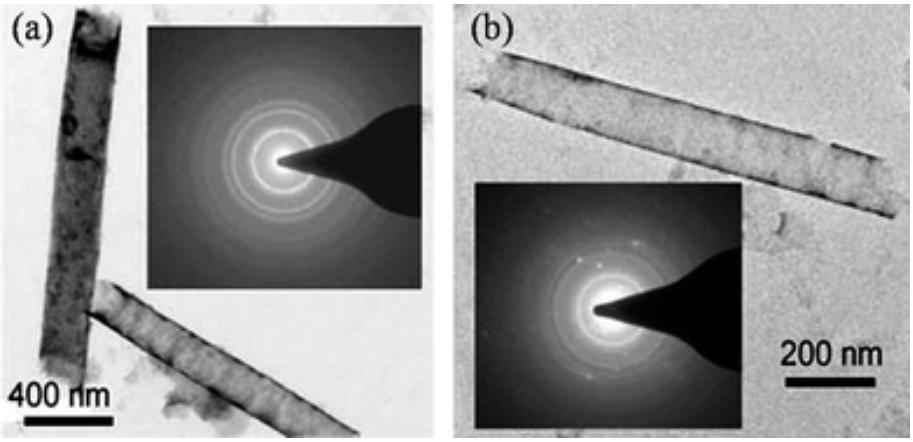

Figure 16: (a) and (b) are TEM images of individual $PbZrO_3$ nanotube imaged at two different scale. The insets show electron diffraction patterns indicating polycrystalline structures of PZO-NT. Reprinted with permission from Royal Society of Chemistry (2010).

Zhu *et al* [151] wrote a review paper on perovskite oxide nanotubes that we recommend readers for additional details. Perovskite oxides have also been engineered to possess nanofiber morphology, for which electrospinning is the most common synthesis method. Zhang et al [152] synthesized monoclinic $NaNbO_3$ nanofibers, which were uniformly distributed on Al substrates (shown in Figure 17).

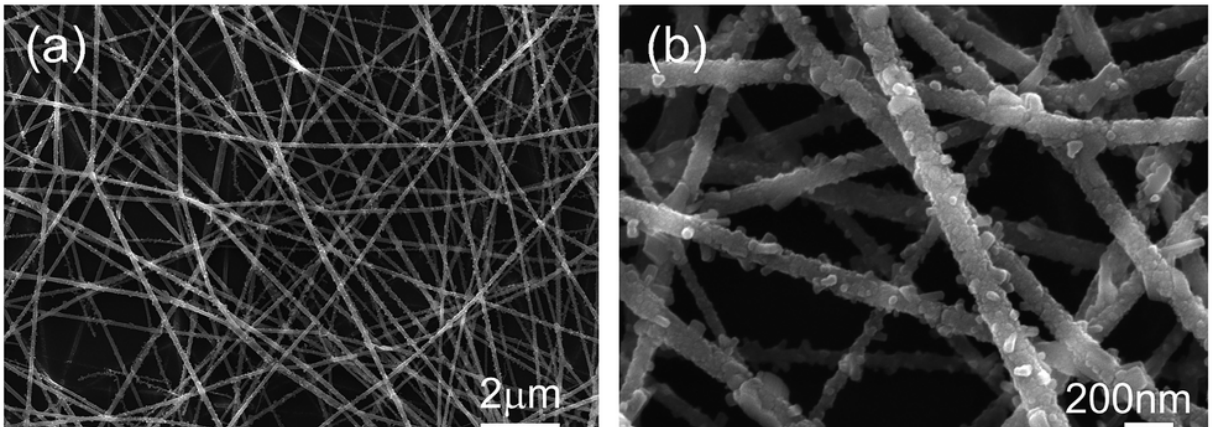

Figure 17: Dark field SEM images of ultra-long $NaNbO_3$ nanofibers that are 100 nm in diameter. Reprinted with permission from Royal Society of Chemistry (2015).

In Figure 18, it is also shown that plenty of nanoparticles are attached on the surface of nanofibers, which enhanced surface area and increased the population of reactive sites. Other nanoscale morphologies in perovskite oxides are reported, and one interesting type is the nanocube structure. Zhang et al [153] used hydrothermal synthesis to obtain porous $LaNiO_3$ nanocubes (Figure 18). Because of the large specific surface area (i.e. area per unit volume) of the $LaNiO_3$ nanocubes as well as its good activity as an electrocatalyst, it can be potentially used for photocatalytic CO_2 reduction.

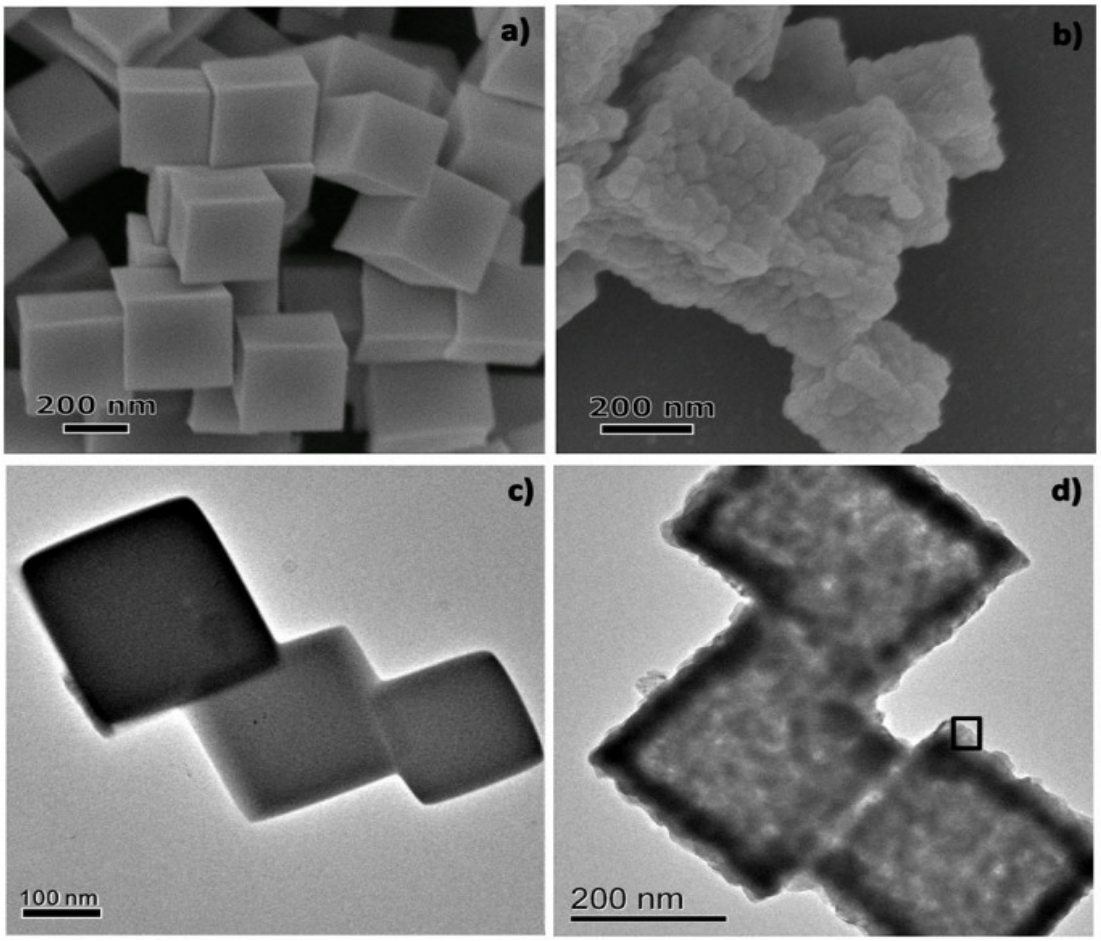

Figure 18: (a) SEM image, and (c) and TEM image, showing a 250 nm smooth surface nanocube shape-precursor; (b) SEM image, and (d) TEM image, indicating morphology after oxygen annealing. Reprinted with permission under the terms of a Creative Commons license.

2.3.3. Bandgap engineering

Density Functional Theory (DFT) modeling for band gap engineering

DFT has emerged as a viable method for bandgap engineering because it can be used to calculate electronic structure, which affects band-gap and light absorption characteristics of semiconductors. DFT models can also illuminate crystal structure effects on photocatalytic perovskites [154]. That is because the energetics of crystalline facets affects their photocatalytic performance. However, DFT modeling of oxide perovskites is a new area of research and not many references can be found on the topic. Typical methods for DFT modeling, as applied to perovskites, are surface relaxation and electronic localization.

Research efforts have been directed at applying DFT modelling to understand and engineer the band structure of perovskites with, and without, doping [155]. While experimental methods can be applied to study existing materials, DFT can be used to analyze and engineer photocatalytically important electronic properties (e.g. bandgap and position of Fermi level) of the material as a function of their composition and the presence of any dopants. This, in turn, can lead to synthesis of photocatalysts of optimized chemistry, which can lead to efficient and improved CO_2 photoreduction systems. Bandgap engineering with non-metallic materials entails modification of valence bands and/or adjustment of conduction bands. Proper bandgap engineered oxide perovskites, with non-metals involved addition of the non-metals that have energies higher than the *p*-orbital of oxygen.

Bandgap engineering with metallic materials resulting in narrow bandgaps involved transition metal impurities with d10 orbitals (such as Cu and Ag) and those with partially filled dn orbitals

(such as V, Ni, Cr, Fe, etc.). Takei *et al* [154] reported DFT models of the AB2O6 types of perovskites by varying the A, where they studied $LiBiO_3$, $NaBiO_3$, $MgBi_2O_6$, $KBiO_3$, $ZnBi_2O_6$, $SrBi_2O_6$, $AgBiO_3$, $BaBi_2O_6$ and $PbBi_2O_6$. They calculated the bandgap values to be 1.63, 2.53, 2.04,1.61, 1.93, 1.93, 1.53, 0.87 and 1.92 eV for $LiBiO_3$, $NaBiO_3$, $KBiO_3$, $MgBi_2O_6$, $SrBi_2O_6$, $BaBi_2O_6$, $ZnBi_2O_6$, $AgBiO_3$, and $PbBi_2O_6$, respectively. Such estimates of bandgaps values are useful in selection of perovskites for visible light driven CO_2 photoreduction.

Perovskite oxides can be doped with metals and non-metals, and it is of interest to the field of photocatalysis to understand how metallic (or cationic) dopants and non-metallic (or anionic dopants affect band structure. Chen *et al* [156] performed DFT modelling of metal doped as well as pristine $SrTiO_3$. The found that in pristine $SrTiO_3$, the valence band is predominantly comprised of O 2*p*−Ti 3*d* hybridized orbitals, whereas Ti 3*d* orbitals dominate the conduction band and Sr *3d* orbitals do not participate in the electronic band structure. From their DFT model of metal doped $SrTiO_3$, they concluded that the Fermi level was positioned within dopant states and therefore the dopant intrinsically had empty states to accept active electrons. They used their findings to further state that dopants do not interfere with the conduction band and that only the available electrons drive the photoreduction process. Generally, the outermost orbital energies of dopants must lie between the conduction band and valence band of host material. Non-metals such C, N, S and P have been shown to assume energies higher than the O 2*p* orbital at the valence band of $NaTaO_3$ and less than the energy of Ta 5*d*. Wang *et al* [157] performed DFT modeling of $NaTaO_3$ with these anionic dopants in mono-dopant and co-dopant forms. They found that the band gap significantly reduced due to anionic element doping because *p*-orbitals of the elements are higher than O 2*p* orbitals. On the basis of their DFT model as shown in the density of states (DOS) plots

in Figure 19, they particularly demonstrate that N-N, C-S, and P-P co-doping renders the perovskite suitable for absorbing visible light.

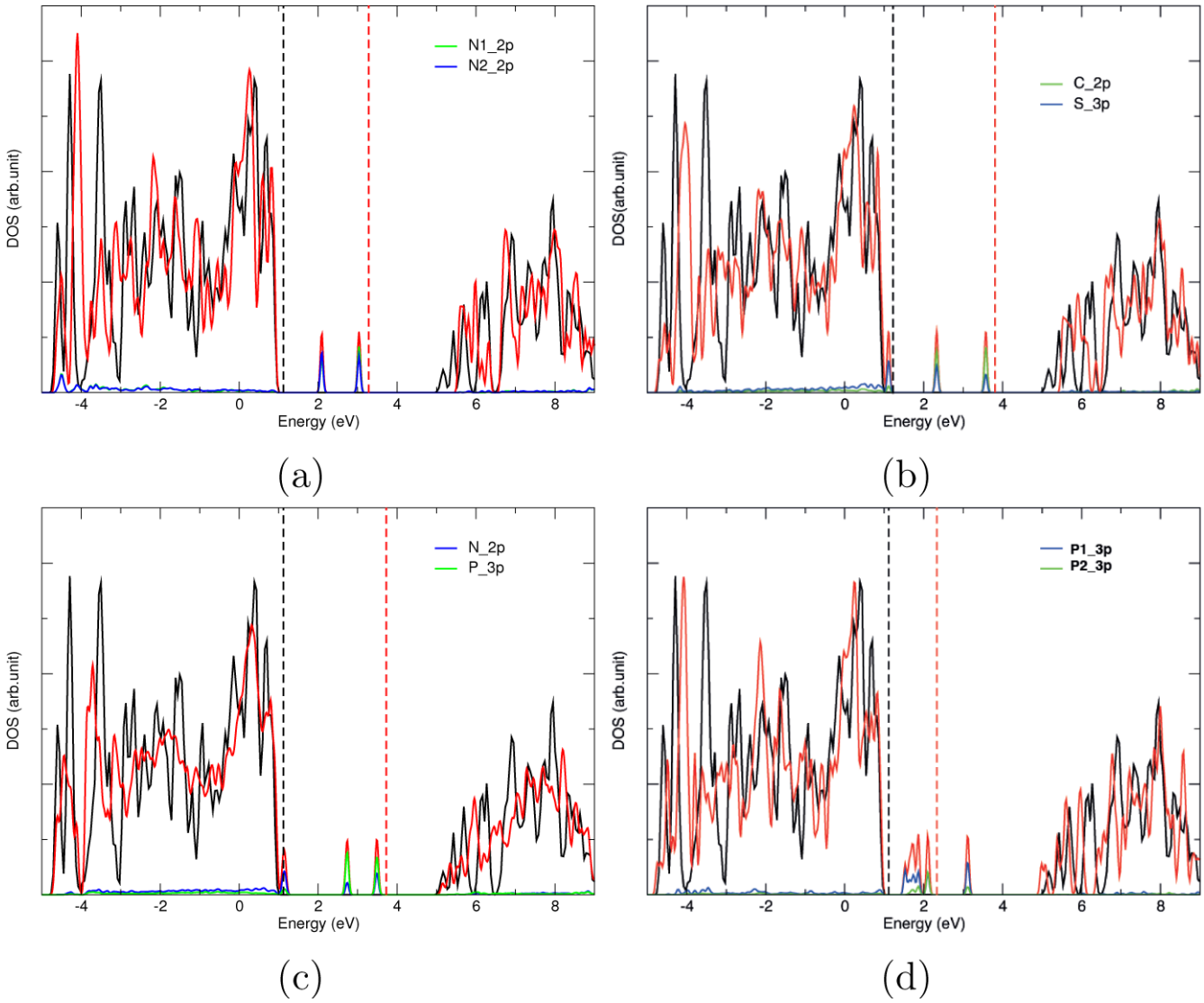

Figure 19: DOS plot of N-N, C-S, N-P and P-P co-doping of $NaTaO_3$. Reprinted with permission under the terms of a Creative Commons license.

There are approaches to reduce the bandgap in oxide perovskites without introducing metals (cationic) or non-metal (anionic) doping, whereby metal oxide double peroxide structures ($A_2B'BO_6$) are employed. One example of such a type of structure is barium bismuth niobate

(Ba_2BiNiO_6) reported by Weng *et al* [158], who via DFT models, showed that Bi rich, and Nb poor stoichiometries can reduce the bandgap.

Methods for bandgap engineering

Doping and substitution are two conventional methods of obtaining a desirable bandgap. Both metals and non-metals can serve as dopants, including elements such as Cr, Ni, Mn, Pb, Bi, N, Br, S, C, F, Cu, Au, Ag, Pt, Pd, Ph, Ru, Rh, etc. Because doping can introduce a midgap state below the conduction band, visible light can be absorbed. An appropriate dopant can narrow the bandgap and lower the probability of recombination of electrons and holes. However, an impropriate dopant can induce defects and thus increase recombination. One popular method for decreasing the bandgap without inducing defects calls for the use of co-dopants to balance the charge. Examples of co-dopants are Ta and Ni [159], and Sb and Cr [160]. Co-dopants restrain the formation of higher valence ions and oxygen defects, thus minimizing non-radiative recombination. The introduction of doping ions, which have higher valence than the parent cations in perovskite oxides, has been considered for suppressing photocatalytic activity.

Besides doping, ion substitution is also a fundamental method for obtaining a desired band gap. For ABO_3 perovskite oxides, either the A or B site cations, or even both, can be changed to narrow the band gap. In wide bandgap titanate perovskite oxides, due to the large deviation of the electronegativity of Ti and O, the bandgap can be narrowed by substituting or partially substituting the titanium cation with more electronegative elements such as Ni or Co. An optimized material $CeCo_{0.05}Ti_{0.95}O_{3.97}$ with a band gap of 1.57 eV (corresponding to an optical absorption edge of 785nm) was reported to have successfully degraded 91 % of an aqueous Nile Blue solution in 3 hours [161].

Recently, multi-component perovskite oxides have become more attractive, wherein different materials are mixed to combine their advantages and abilities. One example of a multi-component perovskite oxide is $SrTiO_3$-$AgNbO_3$ [162]. In some special cases, researchers use one ABO_3 perovskite oxide and one ABX_3 perovskite oxynitride to modulate the band gap, while avoiding doping induced defects and the degradation of carrier transport properties [163].

2.4. Performance

The photocatalytic performance of different perovskite oxides is summarized in Table 3.

Table 3: Performance of different perovskite oxides in artificial photosynthesis.

Catalyst	Light Source, Conditions	Reported Products	Comments	Ref
$SrTiO_3$	Near UV, 15 torr CO_2, 17 torr H_2O introduced into the ultrahigh vacuum chamber containing Pt|$SrTiO_3$|Pt at temperature of 315 K	CH_4	$SrTiO_3$ (111) crystal face CH_4 production, reaction decreased after 10 min because of poisoning (Cl at on $SrTiO_3$ surface from unknown source and a monolayer of carbon on Pt).	[164]
$SrTiO_{3-\delta}$	Visible, Pt-$SrTiO_{3-\delta}$	CH_4 (0.25 μmol m^{-2} h^{-1})	Cell parameter increases with oxygen deficiency, photoactivity considerably decreases after 10 hrs. Annealing at 1200 °C in argon is needed to regenerate photocatalytic activity.	[113]
$SrTiO_3$	UV-vis, Au loaded (precipitation method) $SrTiO_3$	CO (349 nmol h^{-1} g^{-1}) CH_4 (231 nmol h^{-1} g^{-1})	Used leaf as an architecture-design agent to construct 3D helical architecture to enhance rate of CO_2 reduction. Poisoning of Au after 80 hrs.	[114]
$NaNbO_3$	Visible, Pt−$NaNbO_3$ 1.5 hr of irradiation	CH_4 (653 ppm $h^{-1}g^{-1}$)	Orthorhombic crystal, photocatalytic activity of $NaNbO_3$ nanowires was	[165]

			found to be better than $NaNbO_3$ nanoparticles. Poor photocatalytic repeatability.	
$NaNbO_3$	Visible, Pt loaded $NaNbO_3$, 8 hr of irradiation	CH_4 (0.486 μmol h^{-1})	Photocatalytic activity of cubic $NaNbO_3$ was found to be better than that of orthorhombic $NaNbO_3$.	[154]
g-C_3N_4 /$NaNbO_3$	Visible, Pt-g-C_3N_4/$NaNbO_3$	CH_4 (6.4 μmol h^{-1} g^{-1})	Photocatalytic activity of g-C_3N_4/$NaNbO_3$ heterojunction for CO_2 reduction was almost 8 times higher than that of individual C_3N_4.	[166]
g-C_3N_4 /$KNbO_3$	Visible, Pt-g-C_3N_4/$KNbO_3$	CH_4 (1.94 μmol h^{-1} g^{-1})	Pt-$KNbO_3$ has poor photocatalytic activity, however g-C_3N_4/$KNbO_3$ has photocatalytic activity 4 times higher compared to that of naked g-C_3N_4.	[167]
$NaNbO_3$ and $KNbO_3$	UV, Pt loaded $KNbO_3$ and $NaNbO_3$	7 ppm/hr ($KNbO_3$), 2.3 ppm/hr ($NaNbO_3$)	$KNbO_3$ absorbs more light compared to $NaNBO_3$ because of its low bandgap. $KNbO_3$ has high BET surface area compared to $NaNbO_3$.	[168]
$NaTaO_3$	Visible, 1 wt% Au loaded $NaTaO_3$	CO (173 nmol h^{-1} g^{-1}), CH_4 (36 nmol h^{-1} g^{-1})	Activated white pine wood as the template for catalyst microstructures to increase the surface area. Co-catalyst Au was deposited by precipitation method. Photocatalytic activity of templated catalyst by activated wood > template by non-activated wood > non-templated wood.	[169]
$NaNbO_3$ and $NaTaO_3$	UV (365nm), 2 bar, 50°C, 15 hr of irradiation	CO, CH_4, H_2, CH_3OH	No metallic co-catalyst was used. Products from $NaNbO_3$ and $NaTaO_3$ was comparable to TiO_2. $NaNbO_3$ and $NaTaO_3$ evolve similar amount of CO	[170]

			and CH_3OH while $NaTaO_3$ produces more CH_4 and low H_2.	
$LiNbO_3$	Visible, Ti and LiNbO3 as catalyst	HCOOH and HCHO; 1.31×10^{-2} $mol \cdot m^2 \cdot h^{-1}$ 9.56×10^{-4} $mol \cdot m^2 \cdot h^{-1}$ under visible irradiation	$LiNbO_3$ produces 7 times more product under UV and 36-times more product under visible light compared to anatase TiO_2.	[171]
Basalt Fiber $PbTiO_3$ core shell	365 nm, Basalt Fiber (BF) decorated with $PbTiO_3$ nanoparticles prepared by sol-gel	CH_4 (290 $\mu mol\ g^{-1}\ L^{-1}$ in 6 hrs)	Compared to BF-TiO_2, BF-$PbTiO_3$ has higher adsorption capabilities for CO_2 and H_2O, high mobility and charge separation capabilities.	[172]
C-$LaCoO_3$	Visible ($\lambda > 400$ nm), C-doped $LaCoO_3$ prepared by pyrolysis of R08 biomass	HCHO, HCOOH (95 $\mu mol\ h^{-1}\ g^{-1}$)	C-doping doesn't change crystal structure of perovskite, but enhances optical absorption by tuning bandgap.	[118]
C and Fe co-doped $LaCoO_3$	Visible ($\lambda > 400$ nm), C–$LaCo_{0.95}Fe_{0.05}O_3$	HCHO, HCOOH (128 $\mu mol\ h^{-1}\ g^{-1}$)	Addition of Fe forms dopant energy level above the valance band of $LaCoO_3$ and electron in interbond is excited to the conduction band upon absorption of visible light.	[173]
$ALa_4Ti_4O_{15}$ (A = Ca, Sr, and Ba)	UV-Vis, 2 wt % Ag loaded $BaLa_4Ti_4O_{15}$, bubbled	H_2 (10 $\mu mol\ h^{-1}$), O_2 (16 $\mu mol\ h^{-1}$), CO (22 $\mu mol\ h^{-1}$) HCOOH (0.7 $\mu mol\ h^{-1}$)	$BaLa_4Ti_4O_{15}$ has better catalytic property compared to $CaLa_4Ti_4O_{15}$ and $SrLa_4Ti_4O_{15}$.	[174]
Bi_2WO_6	420 nm < λ < 620 nm, Annealed/not annealed catalyst. CO_2 bubbled/not bubbled through water, ball-flower structured catalyst	CO (2.5 $\mu mol\ g^{-1}$ in 5 hr)	When CO_2 was bubbled, un-annealed Bi_2WO_6 performed better. But when CO_2 was directly exposed, annealed sample performed well. Exposing CO_2 directly was proposed to be more efficient.	[175]

Bi_2WO_6	Visible, Single-unit cell thickness of Bi_2WO_6	Methanol (75 μmol h^{-1} g^{-1})	Single unit cell has 3 times higher CO_2 adsorption, higher photoabsorption, higher conductivity, longer carrier lifetime. Single unit cell operates even after 2 days without deactivation.	[176]
Bi_2WO_6	Visible (λ > 400 nm), NIR (λ > 700 nm), Ultrathin Bi_2WO_6 nanosheet decorated with carbon quantum dots (CQD)	CH_4 (7.19 μmol g^{-1} in 8 hours)	1 wt % CQD gives best performance. Increasing CQD concentration reduces light exposure to Bi_2WO_6 and increases recombination of photoexcited charge carriers.	[177]
Bi_2WO_6	Visible (λ > 420 nm) about 9.5 nm of Bi_2WO_6 nanoplates, no co-catalyst	CH_4 (1.1 μmol h^{-1} g^{-1})	Solid state reaction synthesized Bi_2WO_6 showed very poor photocatalytic property (0.045 μmol h^{-1}g-1). Hydrothermally prepared Bi_2WO_6 showed larger surface area and high charge carrier mobility resulting in better photocatalytic property.	[178]
$MnCo_2O_4$	Visible, Microsphere $MnCo_2O_4$ (4 μmol), [Ru(bpy)3] $Cl_2 \cdot 6H_2O$ (10 μmol, hereafter abbreviated as Ru), solvent (5 mL, 2:3 H_2O/acetonitrile), and TEOA (1 mL) in an 80-mL reactor	CO, H_2	27 μmol CO and 8 μmol H_2 were generated within an operation time of 1 h.	[179]
$ZnGa_2O_4$	UV-Vis, nanosheet and meso $ZnGa_2O_4$, no cocatalyst	CH_4	Nanosheet $ZnGa_2O_4$ resulted in approximate 6.9 ppm/h CH_4 formation rate for 12 hours operation.	[180]
$CaTaO_2N$	Visible, as a building block for Z-scheme with the aid of a binuclear Ru complex	HCOOH with high selectivity (> 99 %)	320 nmol HCOOH under condition of 4.0 mg $CaTaO_2N$;4:1 v/v of DMA/TEOA 4 mL; Reaction time: 15 h.	[119]

2.4.1. Titanate group

Hemminger *et al* [164] reported a single crystal of $SrTiO_3$ having (111) orientation at 1000 K, and sandwiched between Pt foils by spot welding for improved CO_2 reduction. Their samples were illuminated with near UV irradiation by the use of $NiSO_4$ filtered radiation from a mercury lamp. Pressurized CO_2 and H_2O was introduced into the ultra-high vacuum chamber and enhanced production of CH_4 was detected. After 10 minutes, the rate of production of CH_4 decreased because of the formation of a Cl layer (from unknown source) on $SrTiO_3$ crystal face and a monolayer of carbon on Pt. CH_4 production was found to be regenerated by cleaning the sample. Zhou *et al* [114] used natural leaves to make 3D helical structure of $ATiO_3$ (A=Sr, Ca and Pb) to improve the photocatalytic activity compared to the powdered constituents. The high connectivity of hierarchical pores and branching network of aeration within leaves were demonstrated to promote gas diffusion and improve photocatalytic activity. The authors claimed that the 3D hierarchical architecture of their perovskite oxide enhanced light harvesting by capturing light and transferring it further into the structure. Higher surface area provided more reaction sites, thus enhancing overall performance. The photocatalyst maintained its photocatalytic activity for up to 80 hours, after which long irradiation, absorption of intermediates, and reduction products poisoned the catalyst. Pure $SrTiO_3$ is not considered as a good catalyst because it is only active under UV irradiation, and therefore dopants such as Fe, C, N, and Cr are often introduced to make it responsive to visible light. Xie *et al* [113] introduced a self-doping mechanism for $SrTiO_3$ by using a one-step combustion method and high temperature annealing. Oxygen vacancy and Ti^{3+} tunes the bandgap and enhanced the visible light absorption of the resulting $SrTiO_3$ perovskite oxides, while enhancing the chemical absorption of CO_2, thus improving photoreduction capabilities (Figure 20).

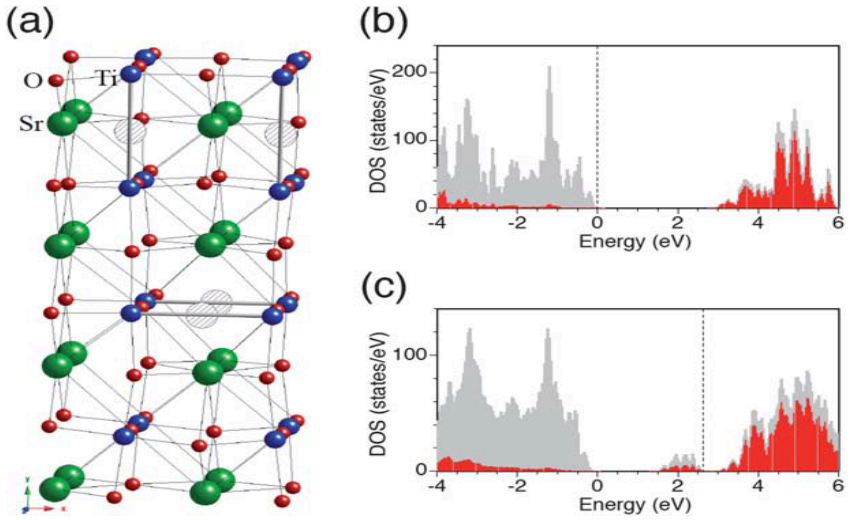

Figure 21: (a) Atomic arrangement in the $SrTiO_3$ structure, where green, blue and red particles represent Sr, Ti, and O atoms; striped circles denote oxygen vacancies, and solid bars denote Ti-Ti bonds in the structure (b) and (c) give the local density of state of pristine $SrTiO_3$ as well as the same for $SrTiO_3$ with defects. Reprinted with permission from Royal Society of Chemistry (2011).

Do *et al* [172] demonstrated that a well decorated $PbTiO_3$ was able to achieve higher light absorption, charge separation, and CO_2 and H_2 adsorption ability in comparison to basalt fiber/TiO_2 core shell and bare basalt. Likewise, Im *et al* [181] obtained $CaTiO_3$ and TiO_2 on basalt fiber using a two-step method (SEM images are shown in Figure 21), and this catalyst achieved high photocatalytic activity during CO_2 reduction ($CH_4 \approx 17.8$ µmol/g, CO ≈ 73.1

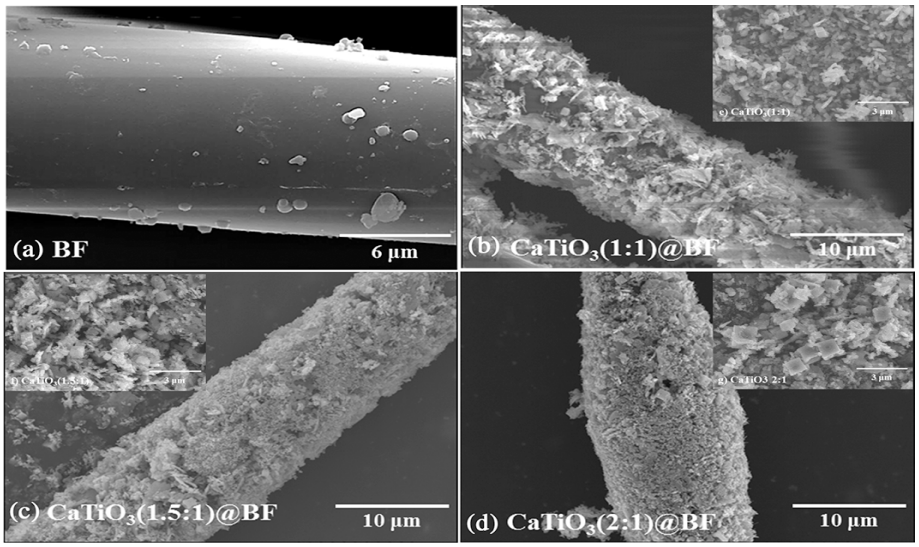

Figure 20: (a) SEM image of basalt fiber; (b), (c) and d) are SEM images of basalt fiber decorated with $CaTiO_3$ with different ratio of Ca:Ti (ratio increasing from (b) to (d)), illustrating that a higher ratio of Ca had denser particle clusters on the surface of basalt fibers. Reprinted with permission from John Wiley and Sons (2017).

μmol/g). The high performance is attributed to appropriate pore size and oxygen vacancies. SEM images were used to compare morphologies between various Ca:Ti ratios.

2.4.2. Niobate group

$NaNbO_3$ has an orthorhombic crystal structure (o-$NaNbO_3$) at room temperature and has an unusual complex sequence of temperature and pressure driven structural phase transitions [182, 183]. Li *et al* [154] compared the photocatalytic activity of Pt loaded $NaNbO_3$ with orthorhombic and cubic structure (c-$NaNbO_3$) and found that the cubic structure exhibits better photocatalytic properties because of higher symmetry. The higher symmetry results in a unique electronic structure that is beneficial for electron excitation and transfer. c-$NaNbO_3$ has conduction bands, which are more dispersive than those of o-$NaNbO_3$. Besides, the lower bandgap indicates that the photogenerated electrons in c-$NaNbO_3$ possess a smaller effective mass, and that favors electron transfer and higher photocatalytic ability of c-$NaNbO_3$. The observed CH_4 evolution rates were 0.486 $\mu mol \cdot h^{-1}$ and 0.245 $\mu mol \cdot h^{-1}$ with c-$NaNbO_3$ and o-$NaNbO_3$ samples, respectively (with 0.5 wt % Pt). The best photocatalytic CH_4 evolution rate was obtained with a Pt loading of 1.0 wt %. Pt decorated, hydrothermally grown $NaNbO_3$ nanorods have been proven to have better CH_4 evolution rates compared to $NaNbO_3$ nanoparticles because of better crystallinity, larger active surface to volume ratio and anisotropic aspects [183]. Incorporation of $NaNbO_3$ nanowires with graphitic carbon nitride (g-C_3N_4) decorated with Pt showed better photocatalytic activity compared to bare $NaNbO_3$ or g-C_3N_4 alone due to well-aligned overlapping band structure of C_3N_4 and $NaNbO_3$. The valence band top of $NaNbO_3$ is lower than that of g-C_3N_4, but the conduction band bottom of g-C_3N_4 is higher than that of $NaNbO_3$. g-C_3N_4 thus acts as a sensitizer to absorb photons and creates photogenerated electrons and holes. The photoexcited electrons in g-C_3N_4 are injected

into the conduction band of $NaNbO_3$ and are subsequently transferred to Pt to generate CH_4 before the occurrence of recombination [166]. $KNbO_3$ has a lower bandgap and a higher mobility of charge carriers when compared to $NaNbO_3$, meaning $KNbO_3$ has higher light absorption and better charge transport properties, and therefore better photocatalytic properties [168]. Composites of g-C_3N_4 with $KNbO_3$ provide better photocatalytic properties compared to bare C_3N_4 and $KNbO_3$. The valence band top of $KNbO_3$ is lower than that of g-C_3N_4, while the conduction-band bottom of C_3N_4 is higher than $KNbO_3$. The photons and electrons absorbed by g-C_3N_4 are promoted to the conduction band and subsequently transferred to the conduction band of $KNbO_3$, whereupon they reduce CO_2 into CH_4 [80]. In the case of $LiNbO_3$, it has a higher bandgap compared to anatase TiO_2, yet the photocatalytic properties of $LiNbO_3$ are better than TiO_2. $LiNbO_3$ has a strong remnant polarization, which facilitates improved charge carrier lifetime as well as lower energy injection of charge carriers, improving the photocatalytic efficiency [184].

Photoluminescence spectra have been studied to obtain information about recombination processes. In Figure 22 [170], there is a broad emission band extending from 400 to 600 nm, which is typically

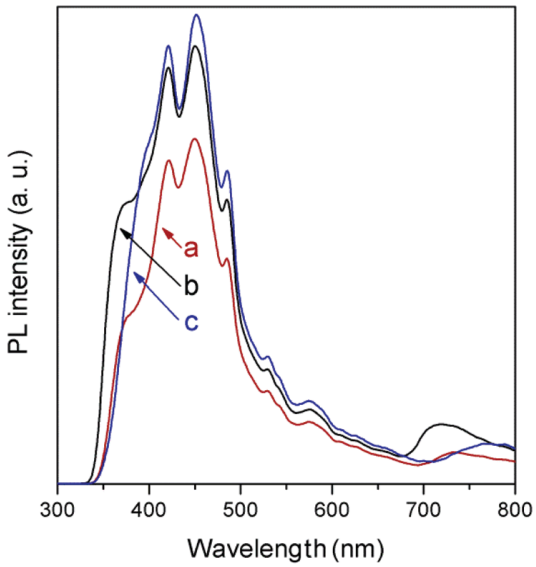

Figure 22: Photoluminescence measurements of (a) $NaNbO_3$, (b) $NaTaO_3$, and (c) TiO_2. Reprinted with permission from the Royal Society of Chemistry (2017).

observed in other ABO_3 perovskite oxides as well. It is also observed that $NaNbO_3$ shows lower intensity in this region than $NaTaO_3$ and TiO_2, which implies that direct- and defect-mediated recombination processes are weaker in $NaNbO_3$.

2.4.3. Tantalate group

Compared to $NaNbO_3$, electrons in the conduction band of $NaTaO_3$ have higher energy, which is a large driving force in the reduction reaction resulting in higher carbon evolution [170], because the photoactivity of catalysts depend upon their conduction band edges. Based on the conduction band energy levels, Zhou *et al* [169] reported that $LiTaO_3$ has superior photocatalytic performance followed by $NaTaO_3$ and $KTaO_3$ respectively (estimated edges of the conduction band of $LiTaO_3$, $NaTaO_3$, $KTaO_3$ are −1.302 V, −1.007 V and −0.98 V (vs. NHE), respectively). Ru/$NaTaO_3$ yielded 51.8 mmol/h/g of CH_4, which indicated highly efficient and stable photocatalytic activity. When Ru was introduced as a co-catalyst, hydrogen was suppressed by Ru, and that allowed the CO_2 reduction reaction to continue without running out of hydrogen [185]. To enhance light absorption and charge separation, Hou *et al* [186] reported that nitrogen and oxygen vacancies regulate the electronic structure in NaTaON, tuning the absorption band from 315 nm to the visible regime. Moreover, a cobalt (II) tetraphenyl porphyrin (CoTPP) sensitized $Na_{(1-x)}La_xTaO_{(3+x)}$ proved to be capable of reducing CO_2 with water, yielding methanol and ethanol as major products, along with trace amounts of CH_4, C_2H_8, C_2H_4. CoTPP sensitizer in $Na_{(1-x)}La_xTaO_{(3+x)}$ not only enables the absorption of UV and visible radiation, but also suppresses charge carrier recombination, leading to better performance in photocatalytic activity [187]. Teramura *et al* [188] indicated that $LiTaO_3$ has the highest photocatalytic activity among the $ATaO_3$ (A=Li, Na, or K) perovskite oxides in the order $LiTaO_3$ > $NaTaO_3$ > $KTaO_3$. The highest photocatalytic activity of

$LiTaO_3$ is because of its lowest band gap among the three. In Figure 23, the morphology of these three different types of tantalate based perovskite oxides is shown. They all have an average particle size ranging from 1 to 3 micrometers.

2.4.4. Cobaltate group

Jia *et al* [118] reported $LaCoO_3$ prepared by the sol gel method, while C-doped $LaCoO_3$ was synthesized by the microorganism chelate method using Bacillus licheniformis R08 biomass. Carbon doping favored the formation of Co-C bonds and reduced the bandgap, making the catalysts active in visible light. The perovskite oxide was also expected to have a higher charge carrier lifetime. Further doping of C-$LaCoO_3$ with Fe enhanced the photocatalytic property, since Fe forms a dopant energy level above the valance band of $LaCoO_3$ and electrons in the interband states are excited to the conduction band upon absorption of visible light. Osazuwa *et al* [189] reported a conversion of over 90 % of CO_2 to CH_4 using $SmCoO_3$, which also exhibited H_2 and CO yields of over 60 %.

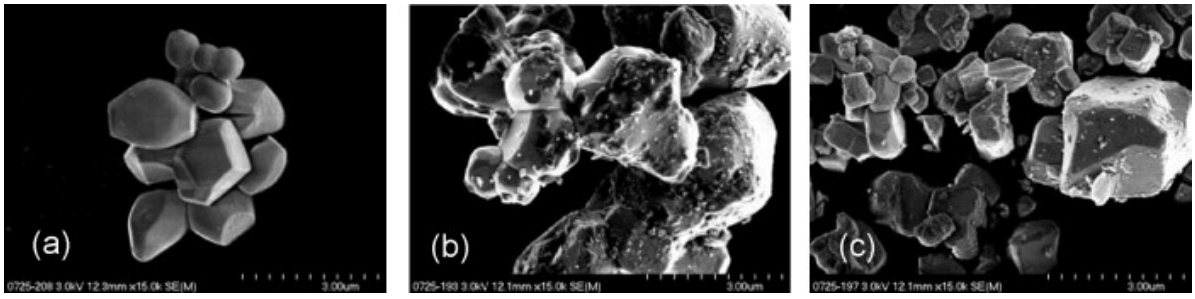

Figure 23: SEM image of the morphology of tantalate-based perovskite oxides (a) $LiTaO_3$, (b)$NaTaO_3$, (c) $KTaO_3$. Reprinted with permission from [118]; copyright Elsevier (2010).

2.4.5. Double perovskite type oxides

Bi_2WO_6 is the simplest member of the Aurivillius family, and it has a WO_6 octahedron sandwiched between two layers of $(Bi_2O_2)^{2+}$, and possesses a bandgap of 2.75 eV [190, 191]. Zhou *et al* compared the photocatalytic performance of Bi_2WO_6 prepared with hydrothermal and solid-state

reactions. Compared to the solid state reaction of Bi_2WO_6, hydrothermally prepared nanoplates were found to have higher charge mobility and larger surface area, due to which they exhibited better photocatalytic properties [178].

Sun *et al* [175] used nanoplates composed of ball-flower like Bi_2WO_6 (Figure 24) synthesized with an inorganic hydrothermal method to produce CO as main product along with a small amount of acetaldehyde. Annealed Bi_2WO_6 showed better CO production when there was a small amount of water vapor because of enhanced crystallinity, reduced recombination of photoexcited electron hole pairs, and improved CO_2 absorption. Reducing the thickness Bi_2WO_6 improves photocatalytic properties. Kong *et al* [177] compared the photoreduction capability of ultra-thin nanosheet of Bi_2WO_6 (length 100-200 nm, thickness ~ 5 nm) with nanopellets. The ultrathin nanosheet was found to have better photocatalytic properties compared to the nanopellets. To further enhance CO_2 reduction efficiency, carbon quantum dots were used, which enabled absorption of near infrared photons and hence enhanced the CO_2 photoreduction efficiency. Compared to the bulk Bi_2WO_6, the single-unit-cell thickness of the double perovskite sheets provides better photoabsorption and a larger active surface area, therefore enabling higher CO_2 adsorption capability, higher electronic conductivity and longer photoexcited carrier lifetime (and lower recombination). This property enables single-unit cells of Bi_2WO_6 to perform as better photocatalysts compared to its bulk form [176]. Furthermore, Wang et al presented an efficient Bi_2WO_6 nanoplate catalysts for generation of methane via CO_2 reduction in presence of water vaper [192]. They decorated their Bi_2WO_6 nanoplate catalyst with Au and CdS nanoparticles.

Rapid CO_2 photoreduction occurred in their catalysts via electron transfer from conduction band of Bi_2WO_6 to valence band of CdS through Au nanoparticle.

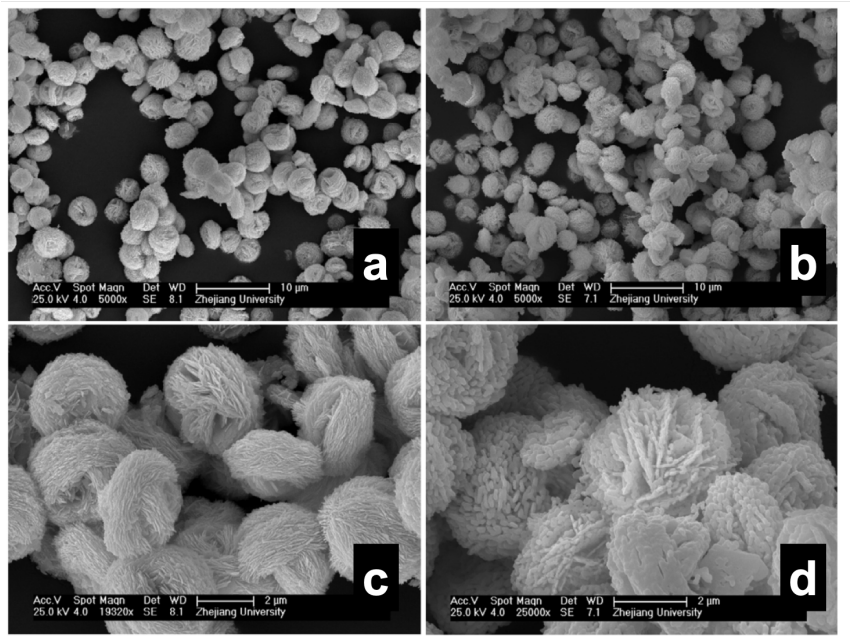

Figure 24: (a) and (c) are SEM images of as-synthesized Bi_2WO_6 nanoflower structures, and (b) and (d) are SEM images of Bi_2WO_6 nanoflower structures that were annealed at 550 °C. Reprinted with permission from Ref American Physical Society (2007)

Under UV- irradiation, $Ag/ALa_4Ti_4O_{15}$ (A = Ca, Sr and Ba) photocatalysts were shown to reduce CO_2 to CO and HCOOH upon bubbling CO_2 gas into an aqueous suspension of the photocatalyst powder. Among these perovskites, $BaLa_4TiO_{15}$ with an anisotropic structure, showed higher photocatalytic activity than $SrLa_4TiO_{15}$ and $CaLa_4TiO_{15}$. Under specific loading of an Ag co-catalyst on the edge of $BaLa_4Ti4O_{15}$, the main reduction product from $Ag/BaLa_4Ti_4O_{15}$ suspension was CO rather than H_2. The edge and the basal planes of $BaLa_4Ti_4O_{15}$ were proposed to be the reduction and water oxidation sites, respectively. Loading fine Ag particles (10–20 nm) onto $BaLa_4Ti_4O_{15}$ by impregnation and H_2 reduction or a liquid phase reduction method, CO_2 reduction to CO and HCOOH dominated over water reduction to form H_2 [174].

2.5. Commercialization of CO_2 reduction process

Commercialization of perovskite oxides based CO_2 reduction systems is dependent upon their photocatalytic CO_2 reduction performance, easy availability, wide applicability, controllable physicochemical properties and stability under exposure to various chemical and temperature conditions [132]. Photocatalytic performance may be defined in terms of solar to fuel conversion efficiency (SFE), which is the ratio of rate of fuel evolution times the energy requirement for formation of the fuel to the energy of incident solar light. SFE has to be at least 10% for viable commercialization of the perovskite oxide catalysts [193]. Considering high product/fuel yields using peroxide oxide based catalysts (as listed in Table 3), the perovskite oxide materials may be suitable for commercialization in terms requisite SFE. However, to-date only a few publications report SFE values, which therefore is a subject for further research. In addition, adequate thermal stability of perovskite oxides renders them applicable in gas phase photocatalytic CO_2 reduction reactions in a wide range of temperature conditions. The commercial usability of perovskite oxides catalysts can be visualized, however, only in small scale and localized applications, and not in open air because atmospheric CO_2 concentration is very small (i.e. 400 ppm) to undergo photocatalytic conversion. Example commercial applications are agricultural and industrial waste streams, such as combustion flue gases, biogas and landfill gas that contain CO_2 [194]. Complexities may, however, arise in applying oxide perovskites in these CO_2 containing waste streams because of presence of large amount of gases other than CO_2, e.g. SO_2, that may poison the oxide perovskite catalysts. Considering these complexities, commercialization of oxide perovskite catalysts is likely to entail further research conducted by considering real world conditions.

2.6. Conclusion and Future Outlook

This review documents the latest advances in synthesis methods, strategies for bandgap engineering, and photocatalytic CO_2 reduction performance of widely researched categories of perovskite oxide nanomaterials, i.e. titanates, niobates, tantalates and cobaltates. Different combinations of dopants, as well as varying the A and B elements in perovskite oxides, can have dramatic impacts on their properties and photocatalytic activities. DFT models and currently applied doping methods demonstrate that perovskite oxides can be engineered to possess valence band energies for triggering water oxidation and conduction band energies to donate photogenerated electrons to facilitate CO_2 photoreduction.

Researchers will continue to study perovskite oxide nanomaterials for the photoreduction of CO_2 because of the technological importance of these materials, owing to the following: their tunable band gap, visible light photoactivity; and nanoscale morphology that promotes quantum confinement and high surface area. However, in spite of interesting properties, challenges remain in the technology from the standpoint of photocatalysis, some of which are: intrinsically most of perovskite oxides are large band gap materials; issues with degradation of perovskite oxides during use and storage; and the lack of effective scale-up methods for producing the materials. Challenges are also foreseen in the attainment of satisfactory SFE for enabling commercialization, product selectivity, and translation of laboratory scale technology to industrial scale. So it is more logical to practice some sophisticated techniques and rational designs on existing benchmark material for photocatalytic activity enhancement.

3. Enhancement of Photocatalysis Using Photonic Crystals and Plasmons

Nearly one hundred years ago, humans were dedicated to master flying, but the Wright brothers did not succeed in a day; one hundred years later, we are placing intensive efforts in manipulating light. Hence, the concept of nanophotonics was proposed for exploiting and manipulating light-matter interactions by Motoichi Ohtsu in 1993[195]. Scientists design photonic nanostructures at subwavelength scales to interact with the propagation of light for promising applications such as photocatalysis, enhanced photovoltaic, bio-therapies, and others. In general, nanophotonic techniques include but are not limited to, photonic crystals, plasmonics, metamatierals, and quantum dots. This report will introduce photonic crystals and plasmonics based on the focus of my PhD research.

3.1. Photonic Crystal Enhanced Photocatalysis

One of the significant research fields in the broad area of nanophotonics is the science and technology of photonic crystals (PhCs). PhCs have been widely studied for over two decades to understand how matter can be used to manipulate the propagation of light, and also as a potential method to solve many practical problems in optical sensing and waveguide optics. When light propagates through a path with a periodic refractive index, photons behave in a manner similar to electrons propagating through an atomic lattice. This periodicity of the photonic lattice provides a photonic band gap similar to the electronic band gap in solid-state materials. From a quantum theoretical perspective, photons with particular energy are forbidden from existing in this periodic modulated nanostructure due to Bragg diffraction or scattering on lattice planes, which is called photonic band gap or photonic stop band. Because of this property, the photonic crystal can either reflect undesired wavelengths or suppress spontaneous emission to enhance light utilizing

efficiency. In addition, it is also capable of trapping desired wavelengths of light or slowing down the propagation of photons for better light absorption. Considering these superior capabilities, photonic crystals have been utilized in many light-matter applications for better confinement and manipulation of photons. In Figure 25, we give simplified examples of photonic crystal structure[196], band structure of photonic crystal[197], and light propagation at multilayer structure[197].

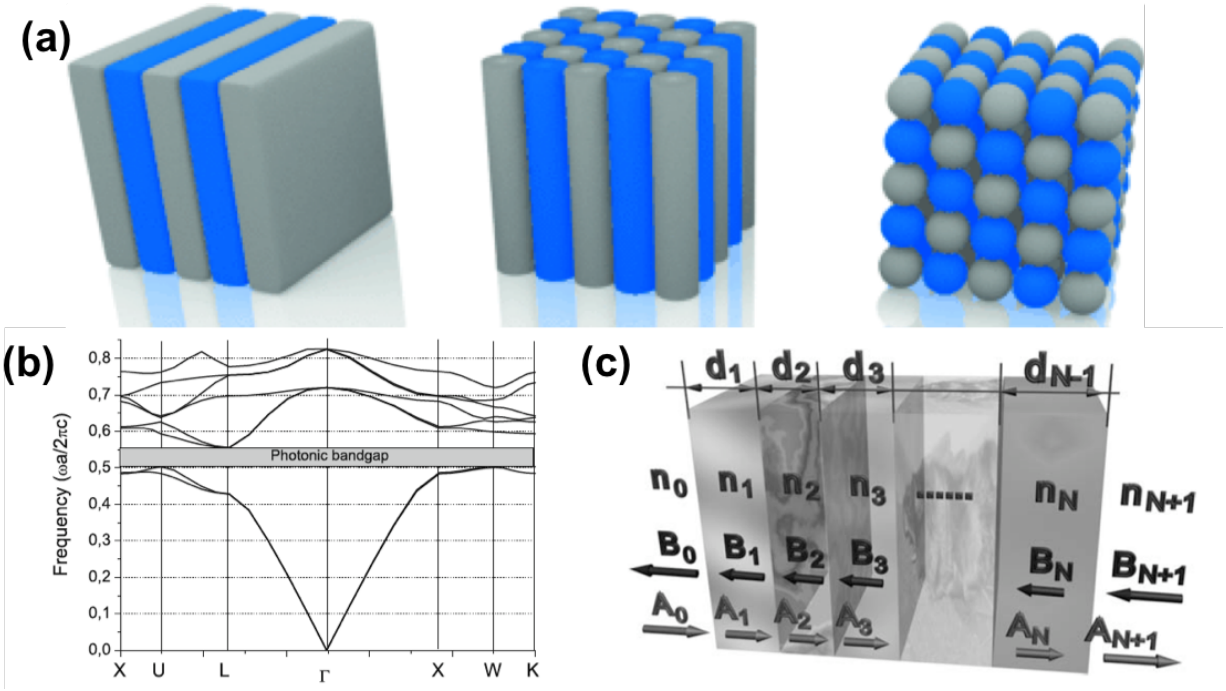

Figure 25: (a) Examples of 1D, 2D, 3D photonic crystal structures, reprinted with permission from Wiley copyright 2014; (b) example of photonic bandgap structure; (c) representation of multilayered structures and light propagation at each layer, reprinted with permission from Springer copyright 2009.

To better understand light propagation in a periodic structure, consider the Bragg reflection equation which explains the relation between reflected wavelength (λ), effective refractive index of the medium (*n*), and periodic lattice distance (*d*).

$$m\lambda = 2n_{eff}d \tag{6.}$$

From Maxwell's equation, the wave function of electric field can be presented as an eigenvalue of this differential equation:

$$\vec{\nabla} \times \frac{1}{\varepsilon(\vec{\gamma})} \vec{\nabla} \times \vec{E}(\vec{\gamma}) = \left(\frac{-1}{c^2}\right) \frac{d^2\, \vec{E}(\vec{\gamma})}{dt^2} \tag{7.}$$

According to the Bloch theorem, the electric field is periodic as follow:

$$\vec{E}(\vec{r}) = \vec{E}_{n,\vec{k}} \cdot e^{i(\vec{k}\cdot\vec{r})} \tag{8.}$$

The periodic modulation of dielectric field can be presented as below, where *a* is the pitch of the periodic lattice:

$$\varepsilon(\vec{r}) = \varepsilon(\vec{r} + \vec{a}) \tag{9.}$$

If the harmonic time is dependent on the frequency of light, then the vector of field is an eigenfunction as follow:

$$\overrightarrow{(\nabla} + \mathrm{i}\vec{k}) \times \frac{1}{\varepsilon(\vec{\gamma})} (\vec{\nabla} + \mathrm{i}\vec{k}) \times \vec{E}(\vec{\gamma}) = \left(\frac{\omega^2}{c^2}\right) \vec{E}(\vec{\gamma}) \tag{10.}$$

where $\varepsilon(\vec{r})$ is the function of dielectric constant at position *r*, ω is the frequency of light, *c* is light speed, and *a* is the periodic lattice distance. As a result, when $k = n\frac{\pi}{a}$ where *n* is integer, the periodic system shows a high reflection at this frequency. Thus, the band structure of this periodic system is a function of wave vector at aforementioned discrete frequencies.

In other words, it means the electromagnetic fields exist as integer combinations of the discrete eigen-values. From energy perspective, it has to satisfy the condition that the lowest energy state of the eigen-mode has to minimize the following equation:

$$\left(\frac{\omega^2}{c^2}\right) \Longrightarrow min \frac{\oiiint \left|(\vec{\nabla} + \mathrm{i}\vec{k}) \times \vec{E}_{n,\vec{k}}\right|^2 d\Omega}{\oiiint \varepsilon \left|\vec{E}_{n,\vec{k}}\right|^2 d\Omega} \tag{11.}$$

Hence, it needs to maximize the denominator. Based on this assumption, the field of the lowest energy state tends to stay in the high dielectric constant region. It also explains why we have Bragg reflection at the interfaces.

Although scientists have studied photonic crystals in detail, the achievement of high quality PhC is a fabrication challenge requiring delicate structures and nanoscale fabrication techniques. The difficulty of fabrication generally increases going from 1D to 2D to 3D PhCs respectively. Normally 1D photonic crystals consist of multiple stacking layers with alternating refractive index, which do not require delicate design in structures. And as such, fabrication is relatively easy and diverse fabrication methods have been used such as sputtering, evaporation, spin-coating, CVD approaches, etc. Regarding 2D PhC, the fabrication methods are more complicated than for making 1D PhC, for example, anodization, photolithography, etc. As for 3D photonic crystals, it is very challenging to achieve a photonic band gap in all orthogonal directions. Therefore, it requires the most advanced fabrication techniques such as electron beam lithography, nanoimprinting and holographic technique. However, there are some methods that are inexpensive and easy to implement. For instance, polystyrene spheres are employed to make 3D PhC using self-assembly methods. Subsequent to self-assembly, polystyrene sphere arrays can be engineered or substituted by other materials using CVD methods. The selection of materials is based on targeted applications. This method broadens the possible applications for 3D PhCs. Although it provides a potential way for low cost mass-production, the cons of this method are also obvious, which are only limited to fcc PhC, not as precise as lithographic methods, and an inability to control defects.

Photocatalysis can benefit from PhC to achieve higher energy conversion efficiency through the more effective utilization of incident light. Many scientists have proved the enhancement from PhC for practical application results. Li and co-authors demonstrated that TiO_2 hollow spheres with tunable shell thickness and sphere diameters can facilitate photocatalytic activities by photonic crystal stop band effect and multiple scattering[198]. Chen et al. reported a dramatical enhancement in practical photochemistry when the photonic band gap matched the electronic bandgap causing slow photon effect[199]. Liao et al. studied coupling TiO_2/P3HT photonic crystal to obtain better visible light absorption and achieve higher photocatalytic efficiency[200]. Zhang and co-authors proved the increase of light absorption due to photonic crystal light trapping effect. In their report, when the resonant wavelength matched with photonic band gap, the localized surface plasmon resonance was boosted because the photonic crystal trapped the light in the region and resulted in strong electric field intensity[94]. Similar work was reported by Zhang et al. demonstrating that improved hot electron generation and injection can be achieved by tuning the pore size of TiO_2 to match the PhC band with the SPR wavelength[201].

3.2. Plasmon Enhanced Photocatalysis

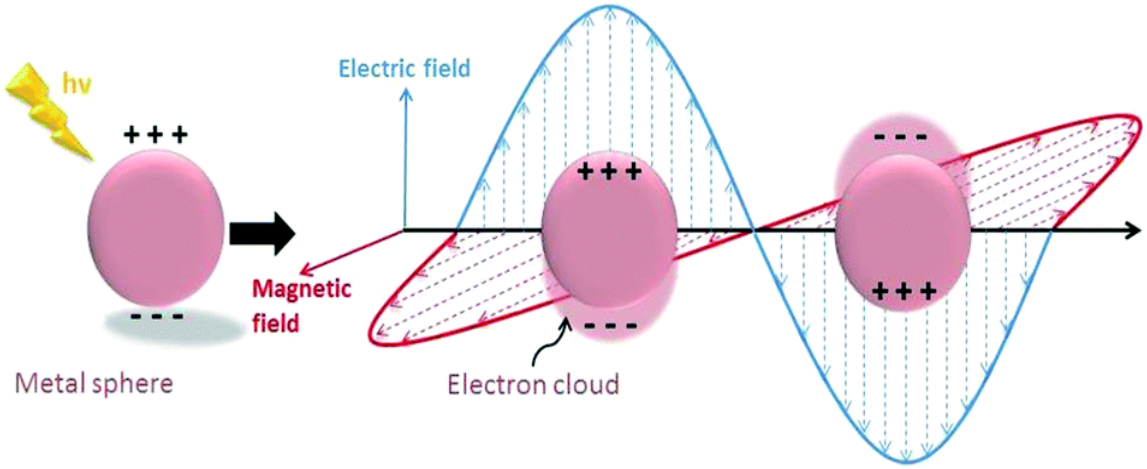

Figure 26: Schematic illustration of LSPR in metal nanoparticles. reprinted with permission from Catalysis Science & Technology copyright 2016.

Pines and Bohm first time studied the oscillation of electrons in metals from which the collective and coherent excitations of conduction band electrons in metal are named plasmons[202]. Figure 26 is a schematic illustration of LSPR in metal nanoparticles showing the collective oscillation of electrons. Plasmonics is a field of study dedicated to utilizing coupled electron-photon states (plasmon polaritons) in practical applications such as therapeutics[203], photovoltaics[204], surface enhanced Raman spectroscopy[205], heat assisted magnetic recording[206], photocatalysis[207], etc. When an electromagnetic wave (of frequency lower than the plasma frequency) interacts with a metal-dielectric interface, it stimulates the motion of electrons and holes which then proceed to absorb energy from the electromagnetic field through damping. The most common and useful modes of these oscillations are localized surface plasmon resonance and surface plasmon polaritons. When obliquely incident light interacts with a large planar metal surface, surface plasmon polariton (SPP), a type of plasmonic oscillations wherein the collective motion of electrons is strongly coupled to the wave vector of the incident photon, propagates

longitudinally along the metal surface as an evanescent wave. On the other hand, localized surface plasmon resonance (LSPR) is confined at small metal nanostructures and oscillate transversely.

In LSPR, we mainly consider noble metal nanoparticles at which the coupling of electromagnetic wave with conduction band electrons occurs. Essentially, it is the incident light frequency that matches with the oscillation frequency of conduction electrons at the metal nanoparticle-dielectric medium interface. Keeping in mind that the size of nanoparticles is much smaller than the wavelength of incident light, normally, the oscillating electric field corresponding to the incident photons is spatially invariant and time-varying (quasi-static approximation). This resonance is affected by the inherent properties of the material resulting in dependence on intensity, field enhancement, extinction coefficient etc. It can be deduced by quasistatic approximation. The Laplace equation for the scalar potential has following expression:

$$\nabla^2 \Phi = 0 \qquad (12.)$$

Alternatively, the electric field can be presented by the gradient of the scalar potential:

$$\vec{E} = -\nabla \Phi \qquad (13.)$$

The electric field inside the sphere caused by an incident plane wave polarized along the x-direction was found to be a constant:

$$\vec{E}_{in} = -\mathrm{A}\vec{\mathrm{x}} = -A(\vec{r}\sin\theta\cos\phi + \vec{\theta}\cos\theta\cos\phi - \vec{\phi}\sin\phi) \qquad (14.)$$

where A is the amplitude of the potential.

On the other side, the electric field outside the sphere is the sum of external uniform field and the induced dipole, which leads to the following equivalence:

$$\vec{E}_{out} = \mathrm{E}\left(\vec{r}\sin\theta\cos\phi + \vec{\theta}\cos\theta\cos\phi - \vec{\phi}\sin\phi\right) + \frac{B}{r^3}(2\vec{r}\sin\theta\cos\phi - \vec{\theta}\cos\theta\cos\phi - \vec{\phi}\sin\phi) \quad (15.)$$

where B is the amplitude of the dipole potential.

From the boundary condition when r is infinity and r at the surface of sphere,

$$\mathrm{A} = \left(\frac{3\,\epsilon_d}{2\,\epsilon_d + \epsilon_m}\right)\mathrm{E} \quad (16.)$$

$$\mathrm{B} = R^3\left(\frac{\epsilon_m - \epsilon_d}{2\,\epsilon_d + \epsilon_m}\right)\mathrm{E} \quad (17.)$$

Wherein ϵ_d is permittivity of dielectric, ϵ_m is the permittivity of metal.

A metal nanoparticle under the electric field is polarized in the potential drop direction as a dipole.

The polarizability of the spherical nanoparticle is defined as follows:

$$\alpha = \frac{4\pi\epsilon_0\epsilon_d(\epsilon_m - \epsilon_d)R^3}{2\epsilon_d + \epsilon_m} \quad (18.)$$

When $\epsilon'_m = -2\,\epsilon_d$, the polarizability is maximum.

To acquire the field at the surface of metal nanoparticles, $\epsilon'_m = -2\,\epsilon_d$, $\theta = \frac{\pi}{2}\ and\ \emptyset = 0$,

$$\vec{\mathrm{E}}_{out} = \left(1 + \frac{2(\epsilon_m - \epsilon_d)}{2\epsilon_d + \epsilon_m}\right)\mathrm{E}\hat{r} = \frac{3\epsilon'_m}{i\epsilon''_m}\mathrm{E}\hat{r} \quad (19.)$$

Normally, for noble metals, $|\in_m^{'}|$ is much larger than $|\in_m^{''}|$. According to Equation 15, the magnitude of the enhancement is three times of the ratio of the dielectric constant of the real part vs. imaginary part, which can result in several orders of magnitude of enhancement at resonance.

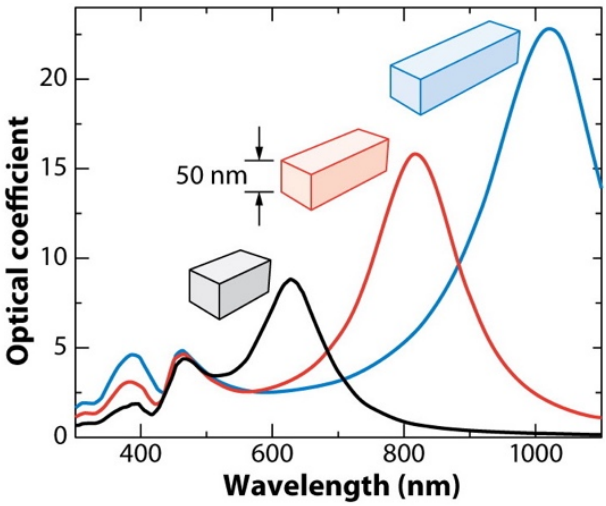

Figure 27: Extinction spectra of Ag nanoparticles with various aspect ratios: 2:1 (black line), 3:1 (red line), 4:1 (blue line) respectively. Copyright 2007 American Chemical Society.

Typically, this metal-dielectric surface plasmon resonance frequency can be derived using the Drude-Lorentz model. The net force on the electron in a metal is given by:

$$F_{net} = m\frac{d^2x(t)}{dt^2} = -m\omega_0 x(\mathrm{t}) - \mathrm{qE(t)} - \Gamma\frac{\mathrm{dx(t)}}{\mathrm{dt}} \qquad (20.)$$

When the size of nanoparticle is much smaller than the wavelength of light, the spatial variation of the electric field is negligible. Hence, the electric field and spatial functions can be written as follows:

$$\mathrm{E(t)} = E_0 e^{-i\omega t} \qquad (21.)$$

$$\mathrm{x(t)} = x_0 e^{-i\omega t} \qquad (22.)$$

Inserting the above expression into Equation (16.):

$$-\omega^2 x_0 + \frac{\Gamma}{m}(-i\omega x_0) = -\frac{qE_0}{m} \tag{23.}$$

$$\mathrm{x(t)} = \frac{{}^{q}/_{m}}{\omega^2 + {}^{-i\omega\Gamma}/_{m}} E_0 e^{-i\omega t} \tag{24.}$$

The polarization P can be described as:

$$\mathrm{P} = -\mathrm{nqx(t)} = -\frac{{}^{nq^2}/_{m}}{\omega^2 + {}^{-i\omega\Gamma}/_{m}} E_0 e^{-i\omega t} \tag{25.}$$

To find the dielectric constant, we need replace the displacement by polarization:

$$\mathrm{D} = \epsilon\epsilon_0 E = \epsilon_0 E + P = \epsilon_0 E_0 e^{-i\omega t} - \frac{{}^{nq^2}/_{m}}{\omega^2 + {}^{-i\omega\Gamma}/_{m}} E_0 e^{-i\omega t} \tag{26.}$$

To simplify the expression, the plasma frequency and the damping frequency in the metal are defined as follows, respectively：

$$\omega_p^2 = \frac{nq^2}{m\epsilon_0} \tag{27.}$$

$$\gamma = \frac{\Gamma}{m} \tag{28.}$$

The dielectric constant of the metal can be split into a real part and an imaginary part:

$$\epsilon = \left[1 - \frac{\omega_p^2}{\omega^2 + \gamma^2}\right] + i\left[\frac{(\frac{\gamma}{\omega})\omega_p^2}{\omega^2 + \gamma^2}\right] \tag{29.}$$

The absorption coefficient has an expression using the imaginary part of dielectric constant, just like the expression using wavevector k, which indicates the peak of plasmon absorption depends on the dielectric constant of the surrounding medium:

$$\alpha = \frac{\omega \epsilon''}{nc} \tag{30.}$$

Meanwhile, the peak of absorption is also related to the dielectric constant of metal. At high frequency, ϵ_∞ is close to 1, and the damping frequency γ is negligible comparing to ω. A more convenient expression is presented as follow:

$$\epsilon' = \epsilon_\infty - \frac{\omega_p^2}{\omega^2} \tag{31.}$$

Because the condition of plasmon resonance is when $\epsilon' = -2\epsilon_m$, the relationship between the resonance peak and the metal dielectric constant can be written as:

$$\omega_{LSPR} = \sqrt{\frac{\omega_p^2}{\epsilon_\infty + 2\epsilon_m}} \approx \frac{\omega_P}{\sqrt{1+2\varepsilon_m}} \tag{32.}$$

Once the resonance is generated, it will decay rapidly in one of the following damping mechanisms: radiative damping, thermalization, Landau damping, electron-electron scattering. The most relevant mode to our study is Landau damping, the mechanism by which hot electron/hole pairs are generated. What happen next is that, if a reagent is within the reach of generated hot electrons or holes, then the reagent will be either reduced by energetic electrons or oxidized by holes, the process which is known as chemical interface damping. This described process is the theoretical foundation of plasmon involved photocatalysis. As we explained above, SRP and LSPR generate high kinetic energy charge carriers, which can boost practical performance. However, due to the

nature of high energy, these hot electrons or hot holes tend to relax extremely quickly, and have lifetimes in the range of a few hundred femtoseconds. This also underscore the importance of rational design of catalysts in many aspects including morphology, material selection, etc. Considering our research works, metal/semiconductor is the most commonly utilized framework providing effective charge transfer, suppressing recombination, improving visible light absorption, generating highly energetic electrons/holes and enhancing the local electric field. A variety of noble metals are commonly utilized based on their suitability to corresponding applications, for example, Pt for hydrogen evaluation, Cu for CO_2 reduction, Ag for dye-degradation, Au for bio-therapy and so on.

4. Optical Control of Selectivity of CO_2 Photoreduction Using Au-TiO_2 Plasmonic Photonic Crystal Catalyst

The above sections have detailed the basics of PhC and SPR. This section focuses on the utilization of aforementioned theories into practical CO_2 photocatalytic reduction. It is a summation of a completed work. The results from this work presented in the following section are proofs of feasibility and enhancement in photocatalysis.

4.1. Synthesis of Au-TiO_2 photocatalyst

Ti foil was cut into 2.5×2.5 cm pieces and washed using soap water, followed by sonication in DI water, acetone, and methanol successively for 10 min each. After being dried under a nitrogen stream, the Ti pieces were chemically polished by dipping into a mixed acid solution of 2:1:1 HNO_3: HF: CH_3COOH (v/v). They were then rinsed in DI water and stored in a methanol bath. Before anodization, foils were dried under a N_2 stream and then adhered to 2.5×4.5 cm aluminum foils to improve uniformity by ensuring constant potential across the back of the foil. The Ti foil was anodized using charge-controlled pulse anodization in a two-electrode cell using a 2.5×4.5 cm Ti counter electrode. Anodization was performed using a 3-step charge-controlled pulse for 30 to 100 periods in an ethylene glycol based electrolyte (0.3 wt% NH_4F, 4 vol% DI) at 65 °C. After anodization, the as-formed PMTiNT on Ti foil was detached from the aluminum backing and soaked in methanol and hexane for 5 and 3 min respectively, to clean off the electrolyte and ensure low surface-tension for drying. It was found that using high surface-tension solvents to clean the PMTiNT caused it to crack and delaminate from the Ti substrate. Finally, the as-prepared PMTiNT were annealed in a 3-zone tube furnace (STF55666C-1, Thermo Scientific Lindberg/Blue M),

increasing from room temperature to 525 °C in 4 h and held at 525 °C for an additional 4 h. The 3-step anodization pulse consisted of a positive charge-controlled 60 V period, followed by 2 seconds of -4 V, and 20 s of 0 V. The charge was kept constant across pulses by integrating current over time using a 0.1-ohm shunt resistor in series with the cell, which was measured using an Arduino ATmega328P, and shut off once it reached the desired value. During the 20 s of 0 V, the anode and cathode were shorted to quickly remove any lingering static potential between the electrodes. For Au nanoparticle decoration, as-prepared PMTiNT was loaded in a DC magnetron sputter system (Kurt J. Lesker Co.). The base pressure was 7 mTorr, the power applied to the Au target was 75 W and the duration of sputtering was 1 min. Following sputtering, samples were annealed in the 3-zone tube furnace again at the same temperature (525 °C) for 30 min. Figure 28 is the schematics of fabrication process for Au-PMTiNT photocatalysis.

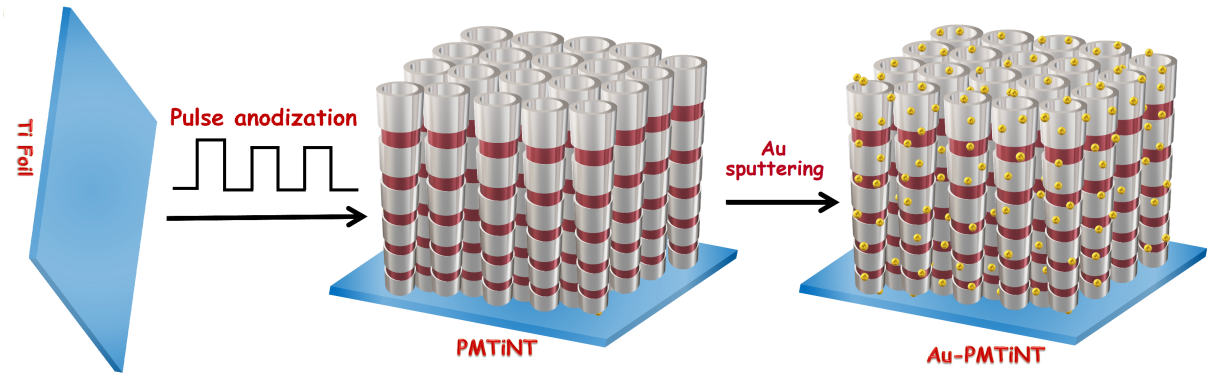

Figure 28: Schematics of fabrication process for Au-PMTiNT photocatalysis.

4.2. CO_2 photoreduction experiments

The photocatalyst PMTiNT or Au-PMTiNT was loaded in a cylindrical reactor (32 mL internal volume) having a quartz window, as mentioned in our previous report [21]. One piece of Au-PMTiNT photocatalyst was placed in the reactor, which was charged with 200

μL DI water and 50 psi of CO_2. Prior to introducing CO_2, the reactor was purged several times with N_2 gas followed by CO_2 and finally the CO_2 pressure was maintained at 50 psi. Subsequently, the reactor was placed on a hot plate heated to 80 °C to evaporate water droplets. To investigate CO_2 to CH_4 photocatalytic reaction, the loaded reactor was illuminated under collimated AM 1.5 G irradiation from a Class A solar simulator (Newport-Oriel instrument USA) for 2 h. The power density at the surface of the samples was 100 mW cm^{-2}. The sample was also irradiated with 50 W white cold LED light ($\lambda >$ 400 nm, max. intensity at 510 nm, Model: GT-FL001-50W, Power density 1 mW cm^{-2}) for 2 h, followed by solar simulator for 2 h. Further, to investigate the effect of wavelength on the product selectivity and probe the Z-scheme photoreduction mechanism, the photocatalyst loaded reactor was illuminated by 365 nm (UV light) and 505 nm (green light) LEDs, simultaneously for 2 h. The power density on the surface of samples was 5 and 10 $mWcm^{-2}$ for 365 nm and 505 nm LEDs respectively. Subsequent to each irradiation step, the obtained gas samples were analyzed by a Shimadzu gas chromatograph (GC-2014) equipped with a Porapak Q column and a molecular sieve column, and a pulsed discharge detector (PDD). Conditions: He carrier flow rate: 0.5 mL min^{-1}, detector temperature: 160 °C, oven temp: started from 60 °C and raised up to 160 °C to expel water vapor. In addition, isotope labeling experiments using $^{13}CO_2$ instead of $^{12}CO_2$ were carried out under identical conditions to rule out contamination from ^{12}C source. Gas chromatography-mass spectrometry (GC-MS) was employed to analyze the obtained gas samples and verify that the products were generated from the photocatalytic reaction.

4.3. Results and discussion

As evident from FESEM imaging of PMTiNT, the pulsed anodization method forms a periodically modulated nanotube structure with an average diameter of 80 nm. The top view and side view of PMTiNT are shown in Figure 29 and Figure 30 respectively.

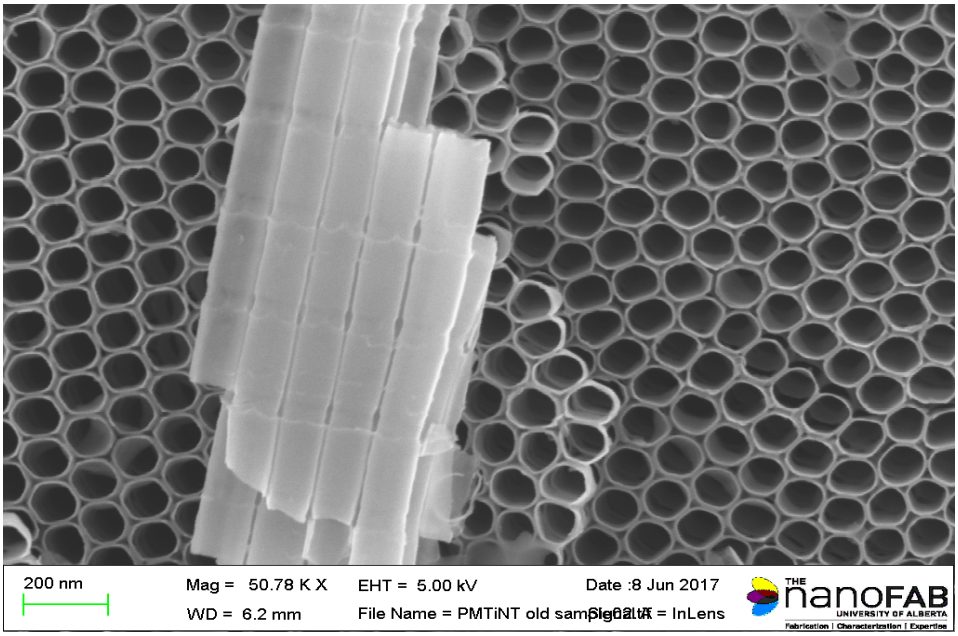

Figure 29:Top view of periodic modulated TiO_2 nanotubes, indicating tube diameter is around 80nm.

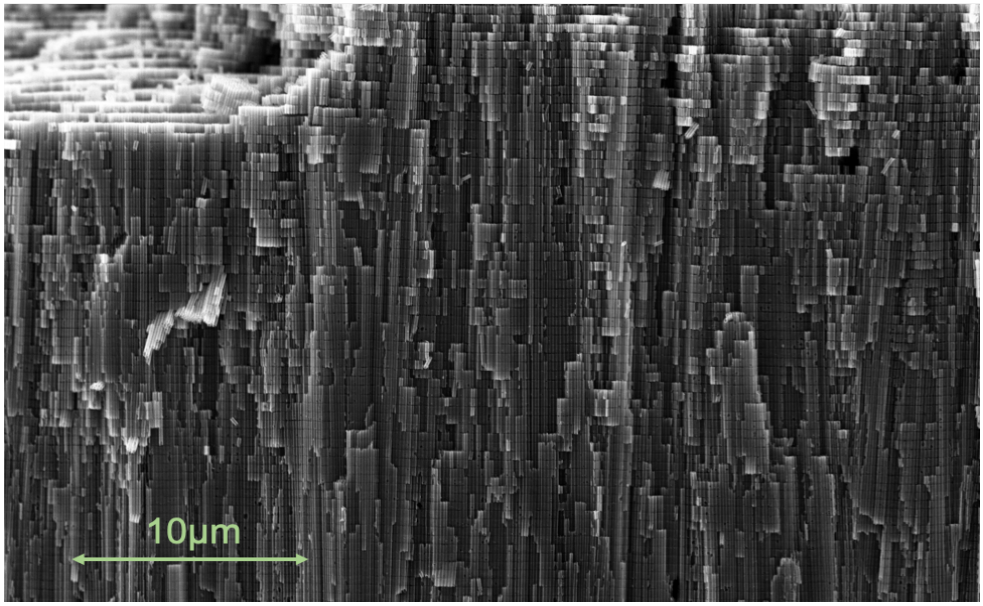

Figure 30：Side view of periodic modulated TiO_2 nanotube arrays.

The periodic density of the TiO_2 phase results in oscillatory dielectric constants that influence photon propagation. Thus, desired photonic band gaps (PBGs) can be obtained by modifying the structure's periodicity, which is controlled by the quantity of constant charge used during pulsed anodization. To obtain the desired photonic band gap, the length of low-refractive index periods is controlled via tuning the quantity of anodization charge. TEM images of Au-PMTiNT indicate Au NPs with a diameter ranging from 5-8 nm are deposited throughout the nanotubes (Figure 31).

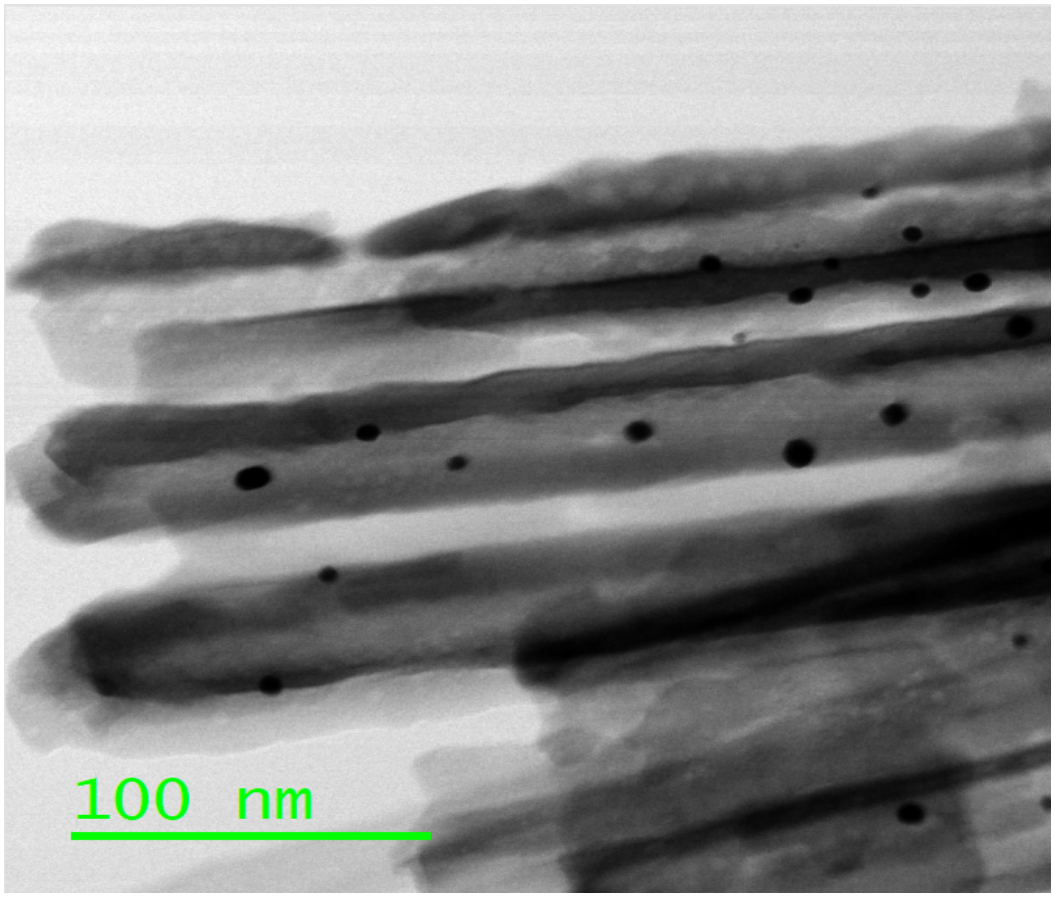

Figure 31 : TEM image of Au nanoparticles loaded PMTiNT nanotubes, showing gold particles are 5-8 nm in diameter.

Electrochemical anodization method is not an ideal fabrication method for high quality factor photonic crystals, despite the advantage of large area self-assembling. Conventional anodization process is either potentiostatic or galvanostatic, each having its own advantages and disadvantages. Potentiostatic anodization allows a relatively constant radius along the nanotube growth, but length of the nanotube poorly controlled by anodization time due to the etching speed is not constant throughout the growth, while galvanostatic anodization can precise control of the length, but with less consistency in radius. As we discussed earlier, the position of photonic band gap depends on the periodically modulated refractive index, which is keenly related to the ratio of air to TiO_2. Thus, we developed a novel anodization profile using constant voltage versus electric charge, which allows us to keep the consistency in both radius and length. Figure 32 presents the relationship between anodization charge, period length, and PBG wavelength.

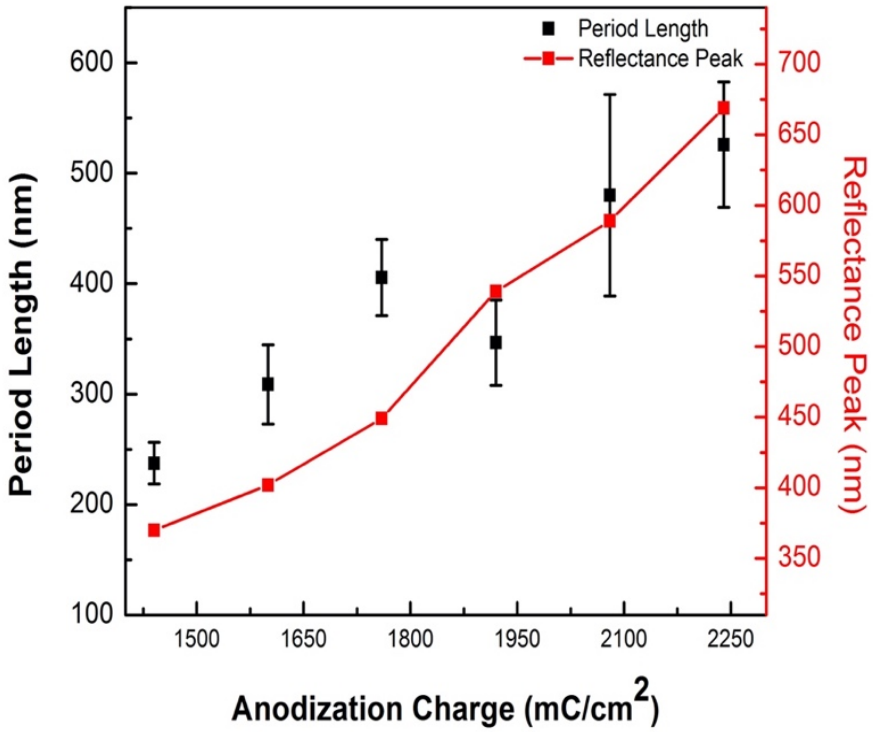

Figure 32: Illustration of charge-controlled pulse anodization process for photonic crystal structure.

The X-ray diffraction (XRD) pattern for Au-PMTiNT split into its component signals exhibited various specific peaks corresponding to anatase TiO_2 (JCPDS# 21-1272), rutile TiO_2 (JCPDS# 21-1276), Au (JCPDS# 04-0784) and Ti respectively (Figure 33). The rutile phase signal intensity was too low, indicating anatase to be the main phase in Au-PMTiNT.

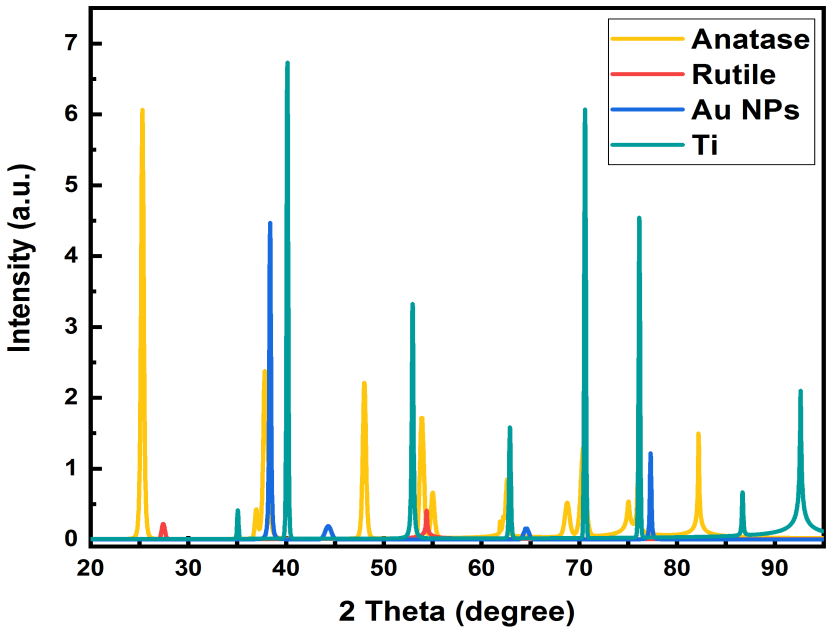

Figure 33: XRD pattern of Au-PMTiNT, illustrating material components and TiO_2 phase by separating signals.

The interaction with light is critical for photocatalysts, which was examined using diffuse reflectance UV-Vis spectroscopy and Lumerical® FDTD simulations. The UV-Vis diffuse reflectance spectrum of PMTiNT (black line in Figure 34) shows a broad photonic stopband from 350 to 550 nm, which is supported by simulated reflectance of PMTiNT (blue dash line in Figure 34) showing three sharp PBGs at 350 nm, 400 nm, and 550 nm. After Au sputtering (red line in Figure 34), the reflectance of the photonic stopband is damped drastically. The absorption band edge is shifted to 386 nm which is characteristic of the anatase bandgap. Additionally, the reflectance valley is shifted at 550 nm due to the absorption of the localized surface plasmon resonance (LSPR) of Au NPs.

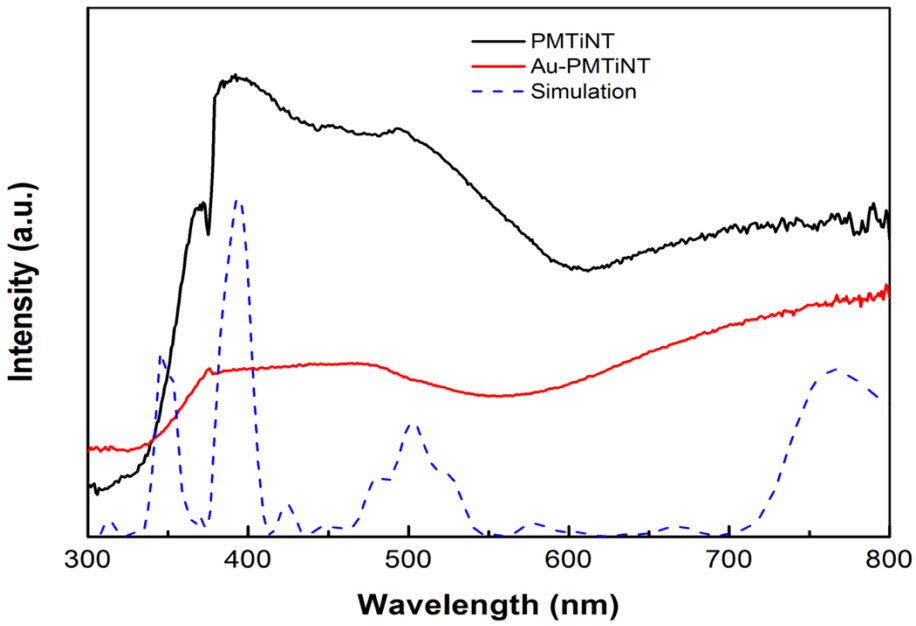

Figure 34:Diffuse reflectance spectra of PMTiNT (black line), Au-PMTiNT (red line), simulated PMTiNT (blue dash line).

The propagation of photons in PMTiNT was investigated through a cross-sectional view of the spatial distribution of Poynting vector field map obtained from Lumerical® FDTD. Clear evidence of periodic high intensity local electric fields is seen in Figure 35 (a), which supported the aforementioned theory that oscillatory dielectric constants forbid the

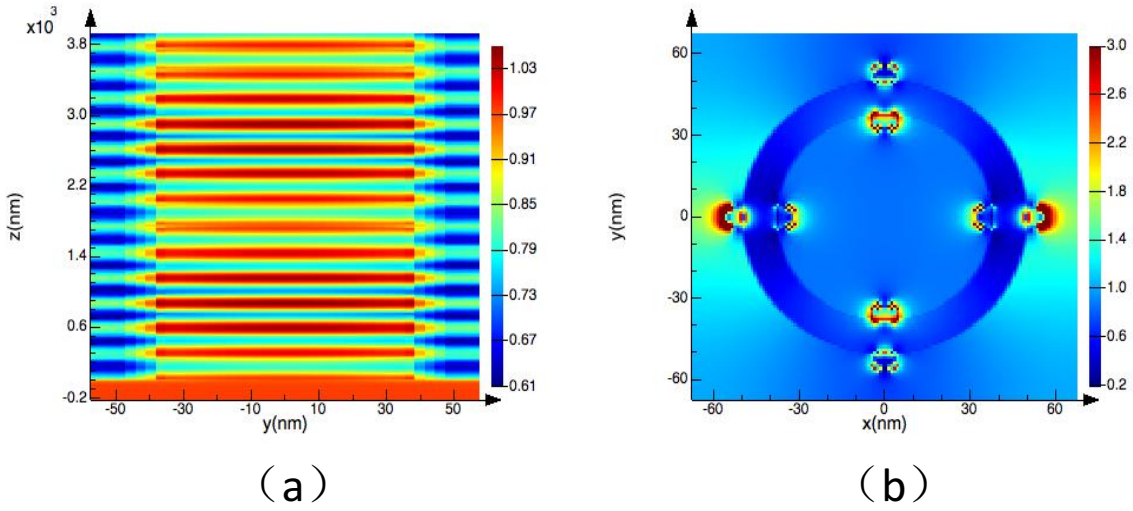

Figure 35:(a) Cross-section view of amplitude of Poynting vector plot of PMTiNT, (b) Top view electric field map for Au-PMTiNT.

propagation of photons of particular wavelengths. In Figure 35 (b), a simulated top view of the absorption caused electric field indicates a strong electric field surrounding the Au NPs under plasmon resonance excitation. These plasmonic Au NPs induced over 10 times higher local field compared to the electric field at the air-TiO_2 interface. The aforementioned plasmonic response and 1D photonic crystal architecture are critical effects that make the Au-PMTiNT nanostructured heterojunction a unique photocatalyst.

The CO_2 photoreduction performance on Au-PMTiNT was investigated under two different irradiation conditions leading to two different reaction pathways 1) Conventional direct route under AM1.5G simulated sunlight and 2) Z-scheme under UV-poor visible illumination followed by AM1.5G simulated sunlight. The CO_2 photoreduction experiments using Au-PMTiNT as a photocatalyst was performed in a stainless steel gas-tight reactor with a quartz window in the presence of gas phase CO_2 and vapor phase H_2O [208]. For the first conventional reaction pathway, the reactor was irradiated under solar simulated AM1.5G simulated sunlight for 2 h. The gaseous products were analyzed by using GC-PDD and GC-MS, and the obtained product yield in ppm was converted into μmol h^{-1}, as mentioned in our previous report [208]. Under simulated sunlight, methane was observed as the dominant CO_2 photoreduction product with a methane formation rate (R_{CH4}) of 302 μmol h^{-1}. Extremely high selectivity manifested in the product composition which consisted of 89.3% methane, 8.5% carbon monoxide, 1.6% hydrogen and 0.6% ethane (Figure 36). To manipulate the reaction into following the second reaction pathway, the experiment was carried out under identical conditions with merely the illumination sequence changed, by first irradiating the reactor with a 50 W white LED (P_{max} at 520 nm) for 2h followed irradiating the reactor with AM1.5G simulated sunlight for 2h respectively. Interestingly, following this illumination sequence, the composition of the photoreduction product was changed drastically compared to

conventional CO_2/CH_4 photocatalysis; formaldehyde (CH_2O) and carbon monoxide (CO) were observed as the primary reaction products (Figure 36). From GC analysis, the CO and CH_2O formation rate (R_{CO} and R_{CH2O}) were extracted to be 323 and 420 µmol h^{-1} respectively. To validate the optical wavelength-directed product selectivity of CO_2 photoreduction on Au-PMTiNT, the photoreaction was also carried out under identical conditions by illuminating with UV light (365 nm) and green light (505 nm) LEDs simultaneously. As anticipated, formaldehyde and CO were observed as major reaction products and no trace of methane was detected. The rate of photocatalytic CO and CH_2O generation were found to be 364 and 123 µmol h^{-1} respectively (Figure 36). To discern if the observed reaction products were truly a result of CO_2 photoreduction and not due to carbonaceous impurities, a series of sanity tests were performed under identical conditions but with absence of one element in control experiments: 1) absence of photocatalyst; 2) absence of water; 3) absence of light; 4) absence of CO_2. No CO_2 reduction product was observed in any of the four control experiments which proved the photocatalytic origin of products.

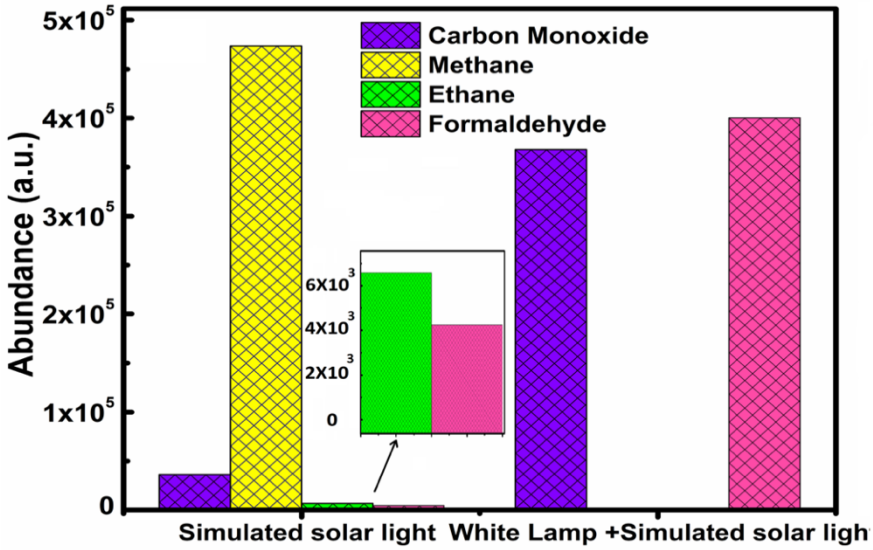

Figure 36: Products chart of two different illumination conditions, dominating products varied under different wavelength illumination.

Additionally, experiments using isotopically labeled $^{13}CO_2$ were also conducted to confirm the origin of observed products and to eliminate possible carbon contamination. The GC-MS spectra of reaction product exhibited ion-chromatogram peaks at *m*/*z* value of 17 for $^{13}CH_4$, 29 for ^{13}CO and 31 for $^{13}CH_2O$ respectively (Figure 37).

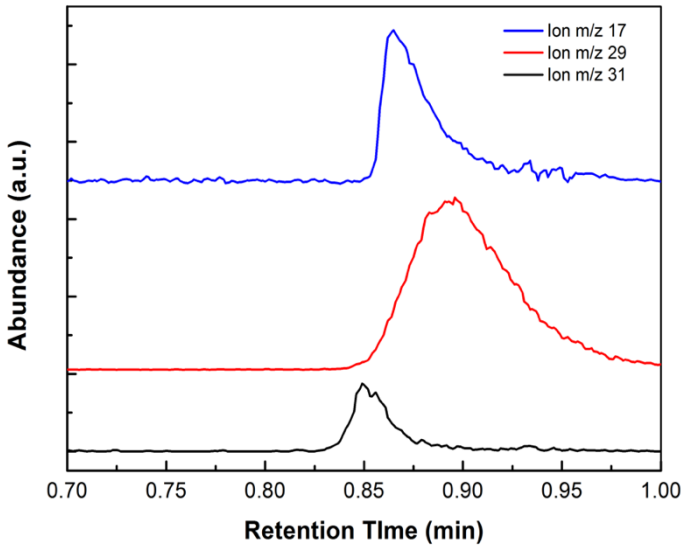

Figure 37: ion-chromatogram indicated existing of ^{13}C isotopic labeled products.

To understand the charge separation mechanism and carrier dynamics in Au-PMTiNT, the surface potential (SP) under different illumination conditions was determined using Kelvin probe force microscopy (KPFM) (Figure 38). Since the gold was sputtered on to the PMTiNTs, the maximum number of Au NPs are found on the top surface of the PMTiNTs, and the charge on these Au NPs determines the surface potential of the Au-PMTiNT samples. Under dark conditions, the SP of Au-PMTiNT was found to be -50 mV (black curve in Figure 38) which demonstrates a slightly electron-rich surface of Au-PMTiNT, which confirmed the presence of a Schottky junction at equilibrium due to transfer of electrons from TiO_2 to Au. Under UV irradiation by 365 nm photons, a negative shift of 300 mV with respect to dark was observed (blue curve in Figure 38). Owing to the large amount of TiO_2 in Au-PMTiNT system and the UV-induced photogeneration in TiO_2, a

flat band or accumulation region is expected to prevail at the Au-TiO_2 interface with the concomitant transfer of a larger amount of negative charge to the Au NPs. The Au NPs thus act as electron sinks for the large excess carrier concentration in TiO_2 under UV illumination, a behavior that is well-documented in prior reports [209, 210]. On the other hand, under 532 nm illumination, Au nanoparticles are the major absorbers due to the LSPR. Under visible illumination, a small positive shift (25 mV) was observed which indicates the transfer of hot electrons into E_{CB} of TiO_2 across the Schottky junction following absorption and plasmon dephasing, thus leaving positively charge holes on the Au NPs. The electrons transferred to TiO_2 following LSPR excitation and damping, have extremely long lifetimes (seconds to hours) due to two major reasons: (1) The extremely low residual hole concentration in TiO_2 that discourages recombination and (2) The high dielectric relaxation time in TiO_2 due to which thermal equilibration of excess carrier concentrations is a slow process [211, 212]. Consequently, the remnant photogenerated holes in Au also have a long lifetime.

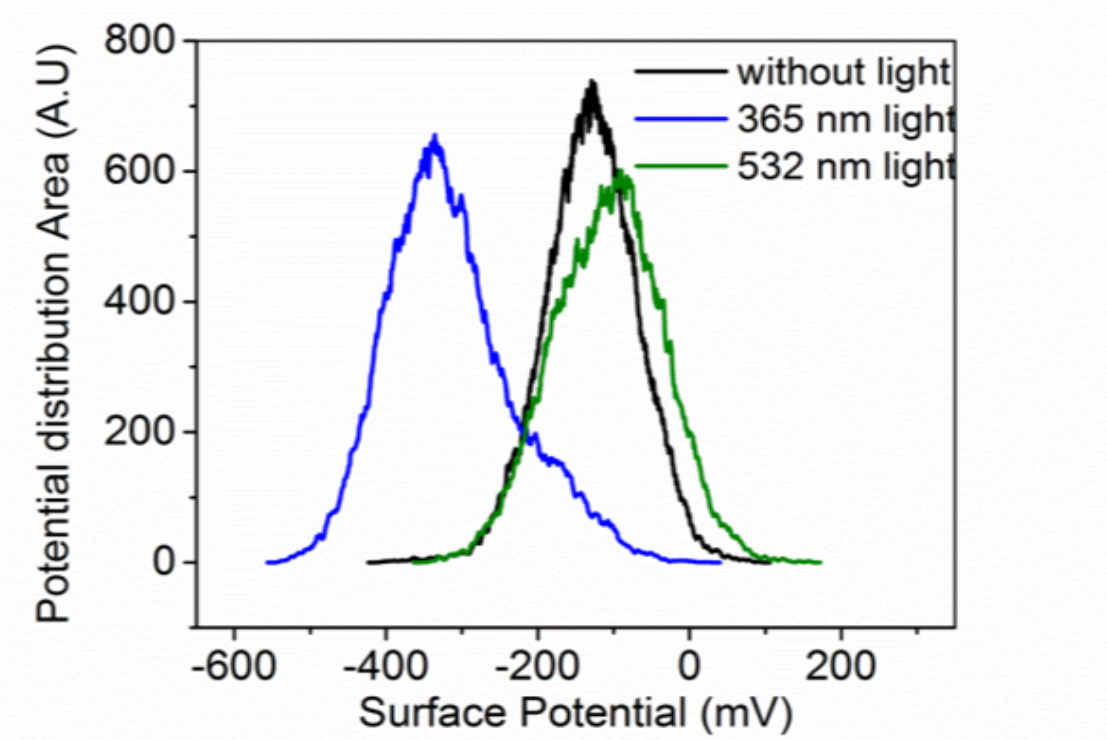

Figure 38: Surface potential shifting under different wav wavelength illumination was measured by KPFM.

Further experiments were used to confirm these inferences. UV-Vis spectra of Au-PMTiNT were measured before and after a 2h white lamp illumination (λ>420 nm) (Figure 39). Figure 39 clearly shows the surface plasmon resonance peak at *ca.* 550 nm. The white LED lamp had maximum intensity around 520 nm; Following illumination and LSPR excitation, the transfer of hot electrons into TiO_2 as described above, significantly increased the concentration of free electrons in TiO_2 which manifested itself as an increased absorbance in the near-infrared (NIR) region in a backward scan (longer wavelength to shorter wavelength) due to enhanced free carrier absorption of NIR photons (Figure 39). Interestingly, after illumination when the sample was scanned in the forward direction (from shorter wavelength to longer wavelengths), no increase in absorbance was observed in the NIR region which suggests that free electrons were used up during UV irradiation. This interesting result provided us the first indication that a plasmonic Z-scheme might be operational in the Au-PMTiNT photocatalyst. Taken together, the picture that emerges from the gas evolute, KPFM and UV-Vis data is that illumination by near-LSPR visible photons alone produces transfer of hot electrons from Au to TiO_2 and illumination by UV photons alone produces transfer of photogenerated electrons from TiO_2 to Au through the electron sink effect of noble metal NPs. Under AM1.5G one sun illumination following visible illumination, an accumulation-type interfacial band alignment exists which promotes a large flux of electrons (both photogenerated electrons and transferred hot electrons) to move from TiO_2 to Au, which in turn recombine with holes in Au generated by plasmon damping. This leaves hot electrons in Au NPs and photogenerated holes in TiO_2 available to drive photocatalytic reactions. Although hot electrons in Au experience

thermalization at picosecond timescales, our gas evolute results clearly indicate that charge transfer to adsorbed CO_2 species occurs within this timeframe.

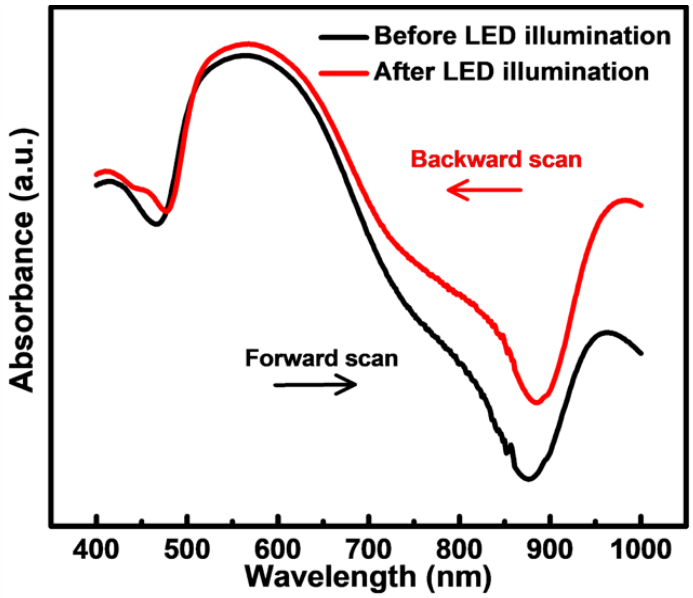

Figure 39: Absorption spectra of as-prepared Au-PMTiNT before and after irradiation of white 50 W, LED lamp (filtered-out UV) (Both collected in the backward scan) After forwarding scan of LED illuminated samples the enhanced absorption peak in NIR region corresponded to free electrons was disappeared and spectra were exactly identical as the non-irradiated sample.

The key question that arises is what factors govern the controllable product selectivity under different wavelength illumination conditions and the underlying mechanism involved. Highly selective methane formation on Au/TiO_2 systems under solar illumination has been previously observed and explained on the basis of energy level positions i.e. the E_{CB} position of TiO_2 which lies above reduction potential of CO_2/CH_4 but remains below the reduction potential of CO_2/CO and CO_2/CH_2O [213]. However, conversion of band positions values on NHE scale at pH 7 actually shows that TiO_2 can reduce CO_2 to CO and CH_2O[214-217]. Further, we calculated that E_{CB} of TiO_2 in Au-PMTiNT to be situated at -0.88 V *vs* NHE at pH 7 suggesting that TiO_2 can reduce CO_2 to CO and CH_2O. Therefore, the energy levels of TiO_2 are insufficient to explain the controllable product selectivity observed by us. The excellent selectivity of methane formation under AM1.5G simulated

sunlight can be explained based on 1) Photonic band gaps[218-220] and 2) Carbene pathway. As mentioned earlier, PBGs of PMTiNT allowed the propagation of selected wavelengths in PMTiNT photonic crystal and enhanced the selectivity of products. The electronic band gap of anatase phase TiO_2 is 3.2 eV which corresponds to a band-edge of 386 nm and only photons with wavelengths longer than 386 nm can induce a direct transition of electrons from the valence band to conduction band. While the conduction band is constituted of Ti^{4+} 3d overlaps, the presence of defect states (Ti^{3+}, O vacancies etc.) creates sub-gap states just below the conduction band and longer wavelengths can also stimulate electronic transition. Due to the presence of photonic stop bands at 350 and 400 nm in the PMTiNT, only light in a narrow range of 355-386 nm remains available for the transition. Photons with wavelengths in the range 386-410 nm, which are primarily responsible for the sub-bandgap excitation of defect states, were attenuated. Due to this filtering effect, only mobile, high energy electrons are excited to the conduction band and react with surface adsorbed CO_2 to form methane. The observation of methane as a sole reaction product (with minor CO) under simulated sunlight support that direct transition of sufficiently energetic electrons to the conduction band of TiO_2 controlled by photonic band gaps prevents defect mediated low energy transitions which might lead to other CO_2 reduction products. Additionally, due to the lower reduction potential of CO_2/CH_4 (-0.24 V *vs* NHE at pH7) in comparison to CO_2/CO (-0.53 V) and CO_2/CH_2O (-0.48 V), formation of methane was thermodynamically more feasible.

Further, gold in Au/TiO_2 Schottky junction can absorb visible light *via* localized surface plasmon resonance (LSPR) and generates hot electrons (energetic electrons) with enough energy to surpass the Schottky barrier which get injected into the E_{CB} of TiO_2 (conventional

mechanism) (Figure 40 (a)-(c)). Further, some fraction of high energy photons was also absorbed which generate more energetic hot electrons and hot holes (energetic holes). Hot holes on the Au are either utilized for water splitting on gold surface or can be migrated to the E_{VB} of TiO_2 where water oxidation takes place. Further two sites water splitting supply of plenty of electrons and protons to sustain complete photoreduction of CO_2 to CH_4.

Unlike selective CH_4 formation under solar simulated light, photoreduction of CO_2 under LED light followed by solar simulator gave formaldehyde and carbon monoxide as major products which suggests the presence of a second mechanism under such conditions. The selective formation of CH_2O and CO can be explained by the Z-scheme mechanism (Figure 40 (d)-(f)). The irradiation of Au-PMTiNT samples with white cold LED light (λ>420 nm) which has maximum power distribution at 520 nm cannot excite electrons from E_{VB} to E_{CB}. While Au can absorb most of light in this region due to LSPR and inject generated hot electrons in E_{CB} of TiO_2 leaving behind poorly oxidizing holes. Despite, the capability of photogenerated hot electrons on gold to perform proton assisted CO_2 reduction, the absence of water spitting to furnish required protons, suppress the reaction. Once solar simulator is turned on electron-hole pairs are generated in E_{CB} and E_{VB} of TiO_2. Due to already established build-in potential electrons in E_{CB} of TiO_2 move rapidly toward Au and recombine with holes there while holes left in E_{VB}, oxidize water to release required electrons and protons (Z-scheme) [221]. Several reports demonstrate transfer of electrons from semiconductors to the gold nanoparticles and Z-scheme catalysis [222-226]. As the spectral distribution of LED was concentrated near to gold LSPR excitation, maximum fraction of photons from LED was used for generation of hot electrons and low energy holes. On the other hand, due to only 5% UV in the solar simulator and faster recombination,

the numbers of generated electrons and holes pairs on TiO_2 was too low than Au. Due to this surface of Au remain populated with less energetic holes and photogenerated electrons in E_{CB} on TiO_2 get recombine to these holes favoring Z-scheme mechanism. Due to less numbers of holes in E_{VB} of TiO_2, the rate of proton generation from water was poor and surface concentration of protons was rate-determining step. The low surface concentration of proton favor proton deficient CO_2 reduction products CH_2O and CO (4 and 2 proton reduction products) via formaldehyde pathway. To validate Z-scheme mechanism reaction was carried out by illumination sample with UV (365 nm) and green (505 nm) LEDs simultaneously having identical power intensity on the surface of the sample. Again, CH_2O and CO were observed as major products.

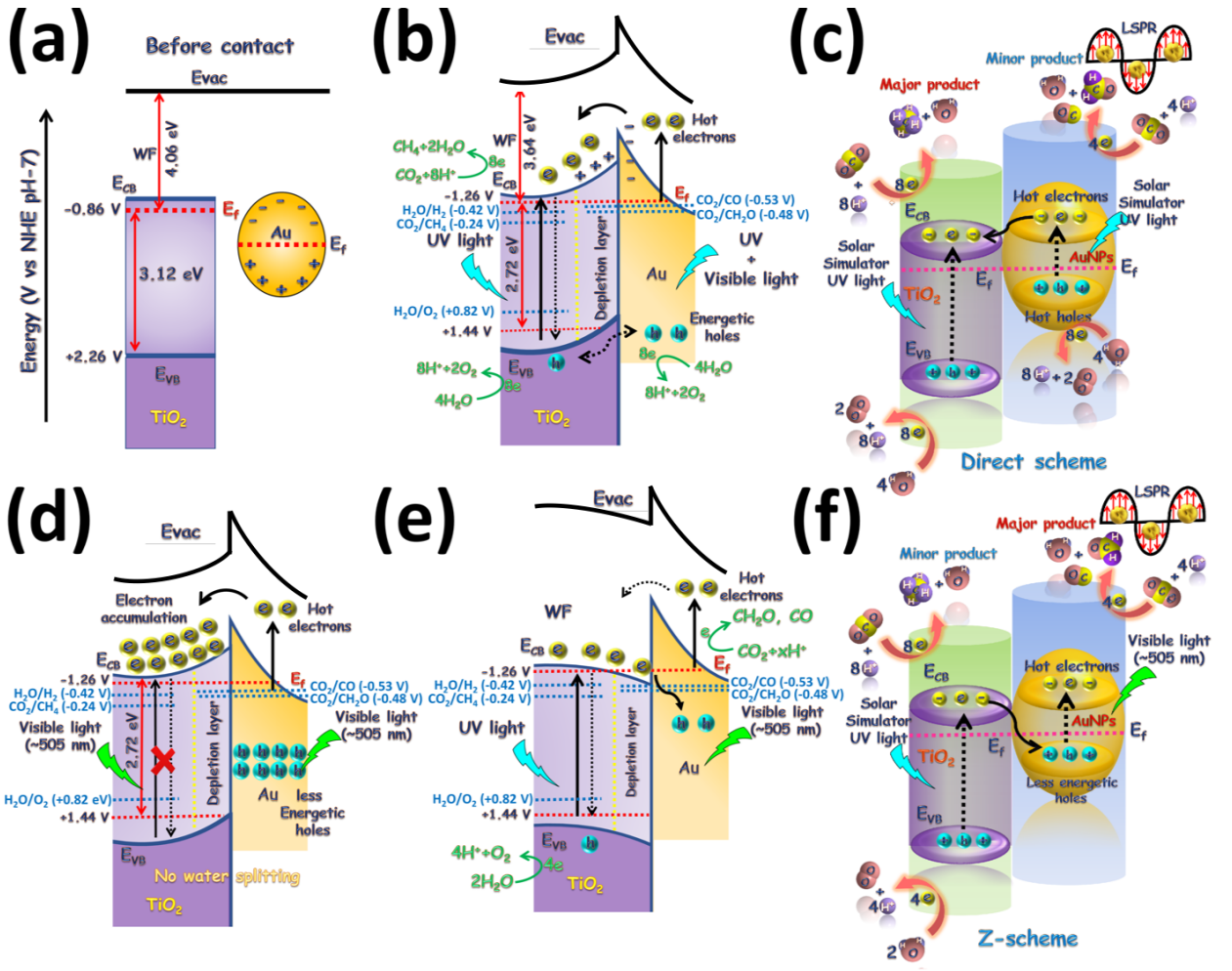

Figure 40: Proposed energy band diagram of Au-PMTiNT obtained from UPS WF and VB spectra. (a) Band energies before contact; (b) Formation of Schottky junction between Au and TiO_2 and reduction of CO_2 to methane; (c) Overall schematics of methane formation on Au-PMTiNT system under solar simulator; (d) The electron accumulation via SPR on Au under visible light; (e) Recombination of accumulated charge promotes Z-scheme; (f) Overall schematics of Z-scheme photocatalytic conversion.

5. Femtosecond and Picosecond Single Pulsed Laser Ablation of Nonlinear Optical TiN, as alternative for gold

Admitted that plasmonic photocatalysis offers the promise of using light as the energy source to drive a variety of thermal energy-intensive chemical reactions, the incorporation of plasmonic noble metals has become a double-edged sword. Researchers are eager to replace them due to their rare and expensive natures. The group IV transition metal nitrides have shown the possibilities as better alternatives courtesy of their unique characteristics such as exhibiting both metallic and semiconducting properties, possessing ceramic hardness, high thermal tolerance and chemical resistance, showing the possibility for substitution of plasmonic noble metal, etc [227-229]. Heretofore, TiN is the superior material that possess both ceramics property being refractory and plasmonic metal property showing high carrier concentration and high permittivity in long wavelength regime, which is considered as an promising alternative for gold in many practical applications. In this paper, the laser ablation threshold of TiN was investigated and compared with that of gold. The experimental results indicate that the prepared TiN-TNT sample is suitable and promising in many practical applications for example non-linear optical limiter and photothermal heating catalyst.

5.1. Experimental details

Fluorine-doped tin oxide (FTO) coated glass substrates were cut into 2 cm × 2.5 cm pieces. Afterwards, substrates were washed using soap water and sonicated by DI water, acetone, methanol for 10 min each. After being dried under nitrogen flow, FTO glass pieces were loaded in a DC magnetron sputter system (Kurt J. Lesker Co.) for Ti thin film deposition. The base pressure was 1mTorr, the power applied on Ti target was 300 W, and the duration of magnetron

sputtering was 40 min to get 300 nm thin film. A two-electrode electrochemical anodization process was applied on as-prepared Ti thin film as the working electrode and a graphite rod as the counter electrode at 40 V in an ethylene glycol (EG) based electrolyte (0.3wt% NH_4F, 4 vol% DI). The electrochemical anodization cell was placed in cold water bath during the anodization process, which normally took 5-7 min till the Ti coated film turned 80% translucent. After rinsing with DI water, as-prepared samples were loaded for plasma enhanced atomic layer deposition of 40 nm TiN thin film using $TiCl_4$ as the Ti precursor and a N_2/H_2 plasma as the N precursor. The Oxford ALD instrument substrate was heated to 200 ℃ and the deposition rate was 0.24 Angstrom per cycle. Afterwards, as-prepared samples were loaded in a three-zone furnace (STF55666C-1, Thermo Scientific Lindberg/Blue M), annealing at 450 ℃ with 4 hours ramping up from room temperature and additional 4h dwell. For comparison, Au thin film and Au coated TiO_2 nanotubes were prepared on FTO substrates as well. The preparation of TiO_2 nanotube substrates for Au coating was identical to the aforementioned fabrication process. All the gold coatings were deposited using the same DC magnetron sputter system at 1 mTorr, 75 W for 330 sec. As the deposition rate of sputtering system is 7.5 nm/min, the thickness of gold layer was 40 nm to match with TiN layer thickness. For simplicity, these three samples are represented by TiN@TNT, Au@TNT and Aufilm.

The experimental setup for laser damaged and non-linear optics transmission experiment is shown in Figure 41. Two different pulse durations 220 femtoseconds and 2.2 picoseconds are used to investigate material ablation threshold. Sample targets are mounted on a 3D motion stage with 200 nm resolution and irradiated at 0◦ angle of incidence. The beam is focused onto the sample using a 10x long working distance microscope objective giving a FWHM spot size of approximately 2.9 μm. A CCD camera and a lens with 70 cm focal length acting as a sample viewing system are

employed to ensure that the sample surface was at the focus of the irradiating beam. The green LED and beam splitter are used for the illumination of in field of view. The energy of laser pulse is controlled by a combination of a half-wave plate and a glan polarizer near the output of the laser. Further energy attenuation is achieved using Schott NG absorbing glass filters. A Spectra Physics Model 407A power meter with an accuracy of 8% and a photodiode is applied for cross-calibration and shot to shot energy measurements. The applied pulse energy is in the range from 0.8 μJ to 200 μJ. For multiple shot irradiation, a combination of fast electric shutter and delay generator is mounted in between the aperture and BS1 generate specific number of shots as required. An Oriel USB2000 commercial fiber-coupled spectrometer is mounted 7 mm after behind the sample to examine the transmitted laser spectrum and intensity level for nonlinear transmission measurement.

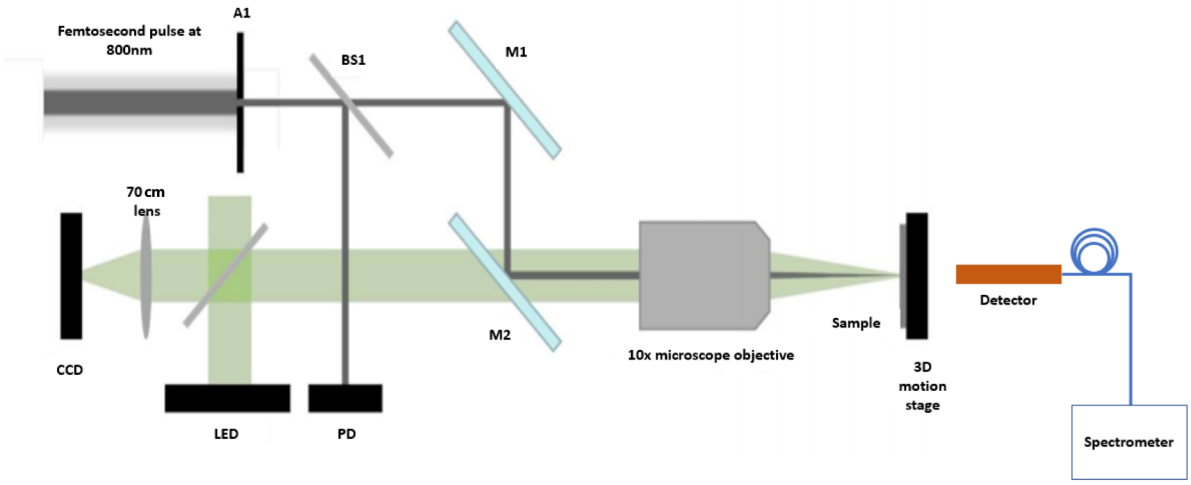

Figure 41:the schematic of the experimental layout. M1: dielectric mirrors coated for 800 nm 45◦ angle of incidence; BS1: Beam splitter: PD: photodiode; M2: aluminum mirror; L1: 70cm achromatic lens.

5.2. Result and Discussion

For a single pulse laser with Gaussian spatial distribution, Equation 13. was adapted to derive the ablation threshold.

$$D^2 = 2w_0^2 \ln\left(\frac{F}{F_{th}}\right) \quad (33.)$$

Where D is the diameter of the damaged crater area, w_0 is the $\frac{1}{e^2}$ gaussian beam radius, F is the fluence of the laser, and Fth is the ablation threshold. The fluence of laser is given as Equation 14, in which Ep is the pulse laser energy.

$$F = \frac{2E_p}{\pi w_0^2} \quad (34.)$$

FESEM was used to inspect and record the ablation diameters. As evidence of laser ablation, when the laser power exceeds the surface ablation threshold of the material, a visual darkening can be observed on the surface which is a damaged spot by the laser irradiation (Figure 42 (a) - (c)). Furthermore, as shown in Figure 43 (a)-(b), the diameter of the ablation crater area reduced gradually along with the decrease of laser power until the crater spots fully disappeared when the laser power was below the ablation threshold of the material. The crater diameters and their

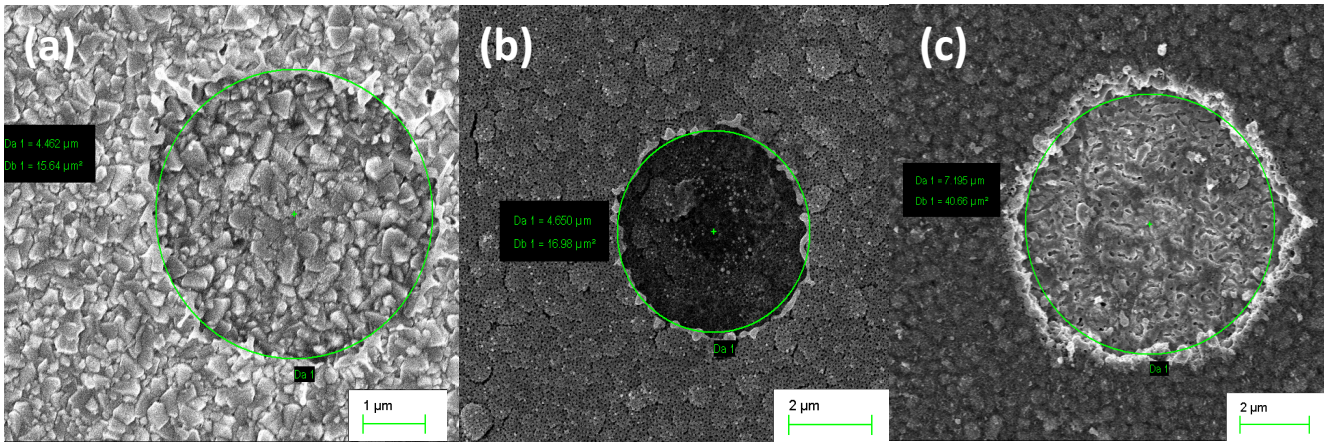

Figure 42: FESEM top view images, three zoom-in images of damaged spots from (a) Aufilm; (b) Au@TNT; (c) TiN@TNT.

corresponding laser fluences are indicated in Figure 44 (a) - (c) for TiN@TNT, Au@TNT, and gold thin film, respectively. The material-dependent ablation threshold can be obtained using a linear fitting curve which extend to $D^2=0$. It is obvious from the figure that TiN showed significantly higher tolerance compared to gold for both femtosecond laser and picosecond laser irradiations.

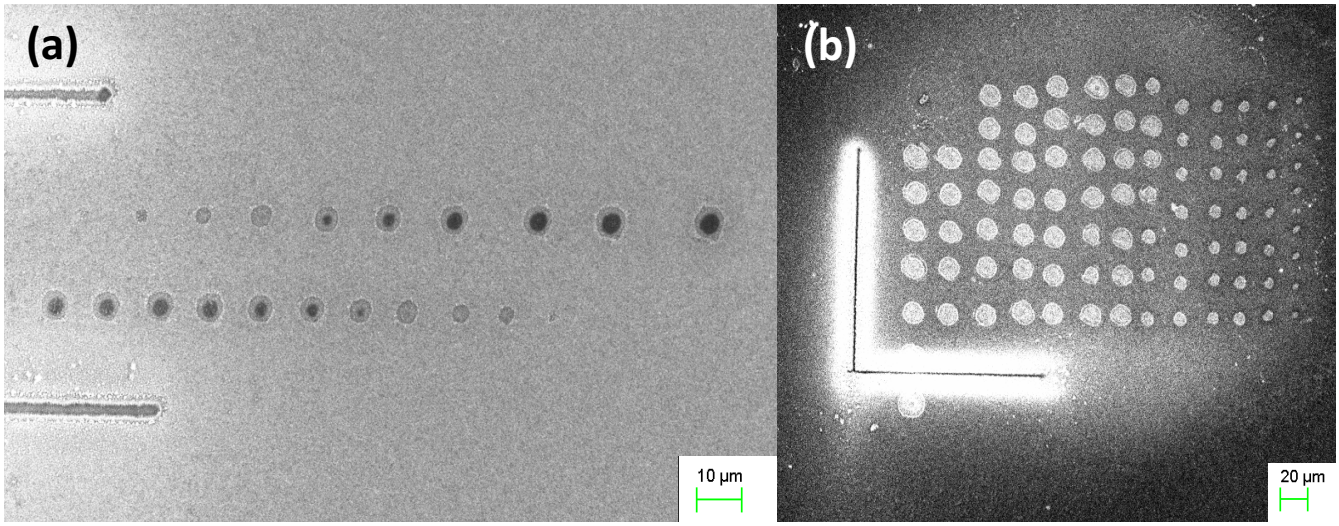

Figure 43: FESEM top view images (a) and (b) zoom-out image of laser ablation arrays of Au thin film and TiN@TNT samples.

Figure 44 (a) was plotted from the experimental data of 40 nm atomic layer deposited TiN on TiO_2 nanotube arrays, in which F_{th} is 1.520J/cm^2 under femtosecond laser irradiation and F_{th} is 1.733J/cm^2 under picosecond laser irradiation. On the other hand, the ablation threshold for picosecond and femtosecond laser from Au thin film and Au@TNT were 0.172 J/cm^2, 0.150 J/cm^2, 0.147 J/cm^2, 0.112 J/cm^2, respectively. It is worth noting that the high laser ablation threshold of TiN@TNT was intrinsically decided by the material property. We also notice that our TiN@TNT threshold is higher than that of some previous TiN reports from Bonse et al.[230], which can be attributed to two reasons as follows: first, the sample transmission is higher due to its nanotube morphology; second, the sample should be consider as TiN@TNT composite, although the chance of light and TiO_2 interaction is low considering the light penetration of TiN is normally about 23nm at 800nm wavelength irradiation[231].

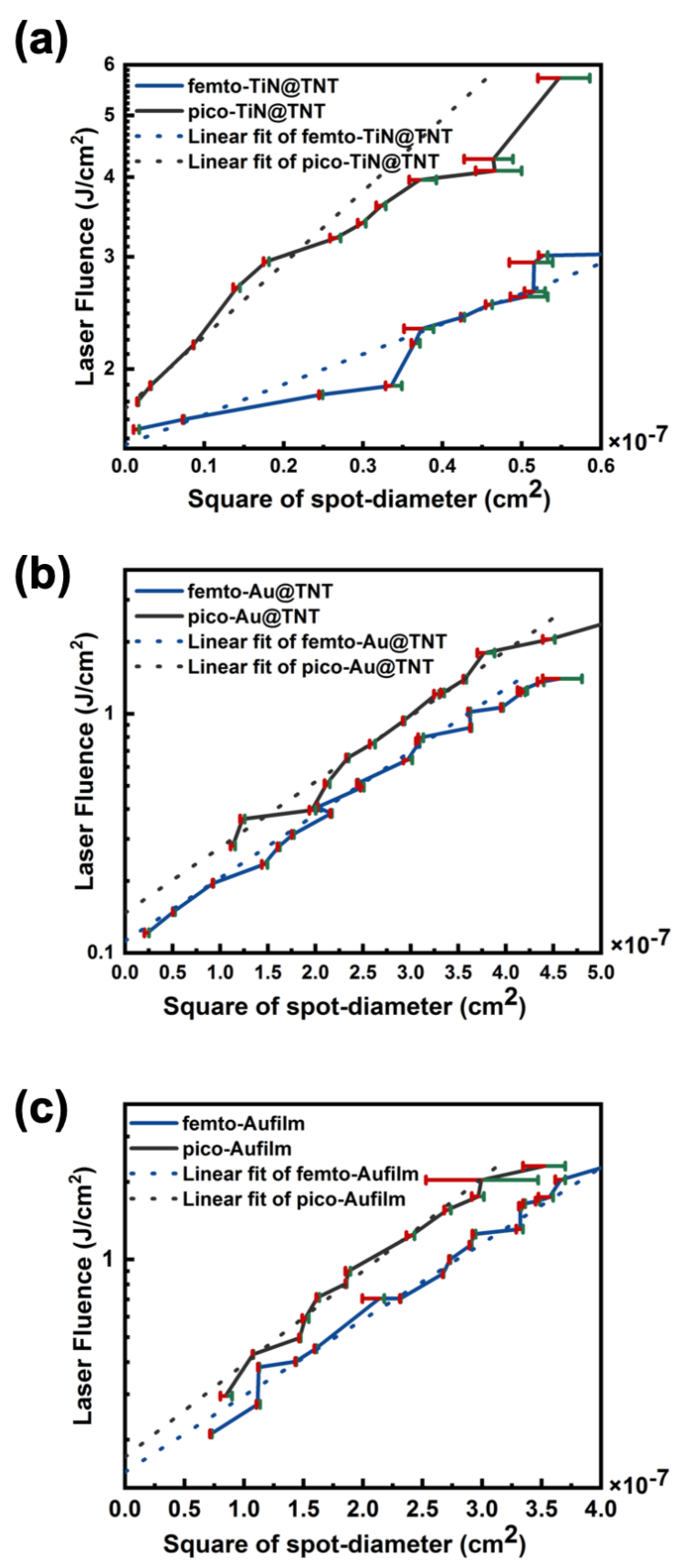

Figure 44：Experimental data plots with error bars for femtosecond and picosecond laser fluence vs. damaged diameter square: (A)TiN@TNT, (B)Au@TNT, and (C)Au thin film.

Another interest aspect is the effect of morphology on ablation threshold regardless of what type of material. Two type of morphologies were developed for comparison: (1) 40 nm of materials coating on TiO_2 nanotube arrays to create highly porous nanostructure; (2) 40 nm of materials as thin film. The experimental results are in line with the expectations from published reports. We observed slightly higher ablation efficiency with nanostructured gold compared to thin film gold. And there are reasons that we can think of for lower laser ablation efficiency: (1) better light trapping within nanotube structures; (2) thermal confinement due to porous structures. The dielectric contrast between the TiN or Au coated nanotubes and the air gaps allows light trapping within the tubular structure, apparently resulting in more effective energy conversion compared to light that is strongly reflected back at the thin film surface. This means that with the same laser power, the sample with better light trapping can reach higher temperature. Furthermore, the nanostructured samples were porous and the pore were filled with air which has poor thermal conductivity approximately 0.026 W/m/K according to literature[232]. On the other hand, the thermal conductivities for continues gold and titanium nitride are 310 W/m/K and 28.84 W/m/K, respectively. Although the thermal transfer is not significant in the scale of our laser pulse duration, it is still reported in previous research that gold can complete electron-lattice thermal equilibration within picoseconds[233]. In other words, when a laser beam incident on a highly thermal conductive material, for example thin film gold in this case, the thermal energy immediately spread out in the scale of picosecond instead of causing ablation. So, we should still take thermal diffusion into consideration as it is also proved later in the simulation.

This nanostructure introduced optical and thermal confinement is practical and has advantages for certain applications. To verify these two suppositions, Lumerical FDTD and HEAT simulations were conducted to analysis light propagation and thermal conduction.

In additional to the differences in materials' property and morphology. the pulse duration of laser also has a significant impact on the ablation threshold. According to the experimental data, we observed slightly higher threshold under picosecond laser irradiation compared to femtosecond laser irradiation, which means the ablation efficiency decreased with the increase of pulse laser duration. The results are listed in the Table 4:

Table 4：The ablation thresholds for three different samples under femtosecond laser and picosecond laser irradiation.

Samples / Ablation threshold （J/cm^2）	TiN@TNT	Au@TNT	Au thin film
Femtosecond laser	1.520	0.112	0.150
Picosecond laser	1.733	0.147	0.172

The reason for this has been explained comprehensively by Chichkov et al [234]. The interaction of femtosecond laser pulse with materials can be described in three sequential stages. It starts from laser energy absorption through photon-electron coupling within the time frame of femtoseconds, which heat up the electrons without disturb the lattice. Then the next stage is in the time frame of picoseconds, named electron-phonon coupling, in which the hot electron transfers thermal energy to lattice and reach an equilibrium temperature. The last stage is phonon-phonon coupling processing which is also known as energy diffusion. As we mentioned earlier, femtosecond laser ablation is a non-thermal process, while picosecond laser ablation is a thermal process, in which the heat conduction loss is inevitable. However, the mass transport process also needs to be taken into consideration. Because remove a material by laser irradiation is still a hydrodynamic process which is normally longer than the thermal process. Taken together, the threshold for ultrashort

laser ablation is generally smaller than long duration laser ablation due to less heat loss effect, but not by much because it is also limited by the mass transport process.

TiN@TNT sample was tested for nonlinear optical limiting performance and the data is show in Figure 45. The sample was measured up to 6 J/cm^2. The nonlinear transmission is easily observed from the curve, starting at 1.2 J/cm^2 with a distinct reduction in transmission, then gradually slowing the slope with the increase of fluence, and finally becoming flat after reaching the ablation threshold. The transmission value started from 64% at 1.2 J/cm^2 to 9.5% at 6 J/cm^2. Additionally, according to the ablation threshold of the sample, the curve can be separated into two segments which are below-threshold power and above-threshold power. From 1.2 J/cm^2 to 1.5 J/cm^2, the drastically decrease of transmission can be ascribed to two-photon absorption due to increasing irradiation power intensity especially when the laser pulse duration is in femtoseconds. After the incident power is above material threshold, the low transmission is a result of optical induced ablation. The obvious nonlinear transmission behavior is benefited from strong Mie scattering and high concentration of excitonic and free electrons.

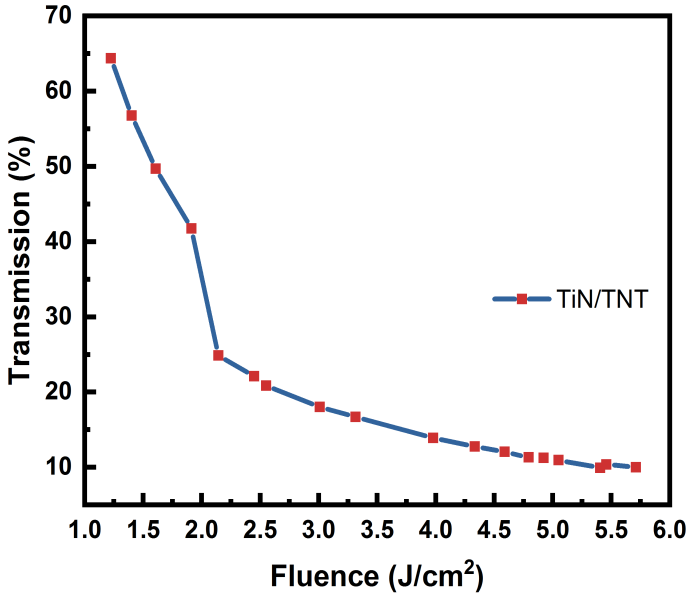

Figure 45: Transmission vs. fluence spectrum indicated strong nonlinear optical limiting effect on TiN@TNT sample.

5.3. Simulations of light interaction and heat distribution:

Lumerical FDTD and HEAT simulations were employed to further analysis the light interaction and heat distribution across the samples. The experimental and simulated absorbance spectra of Au and TiN is shown in Figure 46 and its inset. In spite of small different in absorbance intensity due to the adopted references, the simulated absorbance spectra matched well with those of the actual samples, which proved our optical simulations were valid. Absorbance spectra evident that TiN@TNT and Au@TNT have very similar absorption spectra except that the absorbance intensity is different.

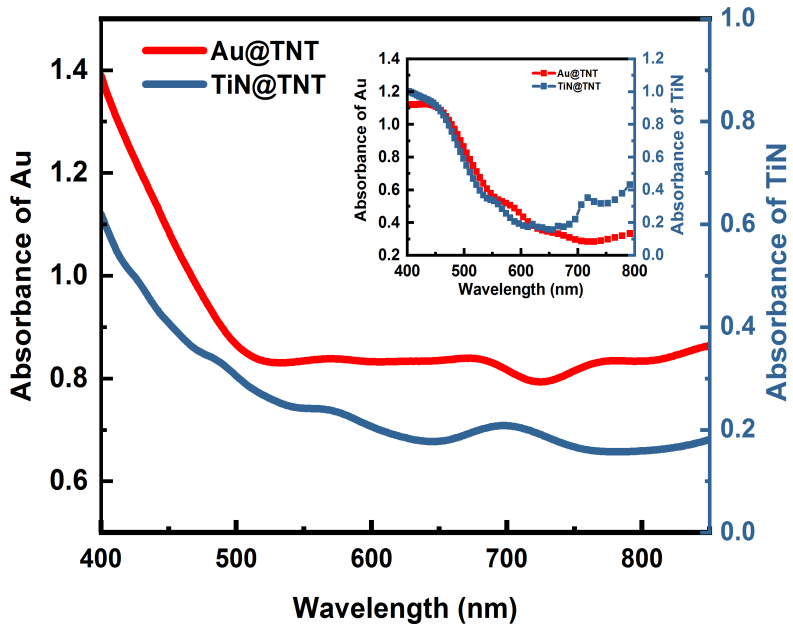

Figure 46: The experimental absorbance spectra of Au@TNT and TiN@TNT and simulation from Lumerical FDTD (inset).

Figure 47 (a)-(c) are Poynting vector plots for Au thin film, Au@TNT, and TiN@TNT, respectively. To be specific, in the presence of nanostructures, hot spots appeared in the inner and outer tubular structure, and especially where the nanotubes are adjacent. On the other hand, the planar gold sample could not find any hot spots except at the sharp corners of the substrate.

However, it is not the case in reality as the size of substrate is much larger than the size of laser beam, so no sharp corners are involved. To summarize, in a Poynting vector plot, hot spots represent areas with high local electric fields that are particularly beneficial for laser ablation due to strong light interaction.

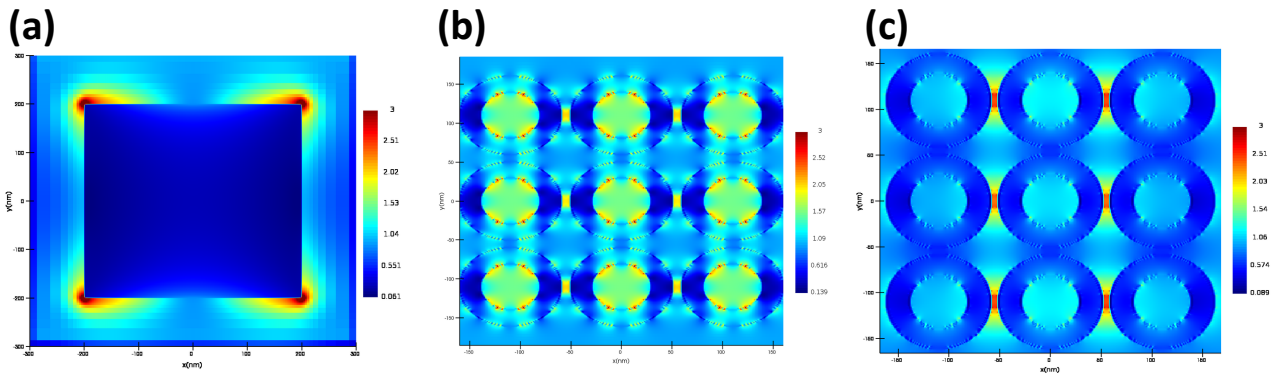

Figure 47: Poynting vector plots: (A) Au thin film, (B) Au@TNT, and (C) TiN@TNT.

In addition to light interaction, heat distribution is also a role of interest for this study. Therefore, the heat distribution maps were simulated for each sample by Lumerical HEAT. As shown in Figure 48, the color gradient of the heat distributions of Au thin film, Au@TNT, and TiN@TNT in the side view and top view were demonstrated. An import heat source is used to import the optical absorption data saved by FDTD to be used as heat input to the simulation. The maximum temperature of Au thin film was 345K, Au@TNT was 426K, and TiN@TNT reached 925K. The thermal transfer in gold is typically on the order of sub-nanometer per picosecond, hence it was difficult to present the temperature deviations quantitatively. However, we could readily observe the trends for the hot spots and heat loss in the color gradient schemes. By comparison, the thermal distribution patterns are significantly different from Au thin film to the nanotube arrays. The thermal diffusion of Au thin film clearly starts from the center to the edge, while nanotube arrays are relatively uniform across the scope. Such high thermal conductivity under short laser pulses

results from high electron temperature and ultrashort collision rate of high energy electrons.In this project, the investigation of TiN-TNT infrared laser ablation threshold and its photothermal effect are valuable and enlighten to future works. Photothermal effect represents the conversion of

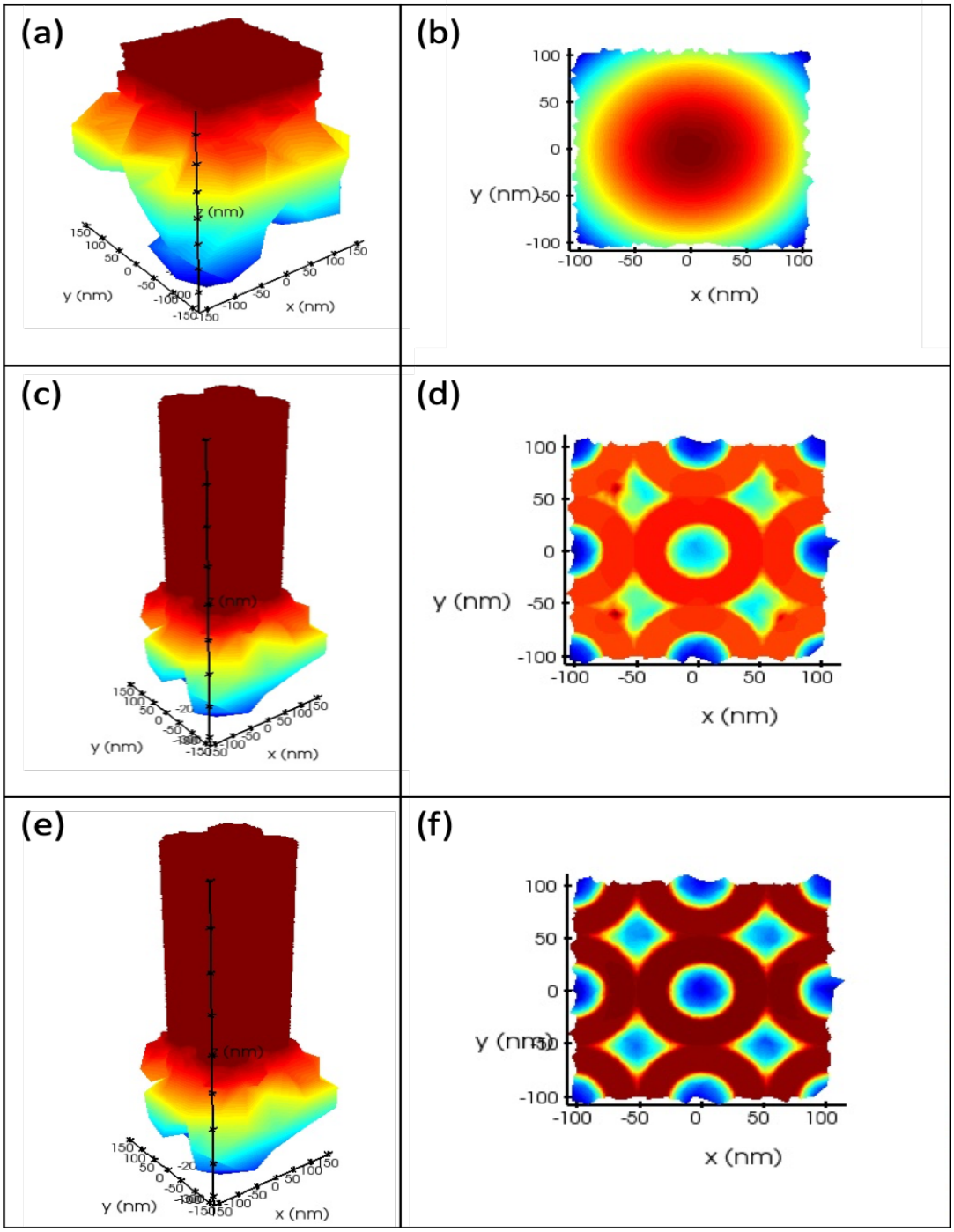

Figure 48: Side and top view of thermal distribution for: (A) and (B) Au thin film, (C) and (D) Au@TNT, (E) and (F) TiN@TNT.

photon energy to thermal energy which is discovered by scientist for long time. Now it becomes increasingly popular due to its application in biotherapy[203], water evaporation and desalination[235], hydrogen evolution[236] and CO oxidation[237]. Gold has always been the benchmark for photothermal applications. Normally the photothermal transduction efficiency is in the range of 20%-65% for gold[238]. However, thermoplasmonics surpasses traditional photothermal heating in terms of efficiency which is highly achievable using TiN-TNT. Taken obtained experimental and simulation results into consideration, TiN-TNT would be the ideal photocatalyst because it has many superior advantages comparing to gold, such as cheap, abundant, strongly light interactive, plasmonic, highly thermal tolerant. Additionally, we have proved that it possesses high laser ablation threshold and high photothermal efficiency.

5.4. Conclusion

In summary, the ablation thresholds of TiN@TNT, Au@TNT, and Au thin film were determined under femtosecond and picosecond laser irradiation in detailed comparison. The experimental data manifested that unprecedented performance of TiN@TNT providing higher ablation resistance and less heat loss. The ablation thresholds for femtosecond and picosecond laser irradiation were 1.52 J/cm^2 and 1.73J/cm^2, respectively, which are more than one order of magnitude higher than those of Au thin film and Au@TNT. Admitted that the material property is decisive for ablation tolerance, the laser pulse duration and surface topography of sample also have impact on the threshold value. Further analysis demonstrated that femtosecond laser ablation tends to be more efficient due to the nature of non-thermal process, whereas in picosecond laser ablation, it involves heat loss resulting in lower efficiency. In addition to that, the effect of surface topography was investigated in this study, showing that the presence of nanostructures obtained strong light

interaction and confined heat transfer. Last but not least, the proof of strong nonlinear optical property opens a window to practical optical applications for TiN such as optical limiter, optical sensor and so forth.

6. Core-Shell TiO_2@HfN Nanotube Arrays: Hot Carrier Photoanode for Sunlight-Driven Water-Splitting

6.1. Background and motivation

Among all the transition metal nitrides hafnium nitride is basically unexplored and rarely utilized in optoelectronic devices. There are many reports investigating approaches to synthesize high quality HfN. Some are interested in employing HfN as hot carrier absorber since its wide phonon gap can slow down the carrier thermalization process. Saha et al. calculated its electronic structure indicating its unique phonon dispersion of acoustic and optical branches [239]. Based on this feature, Chung et al. proposed using HfN for hot carrier solar cell and obtained a decay time of 1.7 ns in a transient absorption spectroscopic measurement [240]. The one and only catalytic application report was from Chiara et al., in which HfN nanoparticles were used for electrocatalytic oxygen evolution and the highest performance was 10 $mAcm^{-2}$ at an overpotential of 358 mV [241]. Another similar work was presented by Yang et al. reporting electrocatalytic hydrogen evolution using nitrogen-plasma treated hafnium oxyhydroxide [242]. Based on the findings from pioneer studies, HfN is worth investigating as a photocatalyst for solar energy conversion due to the following reasons: 1) High thermal and chemical resistance, and photochemical stability under harsh conditions 2) Long hot carrier lifetime 3) Plasmon resonance in the Vis-NIR regime 4) Cost efficient alternative to noble metals. Despite the aforementioned properties that are particularly beneficial to photocatalytic energy conversion, no one has reported successful utilization of HfN for any kind of photocatalytic reactions.

6.2. Experimental Section

TiO_2 nanotube array synthesis: The fluorine doped tin oxide (FTO) coated glasses were first washed by soap water and then ultrasonicated in deionized water, acetone, and methanol sequentially for 10 min each. After being dried under a nitrogen stream, the top 3 mm of substrates were covered with Kapton tape, which was done to keep a FTO exposed area for contact in later experiments. The substrates were then loaded into a direct current magnetron sputtering system. The sputtering chamber was first evacuated to 10^{-6} Torr and later filled with argon to achieve a working pressure of 1 mTorr. A Ti target with 99.99% purity was used to deposit 500 nm on the substrates at room temperature**.** After deposition, the substrates were cut into 2.5 cm × 3 cm pieces with edges protected by Kapton tape to limited high currents at edges and corners during the electrochemical anodization process. The samples were anodized at 40 V in a mixed ethylene glycol-based electrolyte containing 0.3 wt% NH_4F and 4 v% deionized water. The electrochemical anodization was conducted in a two-electrode cell using the as-prepared sample as working electrode and a 6 mm diameter graphite rod as counter electrode with a 3 cm distance between anode and cathode. The anodization process took around 10 min until the current began to rise and the substrate turned semi-translucent from metallic dark. After the anodization completed, the samples were rinsed with methanol and dried under nitrogen flow. To remove debris formed on the top of the TiO_2 nanotubes, a dry etching process was applied on synthesized samples using an Oxford PlasmaPro NGP80 Reactive Ion Etcher with SF_6 as working gas at 20 mTorr and forward power of 250 W for 200 seconds, and followed by O_2 plasma at 150mTorr and forward power of 225 W for 10 min. As-prepared samples were annealed in a three-zone

tube furnace (STF55666C-1, Thermo Scientific Lindberg/Blue M), in which the temperature increased to 450 in 4 h and the dwell time was another 4 h.

ALD deposition of hafnium nitride: HfN films were grown using plasma enhanced atomic layer deposition (PE-ALD) technique in a continuous flow ALD system (ALD150-LX, Kurt J. Lesker) at 1.01 Torr reactor pressure. Tetrakis(dimethylamino)hafnium (TDMAHf) and forming gas (FG: 5% H_2 + 95% N_2) remote inductively coupled plasma (13.56 MHz ICP, 0.6 kW, 60 sccm FG with 100 sccm Ar carrier) were the Hf-precursor and N-source respectively. Process conditions for self-limiting HfN PEALD were characterized with in-situ spectroscopic ellipsometry measurements (M2000DI, J. A. Woollam). Using growth-per-cycle (GPC) determined on a planar Si (111) substrate for PEALD cycle: 0.1s TDMAHf pulse, 12s post-precursor purge, 9s FG plasma exposure, and 5s post-plasma purge, 20 nm thick HfN film was grown on TiO_2 nanotube array structures in 300 cycles.

Photoelectrochemical water splitting measurement: The measurement of photoelectrochemical water splitting was performed in a three-electrode system consisting of as-prepared sample photoanode, Pt cathode, and Ag/AgCl reference electrode, in KOH electrolyte. A Newport Oriel solar simulator with Class A output was used to generate simulated solar light (AM 1.5G) and the power density upon the sample surface was 100 mW/cm^2. In order to measure the photocurrent response under visible light illumination, the simulated sun light (AM 1.5G) was filtered by a UV cut-off filter (λ > 420 nm). The photocurrent was obtained under linear sweep voltammetry mode and the sweeping voltage was from -0.8V to +1.0 V versus Ag/AgCl. To investigate the photocurrent response of the sample at discrete wavelengths, near-monochromatic light LEDs

were used to illuminate the sample at the power density of 10 mW/cm^2. The photocurrent response currents were collected at constant potential of 0.3 V vs. Ag/AgCl.

6.3. Results and discussion

With this aim, a photoanode consisting of TiO_2(core)-HfN(shell) nanotube arrays (HfN-TNT) was deployed in photoelectrochemical water splitting and achieved a champion photocurrent of 2.48 mAcm^{-2} under 1 Sun illumination (AM 1.5G) at an applied bias of +0.6 V vs Ag/AgCl reference electrode in 1 M KOH solution. A photocurrent response of 2.39 mAcm^{-2} during light on-off cycling was measured under identical conditions. To the best of our knowledge, this performance is superior to most plasmonic noble metal decorated TiO_2 based catalysts. The TiO_2 nanotube array (core) was grown by electrochemical anodization of a Ti film sputtered at room temperature on a non-native fluorine doped tin oxide (FTO) coated glass substrate [243-245]. The conformal HfN shell layer was formed by plasma-enhanced atomic layer deposition, which is a facile technique to form conductive transition metal nitride coatings of good structural and stoichiometric quality [246-248]. The catalyst is economically efficient and suitable for large scale production due to the scalability and existing industrial usage of electrochemical anodization and atomic layer deposition.

Further details of the photoelectrochemical measurements are provided in the Methods section. A baseline was measured without any illumination, in which we observed almost zero photocurrent density. The J-V characteristics of HfN-TNT (shown in Figure 49 and 50) were collected in the dark and under AM 1.5 G 1 sun illumination without, and with a UV filter in 1 M KOH solution. The highest photocurrents (shown in Figure 49) are 2.48

mAcm^{-2} under 1 Sun illumination (AM 1.5G) and 1.8 mAcm^{-2} after adding a UV filter (>420 nm) at an applied bias of +0.6 V vs Ag/AgCl. The data collected under light On-Off mode is shown in Figure 50, in which the photocurrents are 2.39 mAcm^{-2} and 1.74 mAcm^{-2} without and with UV filter, respectively. To understand the spectral composition of the generated photocurrent, a set of near-monochromatic LEDs were used to illuminate the sample (Figure 51 (a) and (b)) for testing that were conducted in 0.1 M KOH electrolyte and, unless otherwise stated, the photocurrents were at a bias of +0.6 V versus Ag/AgCl. We observed a photocurrent response that extended all the way to 730 nm wavelength illumination, which is quite unusual in the field of sunlight-driven water-splitting. 730 nm photons have an energy of 1.7 eV which is merely 0.47 eV above the minimum energy required for water electrolysis. It is important to understand how the performance of the HfN-TNT photoanodes stands in comparison to plasmonic noble metal sensitized metal

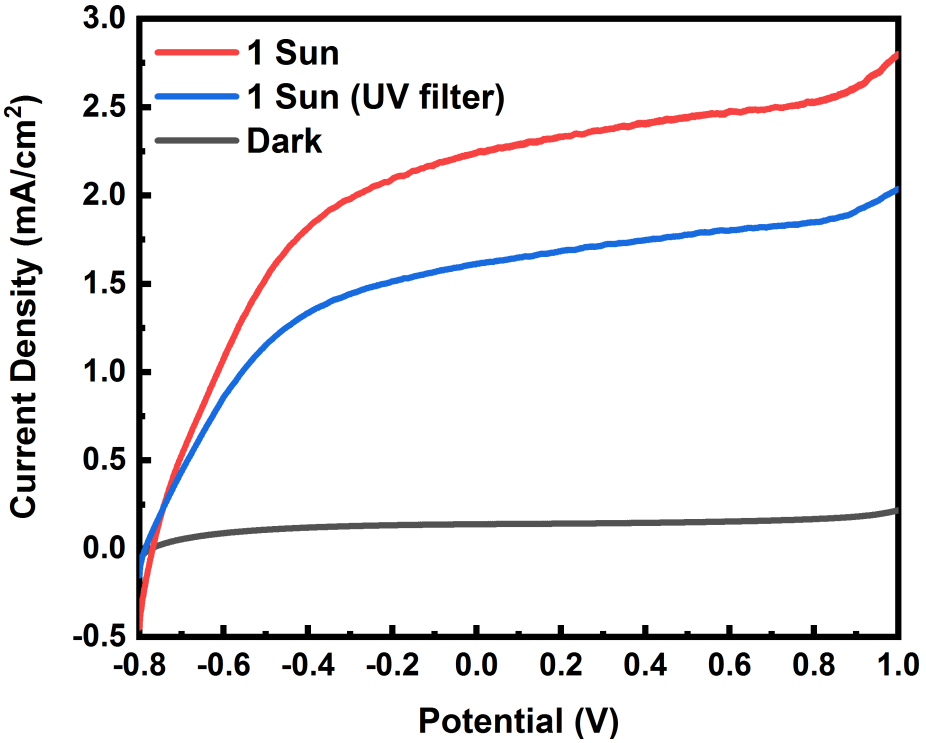

Figure 49: Photocurrent measured by linear sweep voltammetry under AM 1.5 G illumination with and without UV cut-off filter (> 420 nm).

oxide photoanodes they seek to replace. Table 5 is a performance summary of the photoelectrochemical performance under visible light illumination of TiO_2 based photoanodes which derived an enhancement of photoactivity in the visible regime after decoration by nanoparticles or coatings of plasmonic noble metals namely Ag and Au. Table 5 shows that harvesting of visible light using hot carriers by previously reported noble metal-TiO_2 nanostructured plasmonic heterojunctions is able to generate no more than 224 μAcm^{-2} in photocurrent. Such a poor performance is not entirely surprising since it is well-understood that the ultrafast timescale (< 10 ps) of electron-electron scattering and electron-phonon scattering render it extremely hard to drive chemical reactions using hot carriers before their thermal equilibration. In contrast, our unoptimized HfN-TNT photoanode is able to generate 1.8 $mAcm^{-2}$ under identical conditions as shown in Table 5 indicating a potentially superior hot carrier harvesting ability.

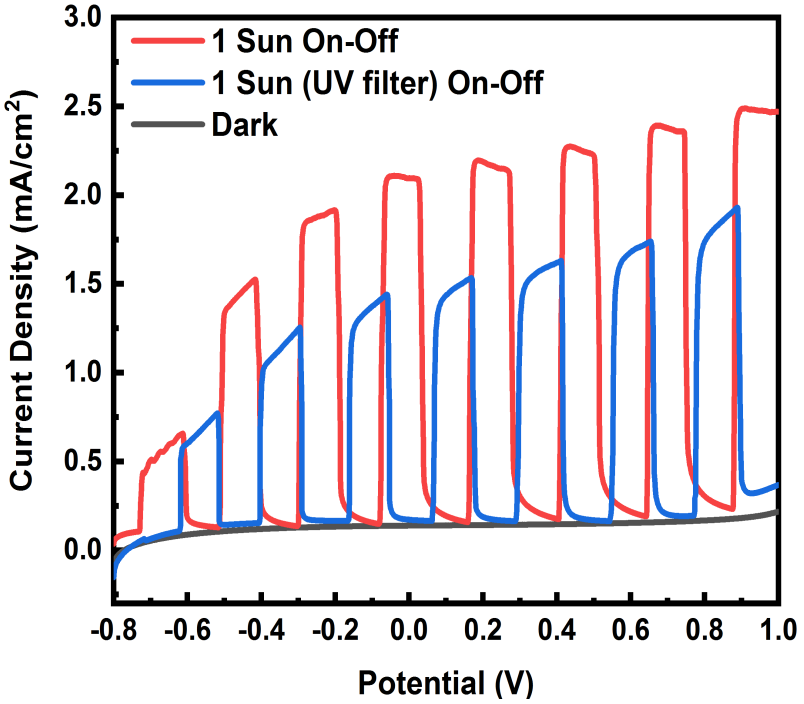

Figure 50: Photocurrent response during light On-Off cycles, measured by linear sweep voltammetry under AM 1.5G illumination with and without UV cut-off filter (> 420 nm).

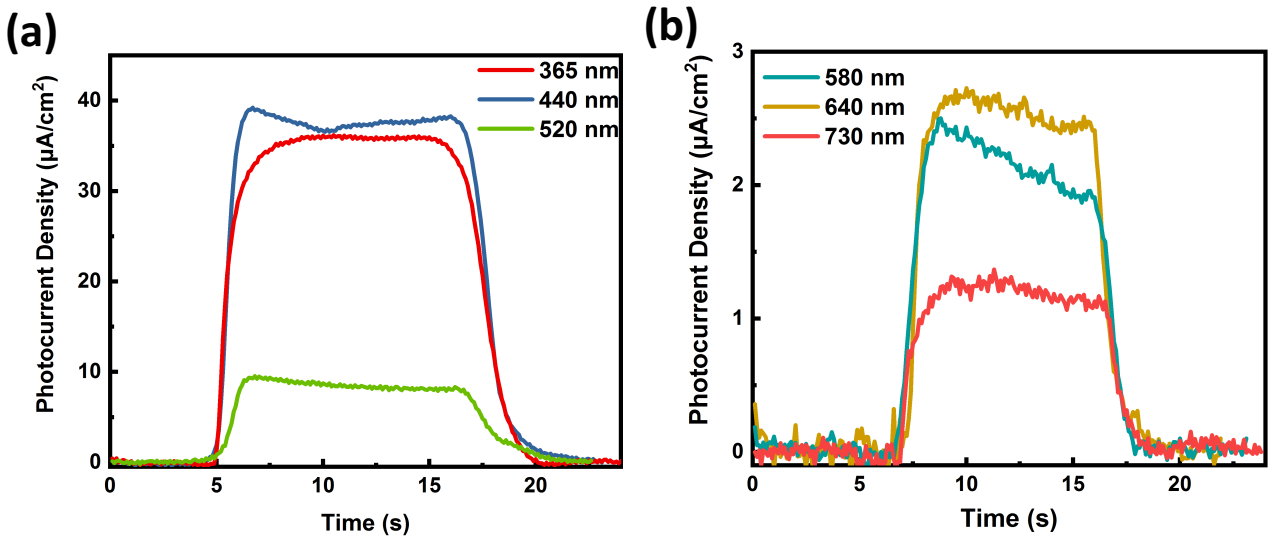

Figure 51: Photocurrent density plots: (a) and (b) Amperometric I-t curves showing photocurrent response under the illumination of near-monochromatic LEDs above at 0.3 V vs. Ag/AgCl.

Table 5: A summary of performance using plasmonic noble metal decorated TiO_2 based catalysts for PEC water splitting under visible light illumination.

Sample	Photocurrent ($\mu A/cm^2$)	Light intensity (mW/cm^2)	Light spectrum	Applied bias	Electrolyte	Reference
HfN-TNT	1800	100	visible light (>420 nm)	0.6V	1M KOH	This work
Ag/N-TiO_2	26	120	visible light (>420 nm)	0V	0.5M Na_2SO_4	[249]
AgNPs/TiO_2 NWs	47	100	visible light (>420 nm)	0.4V	0.1M Na_2SO_4	[250]
In situ AgNPs/TNTs	40	80	visible light (>420 nm)	0.3V	0.1M Na_2SO_4	[251]
Ag/N-TiO_2	0.5	500	400-900nm	0.3V	1M KOH	[252]

Au/RGO/H-TNTs	224	100	visible light (>400 nm)	0.2V	1M KOH	[253]
LE-Au/TNTs	202	100	visible light (>400 nm)	0.2V	1M KOH	[254]
AuNPs/TiO_2	23	7000	532nm, 633nm	0V	1M KOH	[255]
Au embedded TiO_2	3		visible light (>420 nm)	0.2V	1M KOH 25% MeOH	[256]
AuNPs/TiO_2 BNRs	125	100	visible light (>420 nm)	0.5V	1M KOH	[257]
AuNPs/TiO_2 NWs	11	73.3	visible light (>430 nm)	0V	1M KOH	[258]
AuNPs/TiO_2 PhC	150	100	visible light (>420 nm)	0.2V	1M KOH	[94]

The morphologies were examined before and after HfN coating using a Zeiss Sigma field emission scanning electron microscope (FESEM). The outer diameter of nanotubes is 80-100 nm while the inner diameter is 30-50 nm (Figure 52 (a)). After HfN atomic layer

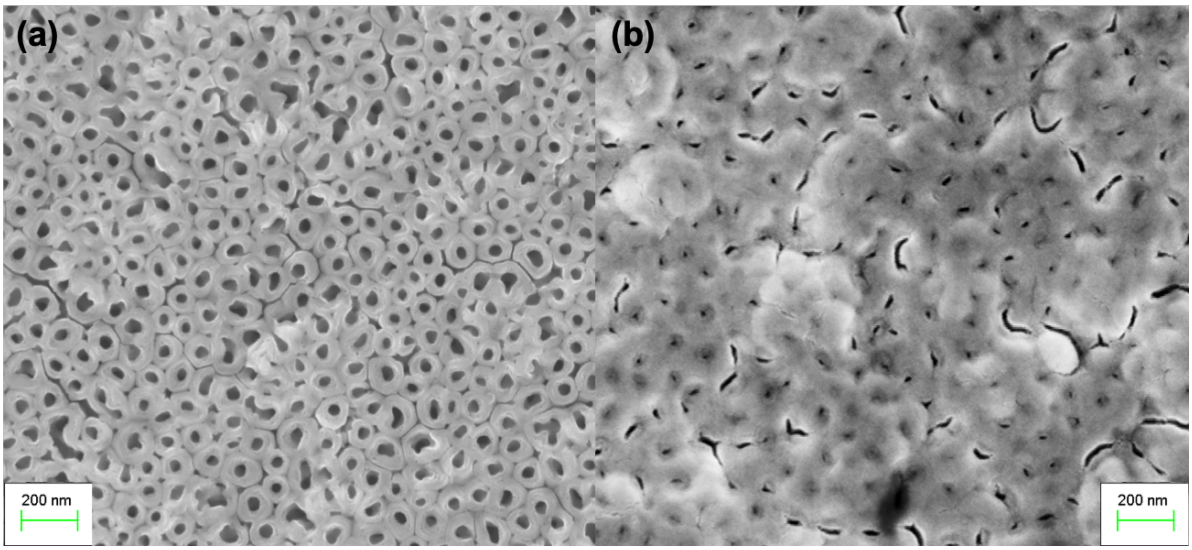

Figure 52：FESEM images of TiO_2 nanotube arrays (a) before and (b)after ALD HfN coating.

deposition (ALD), the mouths of nanotubes are almost closed and the space between nanotubes is filled (Figure 52 (b)). The high-resolution transmission microscopy (HRTEM) image (Figure 53) shows the tubular structure with double layers. The TiO_2 core is slightly brighter than the HfN shell which is darker. Figure 54 shows the lattice fringes at the interface of core and shell with 0.358 nm and 0.256 nm interplanar d-spacing, corresponding to anatase TiO_2 (101) and HfN (111), respectively.

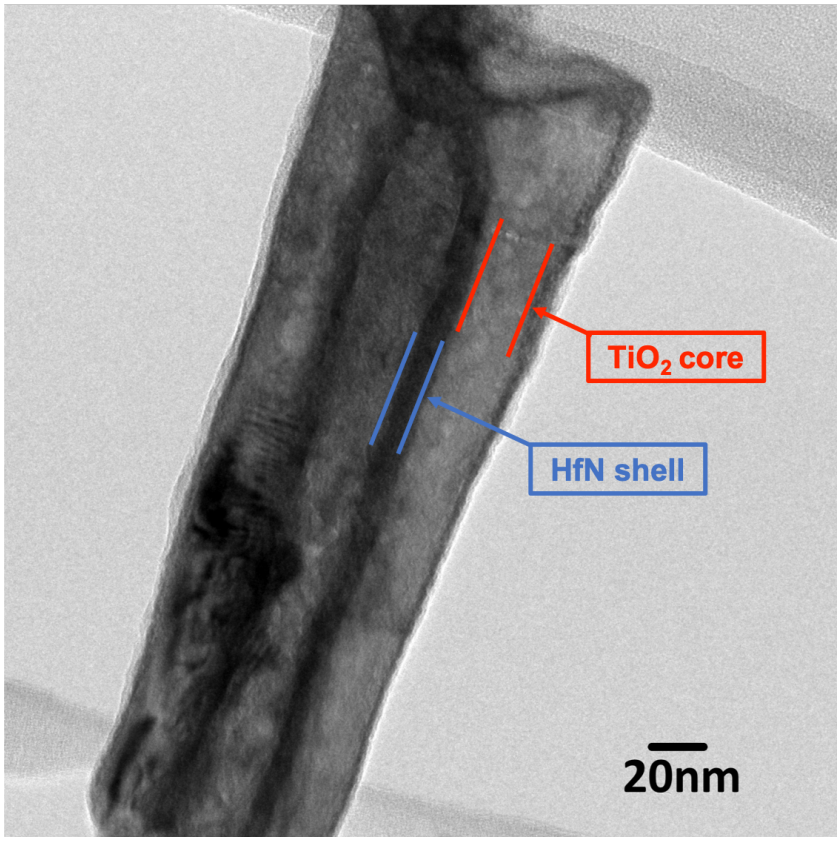

Figure 53：HRTEM cross-section view image demonstrates the two layers constituting the core-shell nanotube morphology.

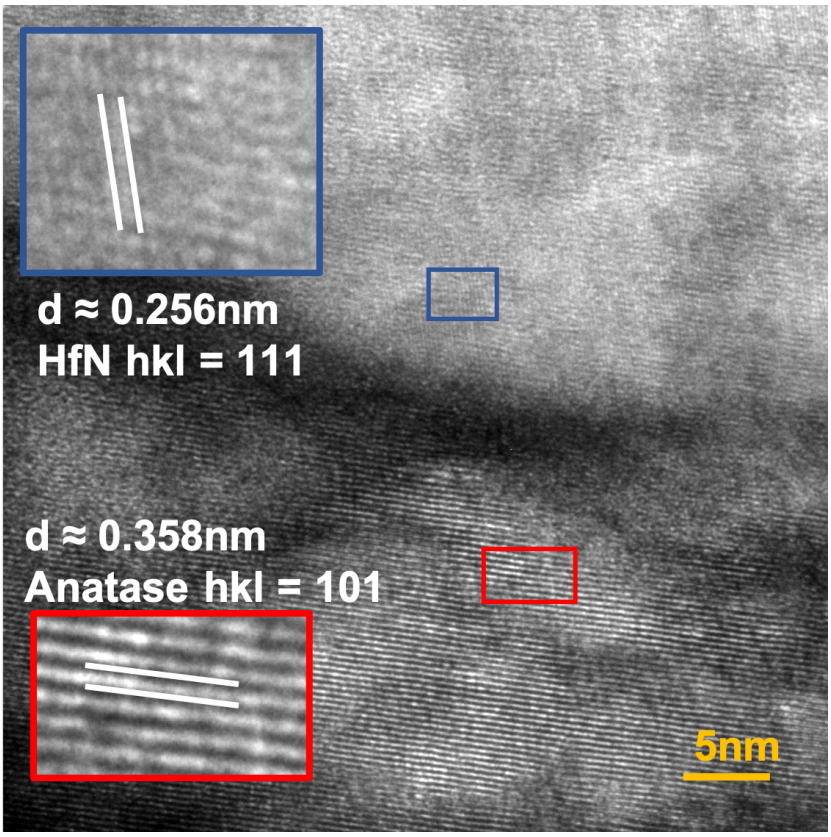

Figure 54: HRTEM image at the HfN and TiO_2 interface showing anatase TiO_2 (101) lattice fringes and HfN (111) lattice fringes.

The phonon dispersion in HfN makes it an outstanding candidate for hot carrier mediated photocatalysis. The constituent Hf and N atoms have a great difference in mass resulting in a large phonon gap between the optical and acoustic modes. In the Raman spectrum of HfN-TNT sample (Figure 55), the dominant four peaks are at 144 cm^{-1} (Eg), 399 cm^{-1} (B1g), 515 cm^{-1} (A1g and B1g), and 639 cm^{-1} (Eg) from anatase TiO_2. Further investigation focused on HfN phonon dispersion. Although there are some peaks that do not stand out from TiO_2 peaks, the signature Raman peaks for HfN phonon distribution are still noticeable. The peak representing the HfN transverse acoustic phonon mode is submerged in the TiO_2 Eg band at 140 cm^{-1}. Nevertheless, another signature peak for longitudinal acoustic phonons in the first order acoustic band is observable at 199 cm^{-1} in the spectrum.

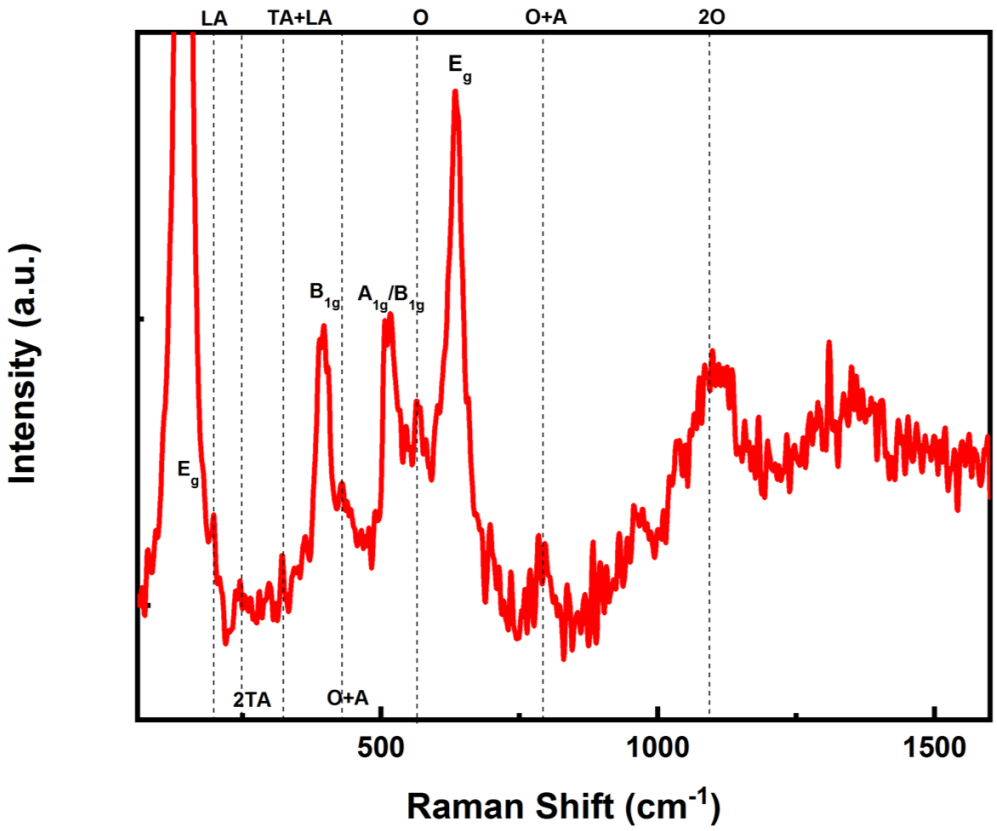

Figure 55：Raman spectrum of HfN-TNT, TA stands for transverse acoustic mode, LA stands for longitudinal acoustic mode, O represents optical mode.

The first order optical phonon band is well resolved at 540 cm^{-1} and energetically distant from the first order acoustic band. Other peaks, at 250 cm^{-1}, 350 cm^{-1}, 420 cm^{-1}, 800 cm^{-1} and 1100 cm^{-1}, can be assigned to second order transverse acoustic mode, the sum of transverse and longitudinal acoustic modes, the difference between optical and acoustic modes, the sum of optical and acoustic modes, and second order optical mode, respectively. It is worth noting that the first-order scattering peaks are not prominent in the Raman spectrum, which is due to the suppression of first order Raman effect by stoichiometric HfN with a low concentration of defects [259].

The source of first order Raman scattering is usually attributed to N vacancies i.e. stoichiometric defects. The X-ray diffractogram (XRD) (Figure 56) indicates HfN has a cubic fcc crystal structure and the dominant (1 1 1) diffraction peak is a strong symbol of stoichiometric HfN [260].

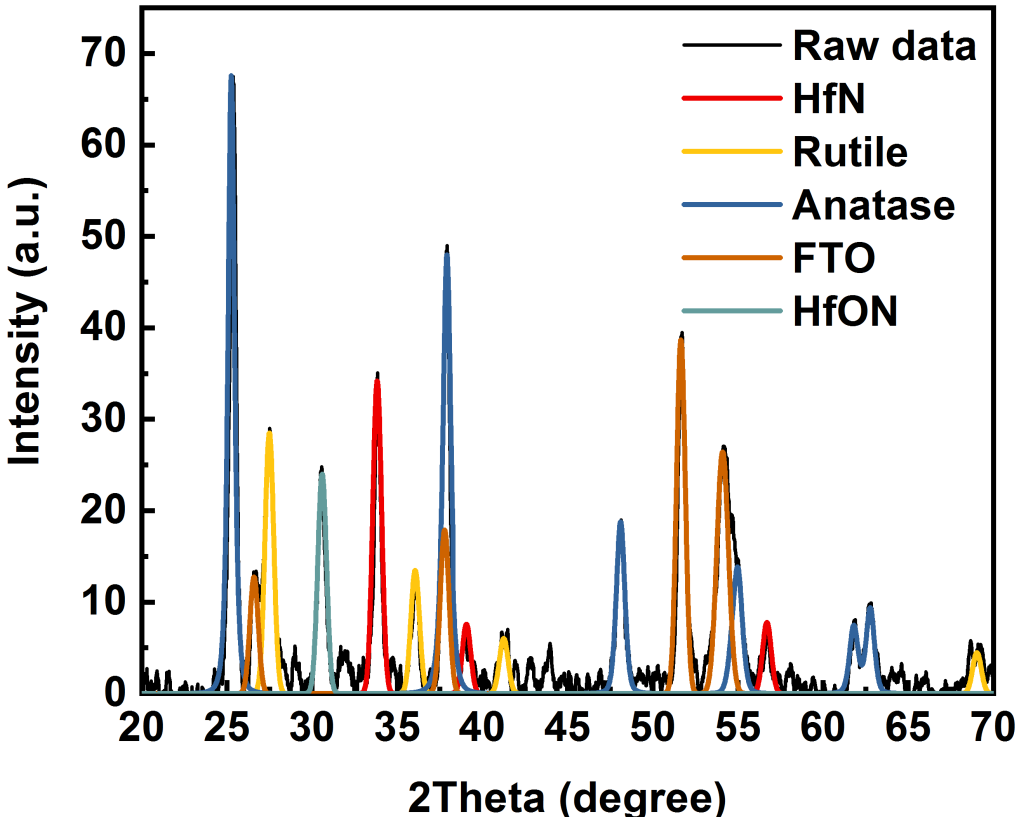

Figure 56: X-ray diffractogram of HfN-TNT sample, illustrating material components by separating signals.

Klemens decay is the primary pathway for the loss of energy of optical phonons and is attenuated by a large phononic bandgap [261]. According to the Raman spectrum we presented, the first order acoustic and the first order optical phonons were located at 140 cm^{-1} and 540 cm^{-1} respectively, meaning that the large energy difference between them prevents Klemens decay. This is a critical factor, because, when the decay of optical phonons is suppressed, a phonon bottleneck is created and hot carriers tend to have a longer

lifetime. HfN is a conductive ceramic with no electronic bandgap, which is a perfect characteristic for a hot carrier absorber [240]. The combination of these properties explains why we observed a small difference in photocurrent with and without UV filter, obtaining a photocurrent response 1.74 $mAcm^{-2}$ and 2.39 $mAcm^{-2}$ respectively, at an applied bias of +0.6 V during on-off cycles. Incident photons stimulate plasmon oscillations on the sample surface, which then decay into hot electron-hole pairs through Landau damping. Due to the presence of applied bias and relatively longer hot carrier lifetimes in HfN, the high energy holes were pushed to the anode-electrolyte interface prior to thermalization and oxidized the OH^- ions in the water-based electrolyte to form O_2. From a thermodynamic point of view, holes with energies higher than 1.23 eV are capable of splitting water. According to the AM 1.5 G solar spectral irradiance data, the percentage of photon flux (vs the cumulative flux of photons in sunlight) up to 750 nm (practical cut-off wavelength), is 31% with UV filter and 36% without UV filter, which is in close agreement with the ratio of photocurrent we obtained with and without UV filter [262].

6.4. Summary of this work

In this study, we reported a method for fabrication of core-shell nanotube arrays consisting of a 20 nm ALD HfN shell and an anodic TiO_2 nanotube support layer. To the best of our knowledge, it is the first report using HfN for photoelectrochemical water splitting. We observed excellent full visible regime photoactivity up to 730 nm from hydrogen evolution reaction and, based on our literature survey, the photocurrent density is superior to any TiO2 based photoanodes using plasmonic noble metal decoration. We consider the finding to be significant as it demonstrated the far-reaching application potential of replacing active

HER/HOR noble metals such as Au, Ag, Pt, Pd, etc. Moreover, the experimental results evidence two unique characteristics allowing a large population of long lifetime hot carriers, namely, a large bandgap between optical and acoustic phonon modes and the absence of an electronic bandgap, which particularly benefit hot carrier-based optoelectronic devices. It opens the window to a wide range of applications that enhance their performance using plasmonic noble metals including but not limited to photocatalysis, photosynthesis, dye degradation, and hot carrier solar cells.

7. Conclusion and Future Works

7.1. Key conclusions

The common thread that holds the thesis together is the exploitation of plasmon enhanced TiO_2 nanotube arrays based nanomaterials for nanophotonics, nonlinear optics, and especially photocatalysis. The main motivation of my research has been discussed in the first chapter. It introduces the rapid growing energy demands and huge conflicts between humanity and nature,

In chapter 2, we demonstrated the great potential of perovskite oxides as efficient catalysts for CO_2 photoreduction. Nanostructured perovskite oxides have emerged as a class of high-performance photocatalytic materials. The perovskite oxide candidates for CO_2 photoreduction are primarily nanostructured forms of titanates, niobates, tantalates and cobaltates. These materials form the focus of this review article because they are much sought-after due to their nontoxic nature, adequate chemical stability, and tunable crystal structures, bandgaps and surface energies. As compared to conventional semiconductors and nanomaterial catalysts, nanostructured perovskite oxides also exhibit an extended optical-absorption edge, longer charge carrier lifetimes, and favorable band-alignment with respect to reduction potential of activated CO_2 and reduction products of the same. While CO_2 reduction product yields of several hundred $\mu mol^{-1}h^{-1}$ are observed with many types of perovskite oxide nanomaterials in stand-alone forms, yield of such quantities are not common with semiconductor nanomaterials of other types. In this review, we present current state-of-the-art synthesis methods to form perovskite oxide nanomaterials, and procedures to engineer their bandgaps. This review also presents a comprehensive summary and discussion on crystal structures, defect distribution, morphologies and electronic properties of the perovskite oxides, and correlation of these properties to CO_2 photoreduction performance. This

review offers researchers key insights for developing advanced perovskite oxides in order to further improve the yields of CO_2 reduction products.

Having accomplished the review paper, nanophotonics and plasmons are considered as good angles to tackle the problem of photocatalyst with less efficiency. Hence, in chapter 3, it covers the fundamental knowledge of photonic crystals and plasmonics based on the focus of my PhD.

Chapter 4 is a published paper named "Optical control of selectivity of high rate CO_2 photoreduction via interband-or hot electron Z-scheme reaction pathways in Au-TiO_2 plasmonic photonic crystal photocatalyst." In this paper, photonic crystals consisting of TiO_2 nanotube arrays (PMTiNTs) with periodically modulated diameters were fabricated using a precise charge-controlled pulsed anodization technique. The PMTiNTs were decorated with gold nanoparticles (Au NPs) to form plasmonic photonic crystal photocatalysts (Au-PMTiNTs). A systematic study of CO_2 photoreduction performance on as-prepared samples was conducted using different wavelengths and illumination sequences. A remarkable selectivity of the mechanism of CO_2 photoreduction could be engineered by merely varying the spectral composition of the illumination sequence. Under AM1.5 G simulated sunlight (pathway#1), the Au-PMTiNTs produced methane (302 μmol h^{-1}) from CO_2 with high selectivity (89.3 %). When also illuminated by a UV-poor white lamp (pathway#2), the Au-PMTiNTs produced formaldehyde (420 μmol h−1) and carbon monoxide (323 μmol h^{-1}) with almost no methane evolved. We confirmed the photoreduction results by ^{13}C isotope labeling experiments using GC-MS. These results point to optical control of the selectivity of high-rate CO_2 photoreduction through selection of one of two different mechanistic pathways. Pathway#1 implicates electron-hole pairs generated through interband transitions in TiO_2 and Au as the primary active species responsible for reducing CO_2 to methane.

Pathway#2 involves excitation of both TiO_2 and surface plasmons in Au. Hot electrons produced by plasmon damping and photogenerated holes in TiO_2 proceed to reduce CO_2 to HCHO and CO through a plasmonic Z-scheme.

In chapter 5, it reports the investigation of TiN coated TiO_2 composite nanotubes. The laser ablation threshold of TiN@TNT was investigated and compared with that of gold using extrapolation of curves from laser fluence vs. squared damaged diameter. A significant increase in laser ablation tolerance from TiN@TNT was observed, which thanks to the nature of the material. For both TiN and gold, the influence of the laser pulse duration and the effect of morphologies were investigated under both femtosecond and picosecond laser irradiation. From the analyses, it can be concluded that femtosecond laser ablation is more efficient than picosecond pulsed laser because it is a non-thermal process, and the presence of nanostructures benefits light trapping and confinement of heat conduction. Furthermore, the suppositions on light interaction and heat conduction were supported by simulations using Lumerical FDTD and HEAT. Additionally, we have proved the potential of TiN being an optical limiter through nonlinear transmission optical test.

In chapter 6, a core-shell nanotube catalyst was fabricated consisting of atomic layer deposited HfN shell and anodic TiO_2 support layer with full-visible regime photoactivity for photoelectrochemical water splitting. The HfN active layer has two unique characteristics: a large bandgap between optical and acoustic phonon modes, and no electronic bandgap, which allow a large population of long life-time hot carriers, which are used to enhance the photoelectrochemical performance. The photocurrent density (~ 3 $mAcm^{-2}$ at 1 V vs Ag/AgCl) obtained in this study under AM1.5G 1 Sun illumination is unprecedented, as it is superior to most existing plasmonic

noble metal decorated catalysts and surprisingly indicates a photocurrent response that extends to 730 nm. The result demonstrates the far-reaching application potential of replacing active HER/HOR noble metals such as Au, Ag, Pt, Pd, etc with low-cost plasmonic ceramics.

7.2. Future works

Future works can be carried out in the following aspects.

In the context of further boost photocatalytic efficiency by improving light management, advanced fabrication techniques are required for precise control of the size, geometry and position of nanostrcutres. We have seen the relation between nanostructure and catalytic activity as described in the previous Au-PMTiNT research. Not only the photocatalytic performance but the selectivity can be controlled by light manipulation. There are many the state of art techniques exhibiting the capability of fabricating sophisticated and periodic nanostructures such as nanoimprint lithography, microelectrical discharge machining, laser scanning holographic lithography. The future outlook of a rational nanostructure for photocatalysis should include many features including but not limited to highly efficient light absorption and large active surface area. However, it still requires large amount of efforts and will encounter unexpected challenges. Progress in nanofabrication skills will open the door of solar energy harvesting wider.

Additionally, exploiting new nanomaterials is also important in the research pathway. The first priority is to explore the inventory of non-toxic, earth-abundant, and high-performance materials. Graphitic carbon nitride is novel and appealing 2D material that has demonstrated its remarkable potential and gained large recognition from scientists. Another particular attention is paid to

substitute expensive noble metals as we mentioned in previous chapters. Transition metal nitrides are good candidates that are still in preliminary stage and require intensively study.

Lastly, exploring the applications of newly developed nanostructures and nanomaterials would be another significant step. Besides applications we have investigated in this thesis, there two categories worth more study that are photoelectrochemical CO_2 reduction and photothermal heating. Photoelectrochemical water splitting has proved its feasibility as a practical method for hydrogen generation. The same may happen with CO_2 reduction considering the urgency of closing carbon loop and the value of producing fuels. It might become the fast track for us to further improve solar penetration and facilitate CO_2 conversion. Similarly, photothermal effect has been widely used in many scenarios which we have discussed in the chapter 5. We can expect great results from optimized transition metal nitrides with rational nanostructure design.

Hitherto, there is still a long way to go before commercially use photocatalysis to provide clean and inexpensive energy, despite recent remarkable progress and appealing findings. However, it does not limit the opportunity of photocatalysis. As a whole, the abovementioned issues will be used as a mind map for the future research.

Reference

[1] A. Gatto, F. Busato, Journal of Cleaner Production, 253 (2020).
[2] R. Smalley, Public Lecture presented at Low Library, 23 (2003).
[3] G.A. Jones, K.J. Warner, Energy Policy, 93 (2016) 206-212.
[4] B. Dudley, BP Statistical Review of World Energy, BP p.l.c., 2019.
[5] I.E. Agency, World Energy Outlook 2018, 2018.
[6] M. Planck, Annalen der Physik, 4 (1901).
[7] K. Branker, M.J.M. Pathak, J.M. Pearce, Renew. Sust. Energ. Rev., 15 (2011) 4470-4482.
[8] B. Parida, S. Iniyan, R. Goic, Renew. Sust. Energ. Rev., 15 (2011) 1625-1636.
[9] A. Polman, M. Knight, E.C. Garnett*, et al.*, Science, 352 (2016) 10.
[10] T.T. Chow, Appl. Energy, 87 (2010) 365-379.
[11] Y. Tian, C.Y. Zhao, Appl. Energy, 104 (2013) 538-553.
[12] A. Sharma, V.V. Tyagi, C.R. Chen*, et al.*, Renew. Sust. Energ. Rev., 13 (2009) 318-345.
[13] R.E. Blankenship, D.M. Tiede, J. Barber*, et al.*, Science, 332 (2011) 805-809.
[14] W.G. Tu, Y. Zhou, Z.G. Zou, Adv. Mater., 26 (2014) 4607-4626.
[15] M.M. Liu, X.H. Ren, C. Cheng*, et al.*, Science of the Total Environment, 718 (2020).
[16] M. Muntean, D. Guizzardi, E. Schaaf*, et al.*, Publications Office of the European Union, Luxembourg., (2018).
[17] S. Tausz-Posch, M. Tausz, M.J.P.B. Bourgault, (2019).
[18] S. Solomon, J.S. Daniel, T.J. Sanford*, et al.*, Proceedings of the National Academy of Sciences, 107 (2010) 18354.
[19] U. Ulmer, T. Dingle, P.N. Duchesne*, et al.*, Nature Communications, 10 (2019) 3169.
[20] X. Chang, T. Wang, J. Gong, Energy & Environmental Science, 9 (2016) 2177-2196.
[21] X. Zhang, F. Han, B. Shi*, et al.*, Angewandte Chemie International Edition, 51 (2012) 12732-12735.
[22] G. Bengough, J.J.G.P. Stuart, 223994 (1923).
[23] R.J. Holly Shaftel, Susan Callery, Carbon dioxide concentration | NASA Global Climate Change, 2017, May 17.
[24] S. Solomon, Climate change 2007-the physical science basis: Working group I contribution to the fourth assessment report of the IPCC, Cambridge University Press2007.
[25] J.D. Froehlich, C.P. Kubiak, Inorganic chemistry, 51 (2012) 3932-3934.
[26] J. Bonin, M. Chaussemier, M. Robert*, et al.*, ChemCatChem, 6 (2014) 3200-3207.
[27] M. Beley, J.-P. Collin, R. Ruppert*, et al.*, Journal of the Chemical Society, Chemical Communications, (1984) 1315-1316.
[28] D.S. Laitar, P. Müller, J.P. Sadighi, Journal of the American Chemical Society, 127 (2005) 17196-17197.
[29] M. Cokoja, C. Bruckmeier, B. Rieger*, et al.*, Angewandte Chemie International Edition, 50 (2011) 8510-8537.
[30] A.J. Morris, G.J. Meyer, E. Fujita, Accounts of Chemical Research, 42 (2009) 1983-1994.
[31] J.-M. Savéant, Chemical Reviews, 108 (2008) 2348-2378.
[32] M. Halmann, Nature, 275 (1978) 115-116.
[33] I. Taniguchi, B. Aurian-Blajeni, J.O.M. Bockris, Journal of electroanalytical chemistry and interfacial electrochemistry, 161 (1984) 385-388.
[34] B. Blajeni, M. Halmann, J. Manassen, Sol Energy Mater, 8 (1983) 425-440.

[35] Y. Hori, K. Kikuchi, S. Suzuki, Chemistry Letters, 14 (1985) 1695-1698.
[36] M. Le, M. Ren, Z. Zhang, *et al.*, Journal of the Electrochemical Society, 158 (2011) E45-E49.
[37] A.E. Ashley, A.L. Thompson, D. O'Hare, Angewandte Chemie, 121 (2009) 10023-10027.
[38] J.A. Rodriguez, P. Liu, D.J. Stacchiola, *et al.*, ACS Catalysis, 5 (2015) 6696-6706.
[39] S.G. Jadhav, P.D. Vaidya, B.M. Bhanage, *et al.*, Chemical Engineering Research and Design, 92 (2014) 2557-2567.
[40] S. Saeidi, N.A.S. Amin, M.R. Rahimpour, Journal of CO2 Utilization, 5 (2014) 66-81.
[41] K. Wenderich, G. Mul, Chemical reviews, 116 (2016) 14587-14619.
[42] W.-J. Ong, L.-L. Tan, Y.H. Ng, *et al.*, Chemical Reviews, 116 (2016) 7159-7329.
[43] J. Shi, D.d. Zhang, W. Zi, *et al.*, ChemSusChem, n/a-n/a.
[44] W.-J. Ong, Frontiers in Materials, 4 (2017).
[45] P. Kar, Y. Zhang, S. Farsinezhad, *et al.*, Chemical Communications, 51 (2015) 7816-7819.
[46] P. Kar, Y. Zhang, N. Mahdi, *et al.*, Nanotechnology, (2017).
[47] D. Zeng, L. Xiao, W.-J. Ong, *et al.*, ChemSusChem, n/a-n/a.
[48] S. Chu, W. Li, Y. Yan, *et al.*, Nano Futures, 1 (2017) 022001.
[49] S. Li, G. Dong, R. Hailili, *et al.*, Applied Catalysis B: Environmental, 190 (2016) 26-35.
[50] Y. Shiraishi, S. Kanazawa, Y. Sugano, *et al.*, ACS Catalysis, 4 (2014) 774-780.
[51] R. Asahi, T. Morikawa, T. Ohwaki, *et al.*, Science, 293 (2001) 269-271.
[52] Q.I. Rahman, M. Ahmad, S.K. Misra, *et al.*, Journal of nanoscience and nanotechnology, 12 (2012) 7181-7186.
[53] B.M. Comer, M. Nazemi, M.C. Hatzell, *et al.*, arXiv preprint arXiv:1707.03031, (2017).
[54] Q. Han, N. Chen, J. Zhang, *et al.*, Materials Horizons, 4 (2017) 832-850.
[55] C. Pengfei, L. Neng, C. Xingzhu, *et al.*, 2D Materials, 5 (2018) 014002.
[56] D. Zeng, W.-J. Ong, H. Zheng, *et al.*, Journal of Materials Chemistry A, 5 (2017) 16171-16178.
[57] X. Chen, N. Li, Z. Kong, *et al.*, Materials Horizons, (2018).
[58] Y. Chen, X. Xin, N. Zhang, *et al.*, Particle & Particle Systems Characterization, 34 (2017) 1600357.
[59] T. Inoue, A. Fujishima, S. Konishi, *et al.*, Nature, 277 (1979) 637-638.
[60] Y. Chen, C.-H. Chuang, Z. Qin, *et al.*, Nanotechnology, 28 (2017) 084002.
[61] S. Navalón, A. Dhakshinamoorthy, M. Álvaro, *et al.*, ChemSusChem, 6 (2013) 562-577.
[62] P. Kar, S. Farsinezhad, X. Zhang, *et al.*, Nanoscale, 6 (2014) 14305-14318.
[63] C. Zhu, Z. Jiang, L. Chen, *et al.*, Nanotechnology, 28 (2017) 115708.
[64] B. Kumar, M. Asadi, D. Pisasale, *et al.*, Nature communications, 4 (2013).
[65] C.M. Mömming, E. Otten, G. Kehr, *et al.*, Angewandte Chemie International Edition, 48 (2009) 6643-6646.
[66] M. Rakowski Dubois, D.L. Dubois, Accounts of Chemical Research, 42 (2009) 1974-1982.
[67] J. Collin, J. Sauvage, Coordination Chemistry Reviews, 93 (1989) 245-268.
[68] W.-J. Ong, L.K. Putri, Y.-C. Tan, *et al.*, Nano Research, 10 (2017) 1673-1696.
[69] Y. Zhu, C. Gao, S. Bai, *et al.*, Nano Research, 10 (2017) 3396-3406.
[70] B. Pan, Y. Zhou, W. Su, *et al.*, Nano Research, 10 (2017) 534-545.
[71] F. Rechberger, M. Niederberger, Materials Horizons, 4 (2017) 1115-1121.
[72] G. Yang, D. Chen, H. Ding, *et al.*, Applied Catalysis B: Environmental, 219 (2017) 611-618.

[73] W.-H. Wang, Y. Himeda, J.T. Muckerman, *et al.*, Chemical reviews, 115 (2015) 12936-12973.
[74] H. Takeda, C. Cometto, O. Ishitani, *et al.*, (2016).
[75] N. Li, X. Chen, W.-J. Ong, *et al.*, ACS nano, (2017).
[76] J.W. Maina, C. Pozo-Gonzalo, L. Kong, *et al.*, Materials Horizons, 4 (2017) 345-361.
[77] K.D. Yang, C.W. Lee, J.H. Jang, *et al.*, Nanotechnology, 28 (2017) 352001.
[78] J. Luo, J.-H. Im, M.T. Mayer, *et al.*, Science, 345 (2014) 1593.
[79] A.R. Bin, M. Yusoff, J. Jang, Chemical Communications, 52 (2016) 5824-5827.
[80] C. Wang, S. Yang, X. Chen, *et al.*, Journal of Materials Chemistry A, 5 (2017) 910-913.
[81] J. Hou, S. Cao, Y. Wu, *et al.*, Chemistry – A European Journal, 23 (2017) 9481-9485.
[82] M. Schreier, L. Curvat, F. Giordano, *et al.*, 6 (2015) 7326.
[83] Y.-F. Xu, M.-Z. Yang, B.-X. Chen, *et al.*, J. Am. Chem. Soc, 139 (2017) 5660-5663.
[84] I. Grinberg, D.V. West, M. Torres, *et al.*, Nature, 503 (2013) 509-512.
[85] J. Suntivich, H.A. Gasteiger, N. Yabuuchi, *et al.*, Nature Chemistry, 3 (2011) 546-550.
[86] R.A. De Souza, Advanced Functional Materials, 25 (2015) 6326-6342.
[87] C.G. Morales-Guio, M.T. Mayer, A. Yella, *et al.*, Journal of the American Chemical Society, 137 (2015) 9927-9936.
[88] K. Peng, L.J. Fu, H.M. Yang, *et al.*, Scientific Reports, 6 (2016).
[89] V. Jeyalakshmi, R. Mahalakshmy, K. Ramesh, *et al.*, Rsc Advances, 5 (2015) 5958-5966.
[90] J. Schooley, W. Hosler, M.L. Cohen, Physical Review Letters, 12 (1964) 474.
[91] J. Appel, Physical Review Letters, 17 (1966) 1045.
[92] Y. Maeno, H. Hashimoto, K. Yoshida, *et al.*, Nature, 372 (1994) 532.
[93] R. Cava, B. Batlogg, J. Krajewski, *et al.*, Nature, 332 (1988) 814-816.
[94] Z. Zhang, L. Zhang, M.N. Hedhili, *et al.*, Nano Letters, 13 (2013) 14-20.
[95] H. Frederikse, W. Hosler, W. Thurber, Physical Review, 143 (1966) 648.
[96] K.-I. Kobayashi, T. Kimura, H. Sawada, *et al.*, Nature, 395 (1998) 677-680.
[97] R.B. Hassine, J. Sánchez-Benítez, J. Alonso, *et al.*, Journal of Alloys and Compounds, 696 (2017) 73-78.
[98] P. Rout, I. Agireen, E. Maniv, *et al.*, arXiv preprint arXiv:1701.02153, (2017).
[99] S.A. Khandy, D.C. Gupta, International Journal of Quantum Chemistry, (2017).
[100] A.K. Yadav, P. Rajput, O. Alshammari, *et al.*, Journal of Alloys and Compounds, 701 (2017) 619-625.
[101] G. Song, G. Li, B. Gao, *et al.*, Journal of Alloys and Compounds, 690 (2017) 923-929.
[102] R. Voorhoeve, D. Johnson, J. Remeika, *et al.*, Science, 195 (1977) 827-833.
[103] T. Seiyama, Catalysis Reviews, 34 (1992) 281-300.
[104] A. Kudo, Y. Miseki, Chemical Society Reviews, 38 (2009) 253-278.
[105] Y. Inoue, Energy & Environmental Science, 2 (2009) 364-386.
[106] E. Grabowska, Applied Catalysis B: Environmental, 186 (2016) 97-126.
[107] P. Kanhere, Z. Chen, Molecules, 19 (2014) 19995-20022.
[108] G. Zhang, G. Liu, L. Wang, *et al.*, Chemical Society Reviews, 45 (2016) 5951-5984.
[109] M. Arash, K. Piyush, D.W. Benjamin, *et al.*, Current Nanoscience, 11 (2015) 593-614.
[110] R. Shi, G.I.N. Waterhouse, T. Zhang, Solar RRL, 1 (2017) 1700126.
[111] W. Wang, M.O. Tadé, Z. Shao, Chemical Society Reviews, 44 (2015) 5371-5408.
[112] K. Li, X. An, K.H. Park, *et al.*, Catalysis Today, 224 (2014) 3-12.
[113] K. Xie, N. Umezawa, N. Zhang, *et al.*, Energy & Environmental Science, 4 (2011) 4211-4219.

[114] H. Zhou, J. Guo, P. Li, *et al.*, Scientific Reports, 3 (2013) 1667.
[115] O.K. Varghese, M. Paulose, T.J. LaTempa, *et al.*, Nano Letters, 9 (2009) 731-737.
[116] S. Rani, N. Bao, S.C. Roy, Applied Surface Science, 289 (2014) 203-208.
[117] P. Kar, S. Farsinezhad, N. Mahdi, *et al.*, Nano Research, 9 (2016) 3478-3493.
[118] L. Jia, J. Li, W. Fang, *et al.*, Catal. Commun., 10 (2009) 1230-1234.
[119] F. Yoshitomi, K. Sekizawa, K. Maeda, *et al.*, ACS applied materials & interfaces, 7 (2015) 13092-13097.
[120] Y. Hori, H. Wakebe, T. Tsukamoto, *et al.*, Electrochimica Acta, 39 (1994) 1833-1839.
[121] S. Shoji, G. Yin, M. Nishikawa, *et al.*, Chemical Physics Letters, 658 (2016) 309-314.
[122] K. Li, A.D. Handoko, M. Khraisheh, *et al.*, Nanoscale, 6 (2014) 9767-9773.
[123] B. Gholamkhass, H. Mametsuka, K. Koike, *et al.*, Inorganic Chemistry, 44 (2005) 2326-2336.
[124] G. Xu, X. Huang, V. Krstic, *et al.*, CrystEngComm, 16 (2014) 4373-4376.
[125] D. Caruntu, T. Rostamzadeh, T. Costanzo, *et al.*, Nanoscale, 7 (2015) 12955-12969.
[126] K.M. Parida, K.H. Reddy, S. Martha, *et al.*, International Journal of Hydrogen Energy, 35 (2010) 12161-12168.
[127] S. Phokha, S. Pinitsoontorn, S. Maensiri, *et al.*, Journal of sol-gel science and technology, 71 (2014) 333-341.
[128] S. Yin, Y. Zhu, Z. Ren, *et al.*, Journal of Materials Chemistry A, 2 (2014) 9035-9039.
[129] L. Vradman, E. Friedland, J. Zana, *et al.*, Journal of Materials Science, 52 (2017) 11383-11390.
[130] C. Wattanawikkam, W. Pecharapa, IEEE transactions on ultrasonics, ferroelectrics, and frequency control, 63 (2016) 1663-1667.
[131] P. Tang, Y. Tong, H. Chen, *et al.*, Current Applied Physics, 13 (2013) 340-343.
[132] J. Zhu, H. Li, L. Zhong, *et al.*, ACS Catalysis, 4 (2014) 2917-2940.
[133] B.S. Kwak, M. Kang, Appl. Surf. Sci., 337 (2015) 138-144.
[134] W. Dong, X. Li, J. Yu, *et al.*, Materials Letters, 67 (2012) 131-134.
[135] Z. Zheng, B. Huang, X. Qin, *et al.*, Journal of colloid and interface science, 358 (2011) 68-72.
[136] A. Sobhani-Nasab, S.M. Hosseinpour-Mashkani, M. Salavati-Niasari, *et al.*, Journal of Cluster Science, 26 (2015) 1305-1318.
[137] A. Moghtada, R. Ashiri, Ultrasonics sonochemistry, 33 (2016) 141-149.
[138] W. Li, Z. Wang, F. Deschler, *et al.*, Nature Reviews Materials, (2017) 16099.
[139] T. Ishihara, Perovskite oxide for solid oxide fuel cells, Springer Science & Business Media2009.
[140] M. Pena, J. Fierro, Chemical reviews, 101 (2001) 1981-2018.
[141] A. Kubacka, M. Fernández-García, G. Colón, Chemical Reviews, 112 (2012) 1555-1614.
[142] H.D. Megaw, Proceedings of the Physical Society, 58 (1946) 133.
[143] T. Jafari, E. Moharreri, A.S. Amin, *et al.*, Molecules, 21 (2016) 900.
[144] N.M. Flores, U. Pal, R. Galeazzi, *et al.*, RSC Advances, 4 (2014) 41099-41110.
[145] X. Zhang, J. Qin, Y. Xue, *et al.*, Scientific reports, 4 (2014) 4596.
[146] S. Chaturvedi, P.N. Dave, N. Shah, Journal of Saudi Chemical Society, 16 (2012) 307-325.
[147] S. Liu, C. Li, J. Yu, *et al.*, CrystEngComm, 13 (2011) 2533-2541.
[148] H. Kato, K. Asakura, A. Kudo, Journal of the American Chemical Society, 125 (2003) 3082-3089.

[149] S.R. Kumar, C.V. Abinaya, S. Amirthapandian, *et al.*, Mater. Res. Bull., 93 (2017) 270-281.
[150] S. Fu, H. Niu, Z. Tao, *et al.*, Journal of Alloys and Compounds, 576 (2013) 5-12.
[151] X. Zhu, Z. Liu, N. Ming, Journal of Materials Chemistry, 20 (2010) 4015-4030.
[152] Y.D. Zhang, X.M. Pan, Z. Wang, *et al.*, Rsc Advances, 5 (2015) 20453-20458.
[153] J. Zhang, Y. Zhao, X. Zhao, *et al.*, Scientific reports, 4 (2014).
[154] P. Li, S. Ouyang, G. Xi, *et al.*, The Journal of Physical Chemistry C, 116 (2012) 7621-7628.
[155] R. Konta, T. Ishii, H. Kato, *et al.*, The Journal of Physical Chemistry B, 108 (2004) 8992-8995.
[156] H.-C. Chen, C.-W. Huang, J.C.S. Wu, *et al.*, The Journal of Physical Chemistry C, 116 (2012) 7897-7903.
[157] B. Wang, P.D. Kanhere, Z. Chen, *et al.*, The Journal of Physical Chemistry C, 117 (2013) 22518-22524.
[158] B. Weng, Z. Xiao, W. Meng, *et al.*, Advanced Energy Materials, 7 (2017) 1602260-n/a.
[159] H. Kato, A. Kudo, The Journal of Physical Chemistry B, 106 (2002) 5029-5034.
[160] R. Niishiro, H. Kato, A. Kudo, Physical Chemistry Chemical Physics, 7 (2005) 2241-2245.
[161] D.Q. Fei, T. Hudaya, A.A. Adesina, Catalysis Communications, 6 (2005) 253-258.
[162] D. Wang, T. Kako, J. Ye, The Journal of Physical Chemistry C, 113 (2009) 3785-3792.
[163] W. Luo, Z. Li, X. Jiang, *et al.*, Physical Chemistry Chemical Physics, 10 (2008) 6717-6723.
[164] J.C. Hemminger, R. Carr, G.A. Somorjai, Chem. Phys. Lett., 57 (1978) 100-104.
[165] H. Shi, T. Wang, J. Chen, *et al.*, Catalysis Letters, 141 (2011) 525-530.
[166] H. Shi, G. Chen, C. Zhang, *et al.*, ACS Catalysis, 4 (2014) 3637-3643.
[167] H. Shi, C. Zhang, C. Zhou, *et al.*, RSC Advances, 5 (2015) 93615-93622.
[168] H. Shi, Z. Zou, J. Phys. Chem. Solids, 73 (2012) 788-792.
[169] H. Zhou, P. Li, J. Guo, *et al.*, Nanoscale, 7 (2015) 113-120.
[170] F. Fresno, P. Jana, P. Renones, *et al.*, Photochemical & Photobiological Sciences, 16 (2017) 17-23.
[171] R.K. Nath, M.F.M. Zain, A.A.H. Kadhum, Advances in Natural and Applied Sciences, 6 (2012) 1030-1035.
[172] J.Y. Do, Y. Im, B.S. Kwak, *et al.*, Ceram. Int., 42 (2016) 5942-5951.
[173] L. Jia, J. Li, W. Fang, Catalysis Communications, 11 (2009) 87-90.
[174] K. Iizuka, T. Wato, Y. Miseki, *et al.*, Journal of the American Chemical Society, 133 (2011) 20863-20868.
[175] Z. Sun, Z. Yang, H. Liu, *et al.*, Appl. Surf. Sci., 315 (2014) 360-367.
[176] L. Liang, F. Lei, S. Gao, *et al.*, Angewandte Chemie International Edition, 54 (2015) 13971-13974.
[177] X.Y. Kong, W.L. Tan, B.-J. Ng, *et al.*, Nano Res., (2017) 1-12.
[178] Y. Zhou, Z. Tian, Z. Zhao, *et al.*, ACS Appl. Mater. Interfaces, 3 (2011) 3594-3601.
[179] S. Wang, Y. Hou, X. Wang, ACS applied materials & interfaces, 7 (2015) 4327-4335.
[180] Q. Liu, D. Wu, Y. Zhou, *et al.*, ACS applied materials & interfaces, 6 (2014) 2356-2361.
[181] Y. Im, S.-M. Park, M. Kang, Bulletin of the Korean Chemical Society, 38 (2017) 397-400.
[182] S. Mishra, N. Choudhury, S. Chaplot, *et al.*, Physical Review B, 76 (2007) 024110.
[183] S. Mishra, R. Mittal, V.Y. Pomjakushin, *et al.*, Physical Review B, 83 (2011) 134105.

[184] M. Stock, S. Dunn, IEEE transactions on ultrasonics, ferroelectrics, and frequency control, 58 (2011).
[185] M. Li, P. Li, K. Chang, *et al.*, Chemical Communications, 51 (2015) 7645-7648.
[186] J. Hou, S. Cao, Y. Wu, *et al.*, Nano Energy, 30 (2016) 59-68.
[187] V. Jeyalakshmi, S. Tamilmani, R. Mahalakshmy, *et al.*, Journal of Molecular Catalysis A: Chemical, 420 (2016) 200-207.
[188] K. Teramura, S.-i. Okuoka, H. Tsuneoka, *et al.*, Applied Catalysis B: Environmental, 96 (2010) 565-568.
[189] O.U. Osazuwa, C.K. Cheng, Journal of Cleaner Production, 148 (2017) 202-211.
[190] X. Liu, P. Long, Z. Sun, *et al.*, Journal of Materials Chemistry C, 4 (2016) 7563-7570.
[191] H. Yamashita, H. Li, Nanostructured Photocatalysts: Advanced Functional Materials, Springer2016.
[192] W. Meng, H. Qiutong, L. Liang, *et al.*, Nanotechnology, 28 (2017) 274002.
[193] T.J. Jacobsson, V. Fjällström, M. Sahlberg, *et al.*, Energy & Environmental Science, 6 (2013) 3676-3683.
[194] D.S. Simakov, Renewable Synthetic Fuels and Chemicals from Carbon Dioxide: Fundamentals, Catalysis, Design Considerations and Technological Challenges, Springer2017.
[195] M. Ohtsu, K. Kobayashi, T. Kawazoe, *et al.*, Principles of Nanophotonics, Crc Press-Taylor & Francis Group, Boca Raton, 2008.
[196] C. Fenzl, T. Hirsch, O.S. Wolfbeis, 53 (2014) 3318-3335.
[197] I.A. Sukhoivanov, I.V. Guryev, Photonic crystals: physics and practical modeling, Springer2009.
[198] Y. Li, T. Kunitake, S. Fujikawa, The Journal of Physical Chemistry B, 110 (2006) 13000-13004.
[199] J.I.L. Chen, G. von Freymann, S.Y. Choi, *et al.*, 18 (2006) 1915-1919.
[200] G. Liao, S. Chen, X. Quan, *et al.*, Environmental Science & Technology, 44 (2010) 3481-3485.
[201] X. Zhang, Y. Liu, S.-T. Lee, *et al.*, Energy & Environmental Science, 7 (2014) 1409-1419.
[202] D. Pines, D. Bohm, Physical Review, 85 (1952) 338-353.
[203] X. Huang, I.H. El-Sayed, W. Qian, *et al.*, Journal of the American Chemical Society, 128 (2006) 2115-2120.
[204] K.R. Catchpole, A. Polman, Opt. Express, 16 (2008) 21793-21800.
[205] M. Moskovits, Reviews of Modern Physics, 57 (1985) 783-826.
[206] N. Zhou, X. Xu, T. Hammack Aaron, *et al.*, Plasmonic near-field transducer for heat-assisted magnetic recording, Nanophotonics, 2014, pp. 141.
[207] X. Zhang, Y.L. Chen, R.-S. Liu, *et al.*, Reports on Progress in Physics, 76 (2013) 046401.
[208] P. Kar, S. Zeng, Y. Zhang, *et al.*, Applied Catalysis B: Environmental, 243 (2019) 522-536.
[209] X.D. Wang, J. Choi, D.R.G. Mitchell, *et al.*, Chemcatchem, 5 (2013) 2646-2654.
[210] Z.B. Hai, N. El Kolli, D.B. Uribe, *et al.*, Journal of Materials Chemistry A, 1 (2013) 10829-10835.
[211] J.S. DuChene, B.C. Sweeny, A.C. Johnston-Peck, *et al.*, Angewandte Chemie International Edition, 53 (2014) 7887-7891.
[212] M.H. Zarifi, A. Mohammadpour, S. Farsinezhad, *et al.*, The Journal of Physical Chemistry C, 119 (2015) 14358-14365.
[213] W. Hou, W.H. Hung, P. Pavaskar, *et al.*, ACS Catalysis, 1 (2011) 929-936.

[214] Y. Izumi, Coordination Chemistry Reviews, 257 (2013) 171-186.
[215] S.N. Habisreutinger, L. Schmidt-Mende, J.K. Stolarczyk, Angewandte Chemie International Edition, 52 (2013) 7372-7408.
[216] Y. Liu, S. Zhou, J. Li, *et al.*, Applied Catalysis B: Environmental, 168 (2015) 125-131.
[217] A.L. Linsebigler, G. Lu, J.T. Yates Jr, Chemical reviews, 95 (1995) 735-758.
[218] X. Zheng, L. Zhang, Energy & Environmental Science, 9 (2016) 2511-2532.
[219] K. Ishizaki, S. Noda, Nature, 460 (2009) 367.
[220] J.I. Chen, G. von Freymann, V. Kitaev, *et al.*, Journal of the American Chemical Society, 129 (2007) 1196-1202.
[221] V. Subramanian, E.E. Wolf, P.V. Kamat, Journal of the American Chemical Society, 126 (2004) 4943-4950.
[222] H. Tada, T. Mitsui, T. Kiyonaga, *et al.*, Nature Materials, 5 (2006) 782.
[223] S.t. Neaţu, J.A. Maciá-Agulló, P. Concepción, *et al.*, Journal of the American Chemical Society, 136 (2014) 15969-15976.
[224] Y. Zou, J.W. Shi, D. Ma, *et al.*, ChemCatChem, 9 (2017) 3752-3761.
[225] Y. Bai, T. Chen, P. Wang, *et al.*, Solar Energy Materials and Solar Cells, 157 (2016) 406-414.
[226] R. Bhosale, S. Jain, C.P. Vinod, *et al.*, ACS Applied Materials & Interfaces, 11 (2019) 6174-6183.
[227] W.S. Williams, Prog. Solid State Chem., 6 (1971) 57-118.
[228] S.T. Oyama, Introduction to the chemistry of transition metal carbides and nitrides, in: S.T. Oyama (Ed.) The Chemistry of Transition Metal Carbides and Nitrides, Springer Netherlands, Dordrecht, 1996, pp. 1-27.
[229] U. Guler, V.M. Shalaev, A. Boltasseva, Materials Today, 18 (2015) 227-237.
[230] J. Bonse, H. Sturm, D. Schmidt, *et al.*, Applied Physics A, 71 (2000) 657-665.
[231] J. Bonse, P. Rudolph, J. Krüger, *et al.*, Applied Surface Science, 154-155 (2000) 659-663.
[232] C.D. Hodgman, S.C. Lind, The Journal of Physical and Colloid Chemistry, 53 (1949) 1139-1139.
[233] O. Ekici, R.K. Harrison, N.J. Durr, *et al.*, Journal of Physics D: Applied Physics, 41 (2008) 185501.
[234] B.N. Chichkov, C. Momma, S. Nolte, *et al.*, Applied Physics A, 63 (1996) 109-115.
[235] E. Traver, R.A. Karaballi, Y.E. Monfared, *et al.*, ACS Applied Nano Materials, 3 (2020) 2787-2794.
[236] S. Rej, L. Mascaretti, E.Y. Santiago, *et al.*, ACS Catalysis, 10 (2020) 5261-5271.
[237] O. Anjaneyulu, S. Ishii, T. Imai, *et al.*, RSC Advances, 6 (2016) 110566-110570.
[238] R.A. Karaballi, Y. Esfahani Monfared, M. Dasog, Langmuir, 36 (2020) 5058-5064.
[239] B. Saha, J. Acharya, T.D. Sands, *et al.*, 107 (2010) 033715.
[240] S. Chung, S. Shrestha, X. Wen, *et al.*, Solar Energy Materials and Solar Cells, 144 (2016) 781-786.
[241] C. Defilippi, D.V. Shinde, Z. Dang, *et al.*, 58 (2019) 15464-15470.
[242] X. Yang, F. Zhao, Y.-W. Yeh, *et al.*, Nature Communications, 10 (2019) 1543.
[243] S. Farsinezhad, A. Mohammadpour, A.N. Dalrymple, *et al.*, Journal of nanoscience and nanotechnology, 13 (2013) 2885-2891.
[244] V. Galstyan, A. Vomiero, I. Concina, *et al.*, Small, 7 (2011) 2437-2442.
[245] S. Farsinezhad, A.N. Dalrymple, K. Shankar, physica status solidi (a), 211 (2014) 1113-1121.

[246] T. Muneshwar, K. Cadien, Applied Surface Science, 435 (2018) 367-376.
[247] X.-Z. Wang, T.P. Muneshwar, H.-Q. Fan*, et al.*, Journal of Power Sources, 397 (2018) 32-36.
[248] T. Muneshwar, K. Cadien, Journal of Vacuum Science & Technology A, 33 (2015) 031502.
[249] M. Sun, Y. Fang, S. Sun*, et al.*, RSC Advances, 6 (2016) 12272-12279.
[250] C. Peng, W. Wang, W. Zhang*, et al.*, Applied Surface Science, 420 (2017) 286-295.
[251] M.-Z. Ge, C.-Y. Cao, S.-H. Li*, et al.*, Nanoscale, 8 (2016) 5226-5234.
[252] D.B. Ingram, S. Linic, Journal of the American Chemical Society, 133 (2011) 5202-5205.
[253] J. Luo, D. Li, Y. Yang*, et al.*, Journal of Alloys and Compounds, 661 (2016) 380-388.
[254] J. Luo, J. Chen, H. Wang*, et al.*, Journal of Power Sources, 303 (2016) 287-293.
[255] J. Chen, C.S. Bailey, Y. Hong*, et al.*, ACS Photonics, 6 (2019) 787-792.
[256] Z. Zhan, J. An, H. Zhang*, et al.*, ACS Applied Materials & Interfaces, 6 (2014) 1139-1144.
[257] F. Su, T. Wang, R. Lv*, et al.*, Nanoscale, 5 (2013) 9001-9009.
[258] Y.-C. Pu, G. Wang, K.-D. Chang*, et al.*, Nano Letters, 13 (2013) 3817-3823.
[259] M. Stoehr, H.-S. Seo, I. Petrov*, et al.*, 104 (2008) 033507.
[260] L. Yuan, G. Fang, C. Li*, et al.*, Applied Surface Science, 253 (2007) 8538-8542.
[261] S. Chung, S. Shrestha, X. Wen*, et al.*, solar cells, 3 (2014) 5.
[262] R. Kroon, M. Lenes, J.C. Hummelen*, et al.*, Polymer Reviews, 48 (2008) 531-582.